UNIVERSITY OF SOUTHAMPTON

FACULTY OF ENGINEERING, SCIENCE & MATHEMATICS
Optoelectronics Research Centre

Femtosecond Pulsed Laser Deposition

by
Mark Stuart Bennett Darby

Thesis for the degree of Doctor of Philosophy

January 2009

UNIVERSITY OF SOUTHAMPTON

ABSTRACT

FACULTY OF ENGINEERING, SCIENCE & MATHEMATICS
OPTOELECTRONICS RESEARCH CENTRE

Doctor of Philosophy

FEMTOSECOND PULSED LASER DEPOSITION

by Mark Stuart Bennett Darby

This thesis investigates two variations of the conventional pulsed laser deposition (PLD) technique. The first technique is femtosecond PLD, whereby the laser used to ablate the target has a significantly higher peak intensity and shorter pulse duration as compared to conventional nanosecond lasers more commonly used for PLD. Experiments have been conducted on the growth of Nd:$Gd_3Ga_5O_{12}$ (Nd:GGG) films on $Y_3Al_5O_{12}$ (YAG) using a Ti:sapphire laser at a wavelength of 800 nm and pulse length of 130 fs, operating at a repetition rate of 1 kHz. The film properties have been studied systematically as a function of the deposition parameters of laser fluence, spot-size, oxygen pressure, target-substrate distance and temperature. X-ray diffraction analysis shows that highly textured growth has occurred. AFM and SEM analysis reveals that deposits consist of particulates, ranging in diameter from $\sim$0.5 µm to 2 µm.

A comparison between the ion velocities produced by nanosecond and femtosecond laser ablation of the Nd:GGG target material has been investigated using the Langmuir probe technique. The results indicate a large difference in the plasma characteristics between femtosecond and nanosecond generated plumes, with ion velocities up to eight times faster observed in the femtosecond case.

The influence of the deposition parameters on femtosecond and nanosecond pulsed laser deposited gallium lanthanum oxysulphide (GLSO) glass films has been investigated. A comparison between films deposited by femtosecond and nanosecond PLD shows that the compositional range of each ablation regime varies significantly; in particular, femtosecond PLD shows a unique potential for selective fabrication of films with a high lanthanum content well outside the conventional glass-melting region. Experiments have demonstrated how manipulation of the PLD growth parameters can influence the stoichiometric transfer of the PLD process.

The second technique is combinatorial PLD, whereby multiple targets are used to deposit material onto a single substrate. Growth of Nd:GGG by the simultaneous ablation of two separate targets of Nd:GGG and Ga_2O_3 is presented. Experimental results will show the composition and lattice parameter of a film can be controlled by changing the relative laser fluences on the two targets. Films have been grown with enough extra Ga to compensate for the deficiency that commonly occurs when depositing from only one Nd:GGG target.

Contents

List of Figures

List of Tables

Declaration of Authorship

I, Mark Stuart Bennett Darby, declare that this thesis entitled *Femtosecond Pulsed Laser Deposition* and the work presented in the thesis are both my own, and have been generated by me as the result of my own original research. I confirm that:

- this work was done wholly or mainly while in candidature for a research degree at this University;
- where any part of this thesis has previously been submitted for a degree or any other qualification at this University or any other institution, this has been clearly stated;
- where I have consulted the published work of others, this is always clearly attributed;
- where I have quoted from the work of others, the source is always given. With the exception of such quotations, this thesis is entirely my own work;
- I have acknowledged all main sources of help;
- where the thesis is based on work done by myself jointly with others, I have made clear exactly what was done by others and what I have contributed myself;
- parts of this work have been published (see appendix B).

Signed: _____

Date: _____

Contributions of Others

The author acknowledges the following sources of collaboration.

- Chapter 4. The thermal modelling work in this chapter was conducted by A. Muir (ORC).
- Chapter 5. Some of the analysis in this chapter was conducted by others. The rocking curve analysis was conducted by K. D. Rogers (Cranfield University). The ion probe measurements were conducted jointly with T. Donnelly and J. G. Lunney (Trinity College Dublin).
- Chapter 6. The Gallium-lanthanum-sulphide glass samples (bulk) used in this work were made by D. Hewak and co-workers (ORC). The switching device was made jointly with R. E. Simpson (ORC).

All these sources of help are referred to in footnotes in this thesis where appropriate.

Acknowledgements

First, I would like to thank my supervisor Rob Eason for his continuous support during the Ph.D. Rob was always free to listen, give advice and ideas. A special thanks goes to Tim May-Smith for all his help and friendship over these years. Tim has taught me many things and has been an invaluable source of guidance. I also thank others who have been involved in this work, Christos Grivas, Rossana Gazia, Tony Donnelly and James Lunney. In particular, Tony and James for their important contribution and allowing me to visit their facility in Dublin. Thanks must go the Ed Wetherby and Mark Lessey for making various chamber components. I would also like to express my appreciation to John Mills for his help in the FAST lab. A final thanks goes to Angela for all her support during the writing of this thesis.

I would like to thank Peter Wright from QinetiQ for sponsoring this work under a CASE studentship. This work has been funded by the EPSRC under grant number EP/C515668.

Chapter 1

Introduction

Pulsed laser deposition (PLD) is a thin film deposition technique whereby a high-energy pulsed laser is focused onto a target in a vacuum chamber. The target material is vaporised by the high laser intensities and forms a plasma plume that travels towards the substrate, which then condenses on the substrate to form a thin film of the target material. The technique was first demonstrated several years after the invention of the ruby laser, but it was not until 22 years later when Dijkamp et al. (1987) demonstrated deposition of a high-temperature superconducting material, $YBa_2Cu_3O_7$, that PLD became an attractive thin film deposition technique. PLD has come along way since then, and today it has become wide-spread among industry and research, with well-over 10,000 academic papers published on the subject, and is being applied to a wide-range of applications for device-quality functional materials.

To date, however, film production by PLD has been primarily based on the use of nanosecond laser pulses in the UV regime, and typical wavelengths are obtained from excimer lasers at 248 and 193 nm, by frequency-quadrupled (266 nm) or frequency-tripled (355 nm) Nd:YAG lasers. The conventional experimental set-up involves the use of one target and one substrate in a vacuum chamber. This thesis will investigate two different alternatives to this conventional set-up. The aim of this thesis is to improve current PLD technologies by exploring alternative approaches. The first part of this thesis will explore femtosecond PLD, where the laser used to ablate the target material has a significantly higher intensity ($\sim 10^{14}\,\mathrm{W/cm^2}$) and shorter pulse duration (130 fs), as compared to conventional nanosecond lasers used for PLD today. The aim of this work was to investigate the possible advantages this laser regime may have for PLD. The second technique studied in this thesis is combinatorial PLD, which utilises multiple targets

for deposition onto a single substrate. The novel aspect of this research is that it allows thin film growth from targets of different compositions, where the individual plumes can be mixed or temporally delayed to produce unique film properties or structures. These two approaches will be introduced in more detail in the following sections.

1.1 Femtosecond pulsed laser deposition

Ultra-short or femtosecond PLD is an emerging technique offering a new set of opportunities for material deposition. One of the most important advantages of femtosecond lasers is that the energy deposited by the laser pulse does not have enough time to move into the bulk, and therefore, thermal energy remaining in the target can be negligible and the ablation is 'cleaner' than from longer nanosecond ablation (Chichkov et al. 1996). This advantage has motivated the use of femtosecond lasers for a wide range of applications in high-precision materials micro-machining (Rizvi 2002). For PLD, these unexplored high intensity laser regimes can be a promising alternative to the more conventional and well-established nanosecond regime, since the reduced thermal conduction to the bulk may lead to a reduction in the production of molten droplets as is commonly observed with nanosecond-laser deposited films. At these laser intensities, multiphoton ionisation and avalanche ionisation become the dominant absorption mechanism, which means that laser energy can be absorbed at wavelengths that would otherwise be transmitted at a lower intensity. Figure 1.1 shows the number of published articles on the subject of ultra-short PLD each year since 1996. The exploration of this technique is still relatively unfulfilled. However, with the reduction in cost of 'user-friendly' Ti:sapphire laser systems, the prospect for industrial use becomes increasing viable. It is important therefore, that research is undertaken to establish the potential advantages or otherwise this laser regime holds for thin film deposition.

1.2 Combinatorial pulsed laser deposition

The second area of study in this thesis is combinatorial PLD. This multiple laser plume geometry introduces a large degree of flexibility on the composition, properties and device architectures possible for thin films. For example, this technique can be used to (a) create new materials by synchronous deposition from multiple targets, (b) create layered structures by sequentially depositing material from different targets, (c) create

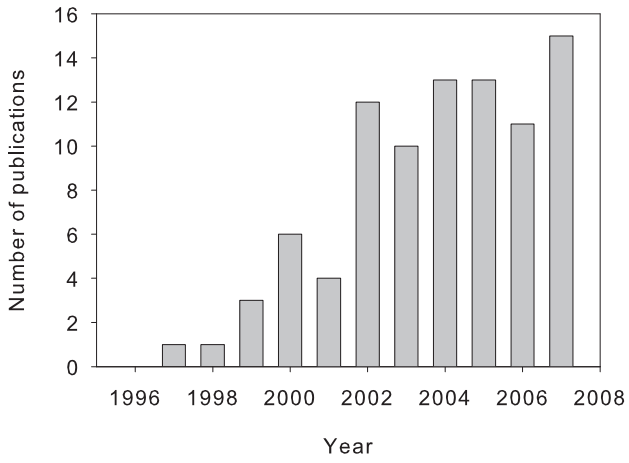

FIGURE 1.1: Number of articles per year on the subject of short-pulse ($< 50\,ps$) duration PLD. (Source: *Web of Science*).

graded structures by gradually changing the mixing ratio (i.e. varying the laser fluence, repetition rate or duty cycle of the different targets), and (d) control film stoichiometry for applications in combinatorial chemistry.

Historically, the combinatorial PLD growth technique can be viewed in the context of the cross-beam PLD approach, first proposed by Gaponov et al. in 1982 to overcome the problem of particulate contamination. In this technique, two laser-generated plumes originating from two separate targets are made to overlap and are directed so that they just miss the substrate. While the comparatively much more massive micron-sized particulates, which have a considerably higher momentum, remain undeviated from their original trajectories, the two plasma plumes combine and expand until they reach the substrate, resulting in a significant reduction in the amount of particulates incorporated in the film. This technique was also applied slightly differently ten years later, and a reduction in the density of particulates was reported using a diaphragm that shadowed the substrate from the direct line-of-sight of the ablation spot (Pechen et al. 1992).

It is not until recently, however, that this multiple-target approach has been used to control the exact film stoichiometry (Gorbunov et al. 1999, Irissou et al. 2006, Levin et al. 2001). To date, reports have focused mainly on the deposition of inter-metallic compounds by cross-beam PLD using two dissimilar targets. It is clear that the potential of the combinatorial PLD approach for thin film deposition of a range of materials has not been fully realised.

1.3 Outline of thesis

This thesis is organised into the following chapters:

- *Chapter 2* explains the theoretical background of ultra-short laser ablation with high intensity, ultra-short duration pulses. It will discuss the mechanisms of ultrashort-pulse laser ablation of materials, and the differences to that of longer nanosecond laser pulses.
- *Chapter 3* will describe the analytical methods used in this thesis.
- *Chapter 4* will describe the design and performance of a novel CO_2 laser heating method using a pyramid-shaped ZnSe prism. Experimental results will be presented on the heating characteristics of the device and thermal modelling will be used to compare the temperature profile produced on the substrate to other known CO_2 laser-heating methods.
- *Chapter 5* will present experimental results on the deposition of Nd:GGG on YAG substrates using a Ti:sapphire femtosecond laser. The effects of various growth conditions, including fluence, spot-size, target-substrate distance and substrate temperature, on the crystallinity will be discussed. A comparison between the ion velocities produced by nanosecond and femtosecond laser ablation of a Nd:GGG target will also be presented.
- *Chapter 6* will present experimental results on the deposition of gallium-lanthanum-oxysulphide glass (GLSO) using femtosecond and nanosecond regime lasers. The effect of the deposition conditions on the film properties will be discussed.
- *Chapter 7* will present an experimental study into combinatorial PLD using two lasers to simultaneously deposit material from two dissimilar targets of Nd:GGG and Ga_2O_3. It will show how the stoichiometry and resultant lattice parameter of a film can be controlled by changing the relative deposition rates from the two targets.
- *Chapter 8* will present experimental results on the deposition of lithium niobate onto silicon using a conventional nanosecond excimer laser.
- *Chapter 9* will summarise achievements of the thesis and discuss the future directions of femtoseond and combinatorial PLD.

Chapter 2

Femtosecond Pulsed Laser Deposition: Theoretical Considerations

This chapter will explore some of the fundamental mechanisms involved in PLD using high intensity ($> 10^{13}\,\mathrm{W/cm^2}$) lasers with ultra-short pulse durations.

One of the drawbacks of using nanosecond lasers for PLD is that there is a comparatively larger heat-affected zone, which can give rise to the generation of molten particulates from the surface of the target (Chen 1994). Ultra-short laser pulses can significantly reduce the extent of heat diffusion into the target, potentially leading to a reduction in the emission of these molten droplets. There have been a few reports into short-pulse duration laser deposition that have shown a reduction in particulates is possible (Dominguez et al. 2002, Rode et al. 1999). Although, many theoretical and experimental studies suggest that in some conditions ultra-short pulse laser ablation can lead to mechanical fragmentation (Perez & Lewis 2002) or cluster emission (Zhigilei 2003) and the generation of sub-micron size particulates (Amoruso et al. 2004b). The extreme conditions of temperature and pressure in the areas irradiated by ultra-short pulses can lead to different properties for the ablated species, with consequences for the deposited films.

Due to the vast number of physical mechanisms involved at these high laser intensities and the complicated nature of the ablation process, involving a number of overlapping stages (laser-solid interactions, laser-plasma interactions and plasma-plume expansion), a generally accepted model for the femtosecond ablation process has not been fully developed. This chapter will present a review of some of the important mechanisms of laser ablation in the high intensity, ultra-short pulse regime, and discuss the consequences of these for material deposition.

2.1 The laser ablation process

The ablation of target material from a laser pulse occurs when the energy delivered to the atoms exceeds their binding energy. The incident laser light is absorbed by electronic transitions in the solid and the absorption and the ablation rate is influenced by the properties of the laser beam (pulse energy, pulse duration and wavelength) and the properties of the target material (metal, semi-conductor or insulator). The wavelength of the laser light plays an important role in the ablation processes. The reflectivity of the targets surface is highly dependent on the laser wavelength, and since UV light has a low reflectivity for many materials in comparison to infra-red light, UV lasers have been predominantly used for laser processes and PLD.

The ablation process can be viewed as being divided into three separate stages, as depicted in figure 2.1. In *stage one* the laser light strikes the target and interacts with the atoms and electrons in the solid, ionising the atoms and transferring energy to the electrons through inverse Bremsstrahlung (IB). The laser energy may be absorbed either by exciting free electrons or by exciting electronic or vibrational transitions in atoms, molecules or impurities. In metals, the absorption occurs due to free electron absorption via IB, that is, electrons in the conduction band absorb a photon and gain a higher energy. In semiconductors, electrons are excited from the valence bands to empty conduction bands, provided that the photon energy exceeds the band gap of the material. In dielectrics, where the band gap is larger than the photon energy,

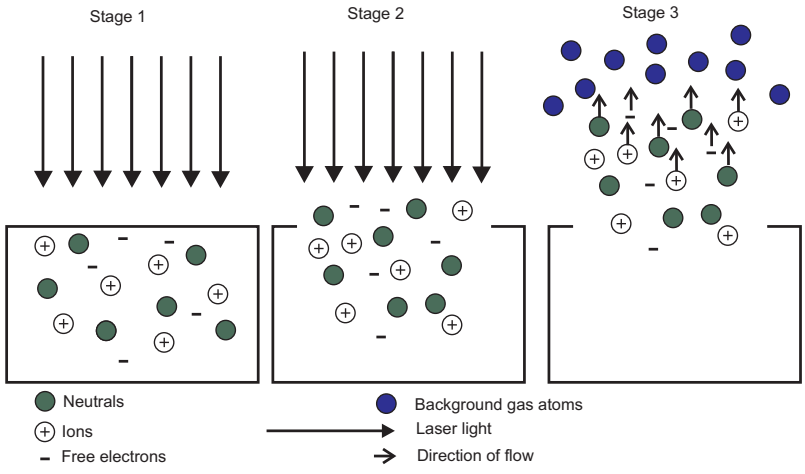

FIGURE 2.1: Schematic of the ablation process. Stage one: absorption of light in the solid; stage two: ejection of ablated material and interaction of light with the pre-formed plasma; stage three: expansion of plasma plume in background gas (or in a vacuum).

multi-photon transitions are required to excite electrons from the valence band to the conduction band.

If the laser is incident normal to the target (z-direction), the radiation intensity decreases below the surface according to Beer's law,

$$I(z) = I_0 e^{-\alpha z} \tag{2.1}$$

where I_0 is the laser intensity at the surface ($z = 0$) and the absorption coefficient α is given by,

$$\alpha = \frac{4\pi\kappa}{\lambda} \tag{2.2}$$

where λ is the wavelength of the laser and κ is the extinction coefficient of the target material. A characteristic length for this process is the skin depth, which is given by, $l_s = 2/\alpha$. This is the depth over which the intensity of the incoming laser light is reduced by a factor of $1/e^2$ of its original intensity.

After a delay of a few ps the electrons and atoms in the solid equilibrate and heating of the irradiated volume occurs. The energy deposited in the skin depth will eventually flow away from the irradiated surface through thermal conduction. Temperatures of up to several thousands kelvin can be achieved with typical nanosecond, UV wavelength pulses used for PLD.

In *stage two* the material from the heated volume is ejected from the target and continues to absorb energy from the laser. The ejection of particles from the surface leads to the formation of a plume of ablated material, which travels away from the target's surface. The plume consists of ions, neutrals, free electrons and fragments.

Stage three is the adiabatic expansion of the plasma plume after the termination of the laser pulse, where it will eventually flow away from the target with a constant velocity (if in a vacuum) or interact with the background gas. After of few µs the plasma plume will arrive at the substrate. The physical parameters of the plume, such as the angular distribution, ion and atom velocity distributions and spatial variations in the composition of the plume can play a very important role for the production of thin films by PLD.

An important point to consider for femtosecond laser ablation is that the duration of the pulse is so brief that any significant movement of the atoms and resultant equilibrium of the irradiated volume will only occur after the pulse has terminated. That is to say

that *stage two* is dramatically different to the nanosecond case: the irradiated volume does not have time to relax into thermal equilibrium during laser exposure.

A characteristic length is the heat-diffusion length during the laser pulse, which gives the heat penetration depth due to thermal conduction. This is given by,

$$l_d = \sqrt{D\tau_L} \tag{2.3}$$

where D is the heat diffusion coefficient and τ_L is the duration of the laser pulse. For femtosecond duration pulses, the value of l_d is such that $l_d = \sqrt{D\tau_L} < l_s$, and heat conducted into the target is significantly reduced, and during the laser pulse almost all the energy is confined within the skin depth of the target.

2.1.1 Two-temperature model

Following the absorption of the laser light the energy is transfered from the energetic electrons to the atoms through electron-phonon collisions. In metals, the transfer of electron energy to the lattice can be described by a two-temperature model (Anisimov et al. 1974). The temperature of the electrons (T_e) and lattice (T_i) can be described by:

$$C_e \frac{\partial T_e}{\partial t} = -\frac{\partial Q(z)}{\partial z} - \gamma(T_e - T_i) + S \tag{2.4}$$

$$C_i \frac{\partial T_i}{\partial t} = \gamma(T_e - T_i) \tag{2.5}$$

$$Q(z) = -k_e \frac{\partial T_e}{\partial z} \tag{2.6}$$

$$S = I(t) A \alpha \exp(-\alpha z) \tag{2.7}$$

where z is the direction perpendicular to the target surface, $Q(z)$ is the heat flux, S is the laser heating source term, $I(t)$ is the laser intensity, A and α are the surface transmissivity and the material absorption coefficient, C_e and C_i are the heat capacities per unit volume of the electrons and lattice, γ is the parameter characterising the electron-lattice coupling and k_e is the electron thermal conductivity. These equations describe the heating of the electrons and lattice, and have two characteristic time scales: the electron cooling time (τ_e) and the lattice heating time (τ_i). The regime of laser heating can be defined using these characteristic times when compared to the duration of the laser pulse (τ_L). For femtosecond pulses ($\tau_L \sim 100\,\text{fs}$), the laser pulse duration is shorter

than the lattice heating time ($\tau_i \gg \tau_L$). This means that during the laser pulse, the electrons and lattice are not in thermal equilibrium and the heated material is inertially confined and does not have time to expand before the end of the pulse. For nanosecond pulses, however, the electrons and the lattice can be considered in equilibrium for most of the pulse duration since the lattice heating time is very much less than the duration of the laser pulse ($\tau_i \ll \tau_L$).

The time required for the electrons to heat the lattice depends on the particular material but lies typically in the range of 2-3 ps picoseconds for metals (Schoenlein et al. 1987). The electron-lattice thermal relaxation time was measured for tungsten films (Fujimoto et al. 1984), niobium films (Yoo et al. 1990), gold films (Brorson et al. 1987) and polycrystalline copper (Hohlfeld et al. 1995). In all these examples, the lattice heating time was measured to be less than a few picoseconds.

2.1.2 Multiphoton ionisation

When the laser intensity is very high ($> 10^{13}\,\mathrm{W/cm^2}$), the atoms can be directly ionised through multiphoton ionisation. This process is schematically shown in figure 2.2. An electron can be removed from its bound energy level or valence band to the free energy level by simultaneously absorbing n photons. The n-photon ionisation rate of an atom varies as $\sigma_n I^n$ where σ_n is the n-photon ionisation cross section and I is the laser intensity. The cross-section σ_n decreases for higher values of n, but I^n dependence ensures that an nth order absorption process will occur if the intensities are high enough. The consequence of this process for femtosecond PLD, is that ablation of material can occur in wavelength regimes that does not permit single-photon ionisation.

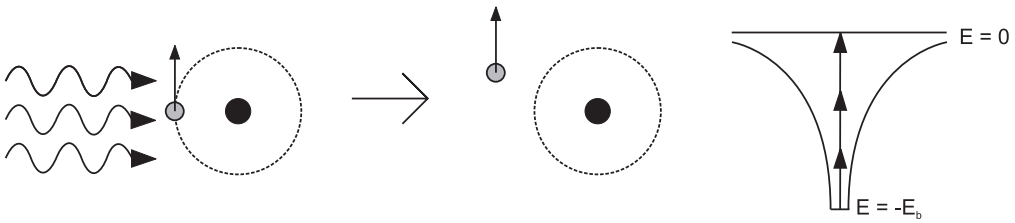

FIGURE 2.2: The multiphoton absorption process. The bound electron is ionised by simultaneously absorbing a number of photons.

2.1.3 Avalanche ionisation

In transparent dielectric materials, the bound valence electrons have an ionisation potential greater than the photon energy. The bound electrons do not absorb the laser light at low intensities. A free electron, however, created through the process of multi-photon ionisation, can gain energy when it collides with a bound electron. The electron can be accelerated enough so that its kinetic energy exceeds the ionisation potential of a bound electron. The next collision with a bound electron will result in an ionisation event if the electron transfers enough energy to the bound electron, resulting in two free electrons with lower kinetic energies. This process will continue, leading to an exponential increase in the free electron density and is known as avalanche ionisation.

The dominant channel for free electron generation from femtosecond pulses has been found to be either avalanche or multiphoton ionisation depending on the size of the band gap. Measurements on the fluence threshold breakdown of fused silica from high intensity femtosecond pulses show that the dominant mechanism is likely to be avalanche ionisation, which is seeded by multiphoton ionisation. (Du et al. 1994, Pronko et al. 1998).

2.1.4 Normal skin effect

An important point to consider for femtosecond laser ablation is that there is not enough time for the plasma to form in front of the target during the laser interaction. This results in the laser light interacting with a near-solid-density plasma. Due to multiphoton and avalanche ionisation this plasma can be above the critical density, n_c, which is the density above which the plasma becomes opaque for electromagnetic radiation with an angular frequency of ω:

$$n_c = \frac{m_e \omega^2}{4\pi e^2} \tag{2.8}$$

where e and m_e are the electron charge and mass respectively. Plasmas that are above the critical density are highly reflective, and in the absence of absorption the electromagnetic field, $E(z)$, will form a standing wave in front of the target in the form of an evanescent wave penetrating into the overdense plasma, given by the equation,

$$E(z) = E_0 \exp\left(\frac{-z}{l_s}\right) \tag{2.9}$$

where z and E_0 is electric field at the plasma-vacuum boundary. This is known as the normal skin effect.

2.2 Ablation mechanisms

2.2.1 Coulomb explosion

It has been shown that ion Coulomb explosion can occur from the surface region of dielectrics due to irradiation with ultra-short pulses (Stoian et al. 2002). Under intense laser irradiation from femtosecond or picosecond pulses, it is possible that electron emission from the surface can occur early in the laser pulse, leading to a high level of charging of the surface region. If this surface region is not neutralised faster than the time for the ions to react to the electrostatic repulsion of their neighbours ions, this charge build-up can result in ion emission by Coulomb explosion. This process is illustrated in figure 2.3. Stoian et al. (2002) used ion time-of-fight mass spectrometry to detect emission of ions from the highly charged surface of Al_2O_3 exposed to 100 fs pulses. Two ablation phases have been identified in the specific case of Al_2O_3 (Tam et al. 1989): the 'gentle' phase and the 'strong' phase. The 'gentle' phase is found for low laser fuences (and low numbers of laser shots) and only a small amount of material is removed ($\sim$10 nm per pulse) leaving behind a smooth surface (Ashkenasi et al. 1999). The observation of a fast ion emission from the ablation of sapphire (Stoian et al. 2000) was interpreted as originating from the Coulomb explosion mechanism. Prior to this work, Daguzan et al. (1994) reported the emission of fast electrons from ablation of quartz using 100 fs pulses.

2.2.2 Phase explosion

Phase explosion (or explosive boiling) has been proposed as one of the primary mechanisms involved in ultrashort laser ablation (Zhigilei 2003). The irradiation from ultrashort laser pulses can result in the material becoming rapidly overheated to a temperature much higher than the boiling point. At temperatures close to the critical temperature, homogeneous nucleation of the material can occur at an extremely high rate, which leads to the explosive expansion of the material into a mixture of vapour and liquid droplets.

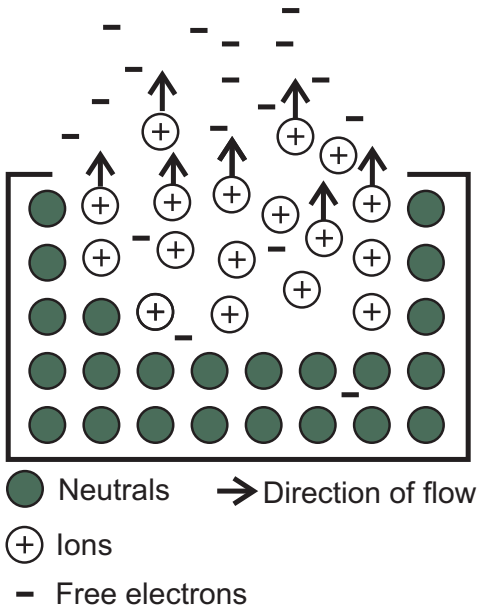

FIGURE 2.3: Schematic view of a planar Coulomb explosion mechanism for dielectric materials irradiated with ultrashort laser pulses.

Zhigilei (2003) has performed molecular dynamics simulations on laser ablation with 15 ps to 150 ps duration pulses. They have found that at sufficiently high laser fluences, the material forms into a 'foamy' transient structure of interconnected liquid regions that decomposes into a mixture of liquid droplets, gas phase molecules, and small clusters of up to $\approx 10^4$ atoms.

2.2.3 Photomechanical fragmentation

Photomechanical fragmentation has been proposed as a mechanism for the formation of nanoparticles from ultra-short laser ablation (Perez & Lewis 2002). In this process, the target disintegrates into clusters as a result of the mechanical stress imposed by rapid thermal expansion of the surface and ablation occurs without any change into the vapour phase. Perez & Lewis (2002) have developed a molecular dynamics simulation to describe the relaxation of a two-dimensional Lennard-Jones fluid, after the irradiation by a femtosecond (100 fs) laser pulse. They found that laser ablation in the short-pulse regime involved mechanical processes, which resulted in the emission of nanoparticles.

2.3 Summary

This chapter has presented a brief review of some of the important mechanisms involved in femtosecond laser ablation. To summarise, femtosecond laser ablation results in the material becoming rapidly heated through a combination of multiphoton absorption and avalanche ionisation. The pulse duration is shorter than the thermal relaxation time of the material, which can lead to non-thermal ablation mechanisms. The short pulse duration also means that the laser light interacts with a near-solid density plasma. Rapid heating of the irradiated volume can lead to a number a mechanisms that do not occur under conventional nanosecond PLD conditions, such as Coulomb explosion, phase explosion and photomechanical fragmentation. In the context of PLD, the fact that the target material undergoes rapid heating without any significant collateral damage to the bulk could potentially lead to a reduction in emission of molten droplets. However, mechanisms such as phase explosion and photomechanical fragmentation can lead to the formation of nanoparticles from the ablated target, which would be detrimental to the quality of films intended for laser waveguide applications.

Chapter 3

Analytical Methods

This chapter will briefly describe the analytical methods used in this thesis.

3.1 Scanning electron microscopy

Scanning electron microscopy (SEM) was used to analyse the surfaces of the thin films. It can be used to measure the size and distribution of particulates on the surface of films, and is a good indicator of the surface quality.

The technique works by generating an electron beam by heating a tungsten filament and accelerating the electrons through condensing lenses in a vacuum (10^{-6} mbar) where they are focused to a spot of a few nanometers in diameter. The beam then passes through pairs of scanning coils, which deflect the beam across the surface of the sample. When the electron beam interacts with the sample, the electrons are scattered from the surface of the film. The sample is coated with conducting film ($\sim$ nm thick), usually carbon or gold that is grounded to prevent charge build-up on the surface. The images are obtained by detecting the secondary electrons emitted from the surface of the sample. SEM is capable of producing images with resolutions of roughly 10 nm (depending on the focused spot-size and the energy of the electron beam). The equipment used in this thesis was a *LEO 1455VP SEM* or a *JSM-5910*.

3.2 Energy dispersive X-ray analysis

Energy dispersive X-ray analysis (EDX) was used to identify the chemical composition of the deposited films and is an integrated feature of SEM equipment. The process works by bombarding the film with electrons, which collide with the atom's inner shell

electrons in the sample, knocking them out of their bound state. The vacancy in the inner shell is then filled with an electron from the outer shell and X-rays are emitted from the interaction volume, which extends from roughly 100 nm to 5 µm from the surface of the sample (depending on the energy of the electron beam and the sample material). These X-rays have an energy spectrum unique to each element. An X-ray detector (SiLi detector) is used to measure the energy of the X-rays and the spectrum is used to quantitively measure the composition of the volume analysed. The energy of the X-rays was calibrated by analysing the X-ray spectrum produced from a known material (typically silicon or cobalt). The equipment used in this thesis for compositional analysis was an *Oxford Inca 300* model.

3.3 Atomic force microscopy

Atomic force microscopy (AFM) was used to analyse the topography of the deposited films. Unlike SEM, AFM provides a three-dimensional surface profile. AFM works by detecting the van der Waals forces exerted between the surface of the film and a small atomically sharp tip attached to the end of a cantilever. As the the tip is brought closer to the surface, these forces lead to a deflection of the cantilever. The deflection of the cantilever is measured by detecting the change in position of a reflected diode laser beam from the end of the cantilever using an array of photodiodes (for contact mode). AFM is advantageous since it can reveal information about the height and shape of the topographic features with a very high resolution ($\sim$0.1 Å). The disadvantage of AFM compared to SEM is the area that can be analysed, which is limited to roughly 100 µm by 100 µm, compared to the millimeter scale possible with SEM. For the analysis of films in this thesis, the AFM apparatus was primarily used in non-contact mode, which means that the cantilever was given a small oscillation and the forces between the tip and the film were measured by detecting the change in oscillation amplitude, phase and resonance frequency of the cantilever in response to electrostatic forces from the atoms on the surface of the film. A feedback mechanism enables the piezoelectric scanners to maintain the tip at a distance from the film as it scans across the surface. The conventional contact mode operation often produced poor quality micrographs, possibly due to small fragments becoming attached to the end of the probe.

3.4 Surface profilometry

The thickness of the films was measured using a profilometer (*Tencor P-16*). The profilometer works by moving a stylus across the surface of the film while keeping a specified contact force constant. The profilometer can measure height variations of a few angstroms, and is capable of analysing areas of several centimetres squared. The film thickness was determined by scanning the stylus over areas of the substrate where the film did not grow (due to the presence of the substrate holder during deposition).

3.5 X-ray diffraction analysis

X-ray diffraction (XRD) analysis was used to investigate the phase, crystallographic orientation, texture and lattice parameter of the films. The technique works by detecting diffracted X-rays from the crystal planes in the sample. The scattered X-rays will interfere constructively at a given scattering angle due to their long range order. The condition for constructive inference is defined by Bragg's law:

$$2d \sin\theta = n\lambda \tag{3.1}$$

where θ is the angle of incidence of the X-rays, d is the spacing of the atoms for given a crystal plane, λ is the wavelength of the X-rays (for CuKα radiation $\lambda = 1.54\,\text{Å}$) and n is an integer, representing the order of the diffraction peak.

XRD analysis was operated in two modes: the $\theta - 2\theta$ mode and the $\omega - 2\theta$ mode, which are schematically shown in figure 3.1. In $\theta - 2\theta$ mode (figure 3.1(a)), the intensity of the scattered X-rays is measured as a function of 2θ. Peaks in the spectrum can be identified to specific crystalline phases by comparing the spectrum to XRD data of known materials[1]. Since the substrate is of known crystalline orientation and phase, the spectrum can also be normalised using the 2θ position of the substrate. This can remove any small shifts in peak locations due to minor differences in sample alignment. For GGG films, the spectrum was normalised to the YAG (400) 2θ peak position. Alternately, the YAG peak position may also be determined from *ab initio* calculations on the structure of YAG (Xu & Ching 1999).

Once the phase and orientation of a film are assigned and the spectrum has been normalised, it is possible to determine the lattice parameter of a crystalline film. For a

[1] In this thesis, this data has been obtained from the *Inorganic Crystal Structure Database*

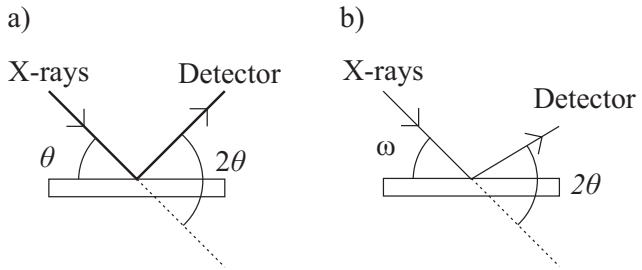

FIGURE 3.1: Configuration of X-ray diffraction measurements in the (a) $\theta - 2\theta$ mode and b) $\omega - 2\theta$ mode (rocking curve).

peak position θ_{hkl} corresponding to a lattice plane with miller indices (hkl), the lattice parameter for a cubic crystal is given by,

$$a = \frac{\lambda\sqrt{h^2 + k^2 + l^2}}{2\sin\theta_{hkl}}. \tag{3.2}$$

In $\omega - 2\theta$ mode, XRD can be used to investigate the texture of the films. The practice is based on conventional X-ray diffraction, accept the angles of X-ray incidence and detection are not coupled. The configuration is illustrated in figure 3.1(b). In this mode, the intensity is measured as a function of ω, and θ is kept at a specified angle (the position of the peak under analysis). A 2D spectrum is obtained by systematically increasing θ around the peak position and measuring intensity against ω. The FWHM of this peak is an indication of the texture or quality of the film.

3.6 Ion probe analysis

An ion probe was used to characterise the laser-produced plasmas from both femtosecond and nanosecond lasers. The device is conceptually very simple, consisting of a conductive electrode immersed in the plasma, connected to an external electrical circuit. Figure 3.2 shows a typical circuit used for the measurements. The probe can be biased positively or negatively to measure the flow of electrons or ions produced from the target. The voltage drop across the load resistor is measured on an oscilloscope. An image of a typical ion probe used for experiments in this thesis is shown in figure 3.3.

At high enough negative bias voltages, the electrons in the plasma are prevented from reaching the probe, and the ionic probe current saturates.

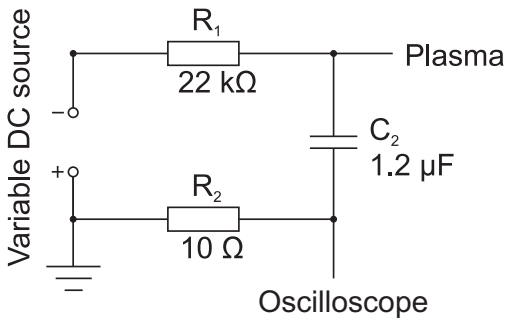

FIGURE 3.2: Probe circuit used for Langmuir probe measurements.

Under this regime, the current is proportional to the ionic density in the plasma and the velocity of the plasma, and is defined as,

$$I_i = An_i e v_i \tag{3.3}$$

where e is the charge on the electron, v_i is the flow velocity of the plasma and A is the probe area (perpendicular to the direction of the plasma flow). From the time-of-flight (TOF) spectrum, a range of physical quantities of the plasma can be determined, such as the velocity of the ions (peak TOF), the velocity distribution, the ion density and ion deposition rate.

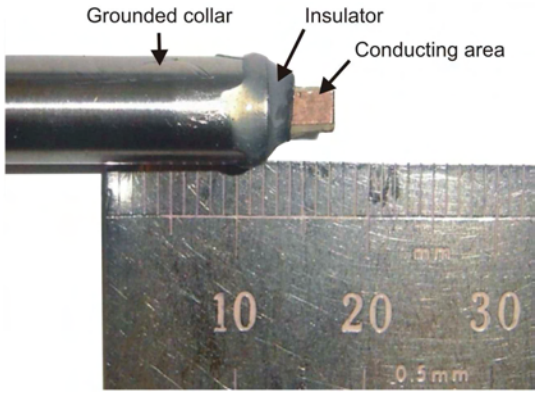

FIGURE 3.3: Photograph of a Langmuir probe (photograph by T. Donnelly).

Chapter 4

Advancements in CO_2 Laser-Heating for PLD

This chapter will report on the design and characteristics of a ZnSe tetra-prism for homogeneous substrate heating using a 25 W CO_2 10.6 µm wavelength laser. Experiments have been conducted to investigate the heating characteristics of the device using temperature sensitive liquid crystal (TSLC) film and the temperature of the deposition face of the substrates has been measured for various heating powers. The temperature profile on the deposition face of a YAG substrate will be compared to other known CO_2 laser-heating methods.

4.1 Introduction

A method of heating substrates that provides a uniform temperature distribution is necessary for the fabrication of high-quality homogeneous films. Conventional methods that are commonly used for PLD, such as resistive heating elements and thermocoax heaters, are highly inefficient and result in heating of the chamber and subsequent out-gassing of the deposit on the chamber walls. This can result in contamination of the growing films. Typically these methods have temperature limits of around 1000℃ due their significant radiative losses. A method of heating that is both efficient and homogeneous would be highly desirable for applications in PLD.

CO_2 laser heating overcomes the drawbacks associated with conventional heating methods, since it is highly efficient and can prevent undesirable heating of the deposition chamber. This high efficiency means that higher temperatures can be attainable with

commercially available lasers. The temperature of the substrate, T, for given heating power, P is described by the Stefan-Boltzmann's law:

$$P = \epsilon\sigma A(T^4 - T_s^4), \tag{4.1}$$

where T_s is the temperature of the surroundings, ϵ is the emissivity of the substrate, σ is Stefan-Boltzmann constant and A is the surface area of the substrate. For example, the power required to reach $\sim$1400 K is less than 22 W (assuming $\epsilon = 0.5$ and A=2 cm^2). Achieving the same temperature using resistive heaters techniques is practically impossible as the surface area of the heated components is significantly larger.

The radiation emitted by the laser-heated substrate will result in heating of the surrounding (namely the chamber walls and the substrate holder), which may in turn affect the temperature of the substrate. It should be noted therefore, that Stefan-Boltzmann's law, as used in this case to estimate the temperature of the substrate for a given laser power, only yields an approximate estimate of the overall substrate temperature. The diameter of the chamber used for laser-heated PLD experiments in this thesis is roughly 40 cm, with a height of 30 cm, and the substrate (size: 1 cm$\times$1 cm$\times$1 mm) is positioned in the centre of the chamber. The geometry of this experimental set-up means that the radiation from the comparatively smaller substrate will not result in the chamber becoming heated to high enough temperature to significantly affect the substrate's temperature[1]. For PLD experiments with more spatially confined geometries and/or larger substrates, the effects of the chamber walls may need to be taken into account when estimating the substrate temperature.

A raster-scanned CO_2 laser heating method has been used in the past (Barrington & Eason 2000), which has some degree of flexibility, in that the temperature profile can be easily adjusted by altering the local dwell time of the laser beam over selected areas of the substrate. A uniform temperature profile is achieved in this case by exposing the outer regions of the substrate for a longer period of time, which counter-balances the effect of radiation losses at the edges. Reflective beam homogenisers (Anderson et al. 1997) have also been used, but the size and position of these devices often means that they are located within the chamber and can, as a result, become coated in the ablated material. Metallic blocks attached to the substrate that diffuse the heat has been reported (Wu

[1]It can be shown that with a laser power of 12 W (typical powers used), the average temperature of a stainless steel chamber will be raised by less than 10°C (assuming the surface area of the chamber is >2000 cm^2).

et al. 1991), however, the large surface area and the high radiation losses of the metal block means that the substrate temperature obtainable will be limited.

There have been several reported attempts to improve the homogeneity of the temperature profile on substrates using a CO_2 laser beam (Hirai et al. 2003, Hopkins et al. 2000). Hirai et al. (2003) have proposed a ZnSe beam homogeniser that transforms the Gaussian profile into a uniform circular profile using two aspheric lenses. However, the circular spatial profile of the irradiating beam onto a square-shaped substrate would result in a significant amount of energy being wasted (roughly 36%).

The novel heating method proposed in this chapter involves transforming a CO_2 Gaussian laser beam into a square profile by passing it through a pyramid-shaped ZnSe prism (tetra-prism). As will be shown, this method can potentially heat substrates with a higher degree of uniformity that is currently unattainable. The laser intensity profile on the back-face of the substrate can also be modified by changing the spot-size of the CO_2 laser beam, and therefore compensate for higher radiative losses at the edges and create a more homogeneous temperature profile.

4.2 Design and modelling

The design of the the ZnSe tetra-prism is shown in figure 4.1 and the experimental set-up for heating substrates is shown in figure 4.2.

The ZnSe tetra-prism consists of a pyramidal shaped ZnSe optic, the function of which is to achieve square heating profile on a 1 cm square substrate by over-lapping four quarters of an incident Gaussian beam. The angle of the facets was determined from the working distance and the size of the substrates. For the tetra-prism to be positioned outside the chamber a working distance of $\gtrsim 30$ cm was required.

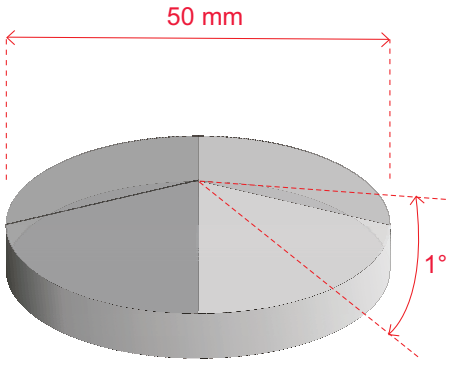

FIGURE 4.1: 3D diagram of the ZnSe tetra-prism.

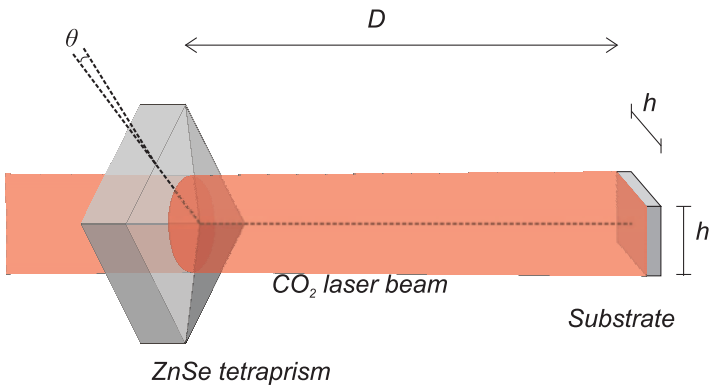

FIGURE 4.2: Experimental set-up for the ZnSe tetra-prism heating method.

Using Snell's law, the angle of the facets, θ, can be calculated according to the following equation,

$$\arcsin\left(n_z \sin\theta\right) - \theta = \arctan\left(\frac{h}{\sqrt{2}D}\right) \tag{4.2}$$

where n_Z is the refractive index of the tetra-prism (=2.4 for ZnSe (Marple 1964)), h is the substrate width and D is the distance between the tetra-prism and the substrate. For simplicity only a non-divergent laser output beam has been considered. Using the small angle approximation ($\sin x = x$), the formula can be written as (θ is in radians),

$$\theta \simeq \frac{h}{\sqrt{2}D\left(n_Z - 1\right)} \tag{4.3}$$

For a working distance of 30 cm and a substrate width of 1 cm the approximate angle of the facets can be calculated to be 1.0°. Two prisms were manufactured[2] from ZnSe chamber port windows of diameter 50 mm. The angle of each facet was subject to a manufacturing tolerance of ±0.1°.

An important feature of the CO_2 laser-heating method is the substrate holder, which enabled heating of the substrate with minimal heat conduction to the holder. For this, alumina ceramic tubing was machined[3] to support the substrate, as shown in figure 4.3. The holder allows a large amount of the substrate surface to be utilised for film growth, with only four small regions (less than 1 mm × 1 mm) on the edges of the substrate where film does not grow.

[2]The prisms were manufactured by *Crystran Ltd (UK)*
[3]The ceramic tubes were machined by T. C. May-Smith (ORC)

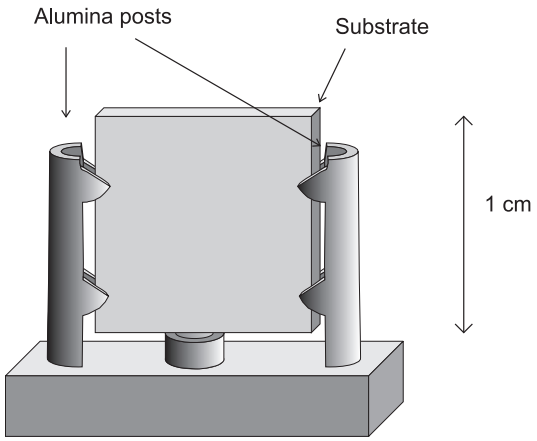

FIGURE 4.3: Substrate holder design.

4.2.1 Effects of the facet edges of the tetra-prism

The edges between each facet of the tetra-prism form a sharp discontinuity that gives rise to Fresnel diffraction. The effect of one polished facet of the tetra-prism is to displace one-quarter of the incident beam in a direction transverse to the direction of propagation of the incident beam. The purpose of the following model is to give an indication of the interference pattern that may occur from the sharp discontinuity at the facet edges of the tetra-prism. This model has been simplified by considering a right-angled obstruction, which roughly simulates edges of a single facet (i.e. one quarter) of the tetra-prism.

The incident waves (plane waves have been assumed) of intensity I_0 upon a right-angled obstruction (see figure 4.4) produce an intensity I_p at a distance of r_0 from the obstruction that is given by (Hecht 2002, p 500),

$$I_p = \frac{I_0}{4} \mid B_{12}(u) \mid^2 \mid B_{12}(v) \mid^2 \tag{4.4}$$

where,

$$B_{12}(u) = [\mathcal{C}(u) + i\mathcal{S}(u)]_{u_2}^{u_1}$$

$$B_{12}(v) = [\mathcal{C}(v) + i\mathcal{S}(v)]_{v_2}^{v_1}$$

and,

$$u_n = y_n \left(\frac{2}{\lambda r_0}\right)^{1/2} \qquad v_n = z_n \left(\frac{2}{\lambda r_0}\right)^{1/2} \qquad n = 1, 2$$

where y_1 and z_1 are the distances of the horizontal and vertical edges (note that $y_2, z_2 = \infty$), λ is the wavelength of the incident light and the Fresnel integrals $\mathcal{C}(w)$ and $\mathcal{S}(w)$

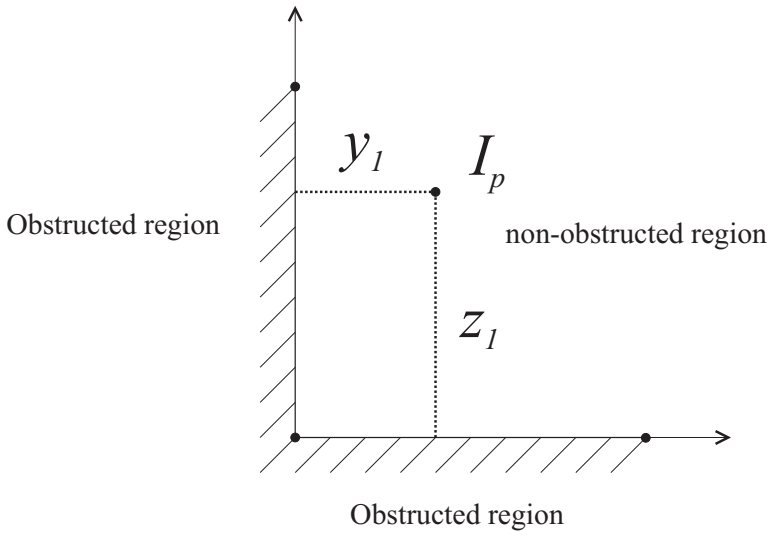

FIGURE 4.4: Diagram to illustrate a right-angled obstruction with the orthogonal edges a distance y_1 and z_1 from I_p. I_p is a distance r_0 from the obstruction.

are defined as,

$$\mathcal{C}(w) = \int_0^w \cos\left(\pi w'^2/2\right) dw' \qquad \mathcal{S}(w) = \int_0^w \sin\left(\pi w'^2/2\right) dw'.$$

By solving equation 4.4 for values of y_n and z_n it is possible to map the irradiance profile caused by the obstruction. The 2-D Fresnel pattern for a right-angled obstruction illuminated with plane waves of wavelength 10.6 µm at a distance 30 cm is shown in figure 4.5.

4.2.2 Interference effects

The beam incident on the prism is spatially coherent and the re-arrangement of the beam quarters by the prism will result in the formation of interference fringes within the overlapping region. This interference pattern will result in a modulation in the intensity profile on the substrate. The modulation will be complicated as it involves the interference of four beam portions. For simplicity, consider the interference due to two plane waves propagating through a ZnSe bi-prism with a facet angle of θ. The periodicity of the interference fringes is described by,

$$\delta = \frac{\lambda}{\sin\left(\arcsin\left(n_z \sin\theta\right) - \theta\right)} \approx \frac{\lambda}{\theta(n_z - 1)}, \tag{4.5}$$

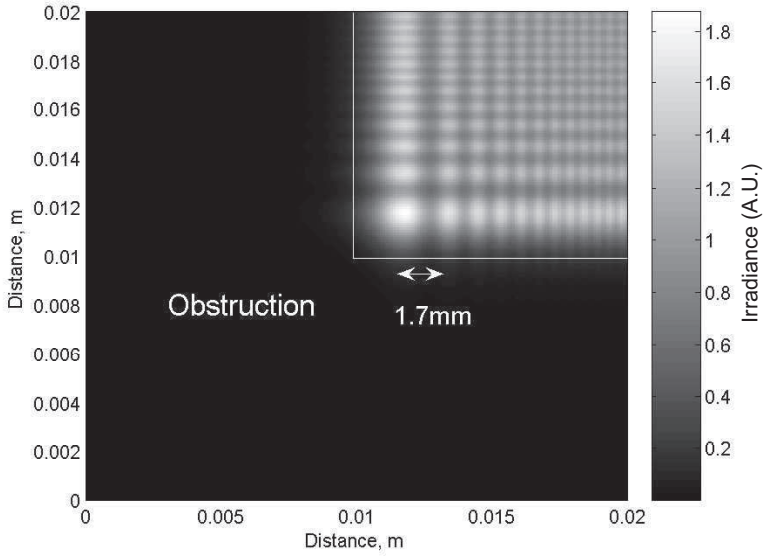

FIGURE 4.5: Modelled irradiance profile produced from a right-angled obstruction that is illuminated with plane waves at a wavelength of 10.6µm at a distance from the obstruction of 30 cm. The irradiance before the obstruction is unitary. This illustrates the interference that may occur from the right-angled edges of the tetra-prism.

where n_z is the refractive index of ZnSe and λ is the wavelength of the laser. For $\theta = 1°$, $n_z = 2.4$ and $\lambda = 10.6$µm, the periodicity, δ is 430µm.

4.2.3 Three-dimensional heat diffusion modelling

Finite element modelling[4] was used to construct a three-dimensional (3D) profile of the temperature on the deposition face of a YAG substrate with dimensions 10 mm × 10 mm × 0.5 mm. A full description of the model and the results can be found in appendix A. Only a review of the important results from this work will be presented here.

A range of different CO_2 laser heating options were considered, these include, heating the substrate with:

- an untransformed Gaussian laser beam;
- a Gaussian beam homogenised using a square-tapered beam-pipe;
- a raster-scanned Gaussian beam in a 6×6 grid (as used by Barrington & Eason (2000));
- a Guassian beam homogenised using the ZnSe tetra-prism.

[4]The thermal modelling results presented in this section were conducted by A. Muir (ORC).

For each of these options, the laser heating parameters (laser beam waist, and spot-size) were varied to result in the most uniform temperature distribution on the deposition face of a YAG substrate at typical deposition temperatures (roughly 1000 K at the centre of the substrate). The results are summarised in table 4.1. This table gives the minimum standard deviation of the temperature profile, the mean temperature and the range of temperature on the deposition face of a YAG substrate. The important result here is that despite the modulation caused by Frensnel diffraction, the ZnSe tetra-prism produces a temperature distribution with standard deviation of only 2.2 K. This is noticeably smaller than the square-tapered beam-pipe case, even though this method is shown to produce the most uniform laser intensity profile (May-Smith et al. 2008). This is because the comparatively higher radiative emission that occurs at the edges of the substrate is compensated for by using the ZnSe tetra-prism to irradiate the edges with higher intensities. This is achieved simply by changing the laser beam spot-size and/or working distance.

		Surface temperature properties (K)		
Homogenisation technique	Power (W)	Standard deviation	Mean	Range
Untransformed Gaussian	5.6	43	978	173
Square-tapered beam-pipe	7.2	7.2	1068	34
Raster-scanned 6 ×6 grid	6.9	14	1052	63
ZnSe Tetraprism	9.5	2.2	1076	14

TABLE 4.1: Summary of modelling results for the different homogenisation techniques (May-Smith et al. 2008).

4.3 Experimental characterisation

4.3.1 Heating profile using a CO_2 laser beam

A temperature sensitive liquid crystal (TSLC) film was used as a viewing screen to obtain a rough indication of the temperature profile from the CO_2 laser beam homogenised using the tetra-prism method. The TSLC exhibits a colour spectrum response with temperature change and therefore can provide a detailed thermal map of the homogenised laser beam.

The laser beam was first collimated to a beam waist of 4 mm and then passed through the tetra-prism onto the TSLC sheet. It was necessary to adhere the TSLC film to a metal plate with conductive silver paste in order to prevent heat spreading along the surface of the film. The output power of the laser remained at 0.5-1 W throughout the

experiment and the camera was positioned roughly 3 cm away from the TSLC film at an angle of roughly 45°. Due to the angle of the camera the images needed to be corrected for perspective distortion[5]. The experimental set-up is shown in figure 4.6.

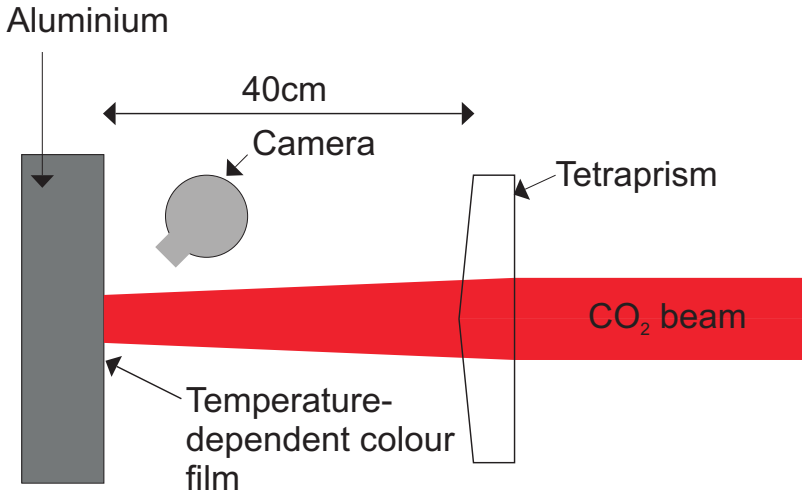

FIGURE 4.6: Experimental set-up used to investigate the CO_2 laser-heating characteristics of the ZnSe tetra-priam.

An image of the TSLC film is shown in figure 4.7 (for $D = 40\,\text{cm}$ and $w = 4\,\text{mm}$). Notice that the heating profile has dimensions 11 cm by 12 cm. This rectangular profile is believed to be due to the asymmetry of the polished facets. The heating profile shows large low intensity bands which are due to Fresnel diffraction from the edges between each adjacent facet of the tetra-prism. Interference fringes with a lower periodicity of roughly 0.5 cm are also visible on the profile and are enveloped by the larger Fresnel diffraction fringes.

4.3.2 Temperature measurements

Measurements of the substrate temperature were made using a thermocouple attached to the deposition face of a YAG substrate (1 cm×1 cm×1 mm) heated with a CO_2 laser homogensied using the ZnSe tetra-prism. An accurate measurement of substrate temperature is technically difficult to achieve because the thermocouple acts as a heat sink and reduces the substrate temperature where the measurement is made. Also, poor thermal contact between the thermocouple and the substrate can result in inaccurate temperature readings. To improve the repeatability of the temperature measurements, a very small amount of thermally conductive gallium-indium paste was used on the tip

[5]Using software: *Hugin - version 0.6.1* (20th August, 2006). Developed by Pablo d'Angelo and co-workers.

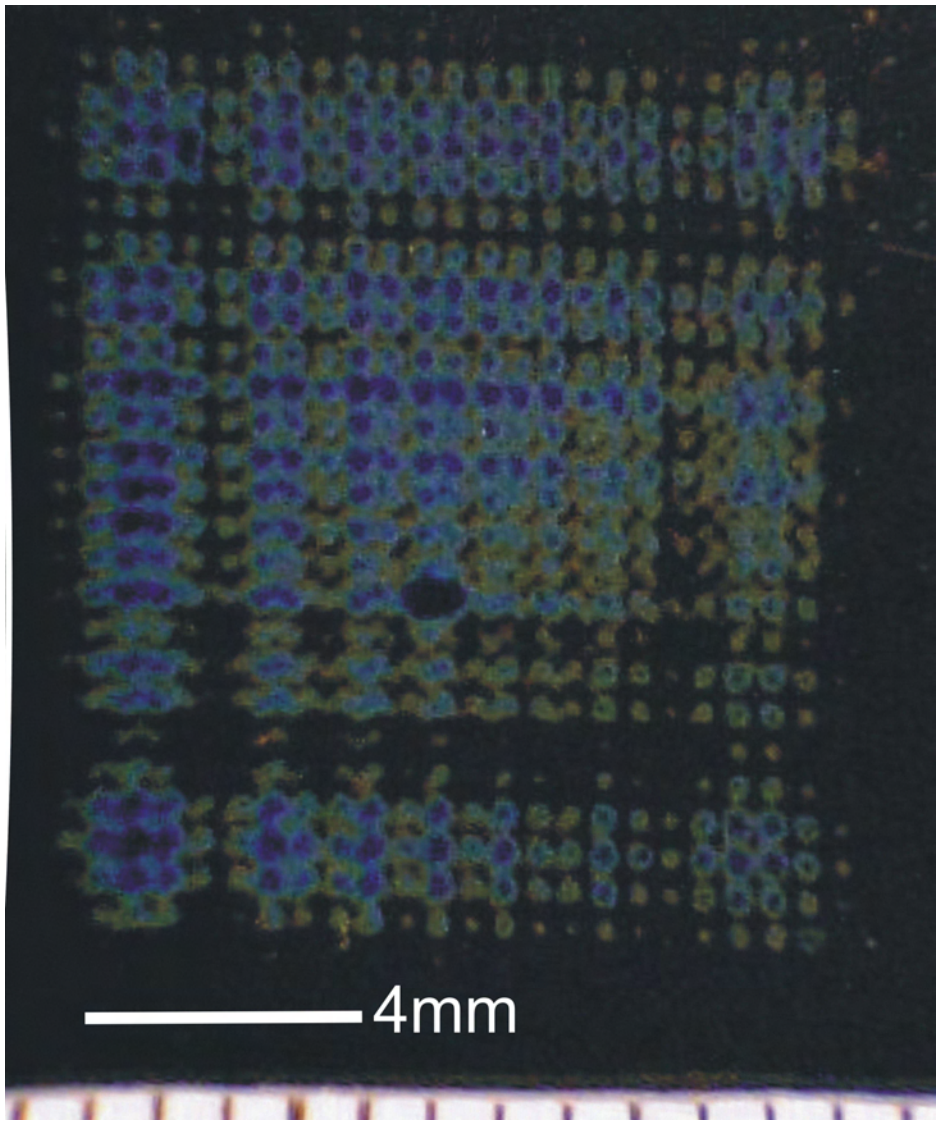

FIGURE 4.7: A photograph of an intensity profile generated by the tetra-prism heating method using TSLC film. The experimental set-up is shown in figure 4.6. The image was taken at an angle of roughly 45° and perspective correction software was used to correct for perspective distortion.

of the thermocouple (0.25 mm diameter type-K). The thermocouple was attached to the centre of the deposition face of the substrate, and the measurements were made for various incident laser powers. The measurements were made under a pressure of 0.1 mbar to accurately predict temperature for typical deposition conditions. The temperature of the substrate was allowed to stabilise for a period of ∼3 minutes between each measurement. To simulate typical deposition conditions, the substrate was located in a vacuum chamber under a pressure of 0.1 mbar.

Figure 4.8 shows a graph of the incident CO_2 laser power on the substrate plotted against the measured substrate temperature. The data obtained from attempts 2-4 was

fitted to Stefan-Boltzmann's law (equation 4.1). The fit yielded a value of emissivity of roughly 0.77. The measurements are in good agreement with the predicted model at the typical temperatures. The heat diffusion model predicted that the substrate surface temperature would be 1073 K for an absorbed power of 9.5 W (May-Smith et al. 2008).

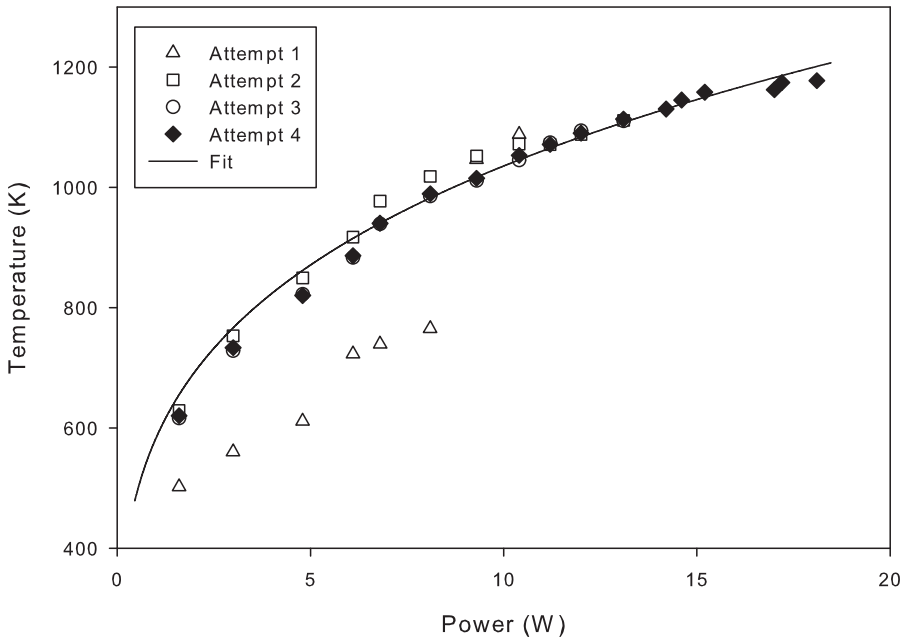

FIGURE 4.8: Temperature calibration curve for the tetra-prism heating method (conducted inside a vacuum chamber at a pressure of 0.1 mbar).

4.3.3 Intensity profile using a HeNe laser

A beam profiler was used to obtain an intensity profile from a HeNe laser beam homogenised using the tetra-prism method. The set-up is shown in figure 4.9. It is important to note that these measurements were conducted with a second ZnSe tetra-prism (made with the same design specifications as presented in section 4.2). Profiles were taken for beam waists of 2 mm, 3 mm and 4 mm, and are shown in figure 4.10. These profiles demonstrate how the intensity distribution can be modified by changing the beam waist of the incident laser and also reveal the accuracy of the facet angles. As can be seen from figure 4.10(a), the top-right corner of intensity profile is not aligned with the other three corners. This is because the angle of the corresponding facet is slightly smaller, leading to a smaller angle for the refracted light. This indicates the need for the device to be manufactured to higher tolerances in the future. The manufacturing tolerance of the current device is $\pm 0.1°$, which leads to a positional accuracy in the CO_2 laser heating profile of ~ 0.1 cm (in the x and y directions on a substrate located 30 cm from the tetra-prism). For the tetra-prism to provide a heating profile to an accuracy of 0.01 cm, the manufacturing tolerance of the facet angle would need to be improved to $< 0.02°$.

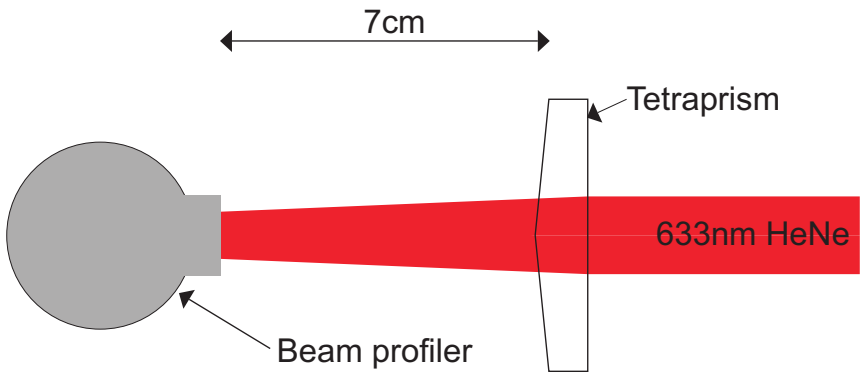

FIGURE 4.9: Experimental set-up used to investigate the intensity profile produced from passing a HeNe laser through the ZnSe tetra-prism.

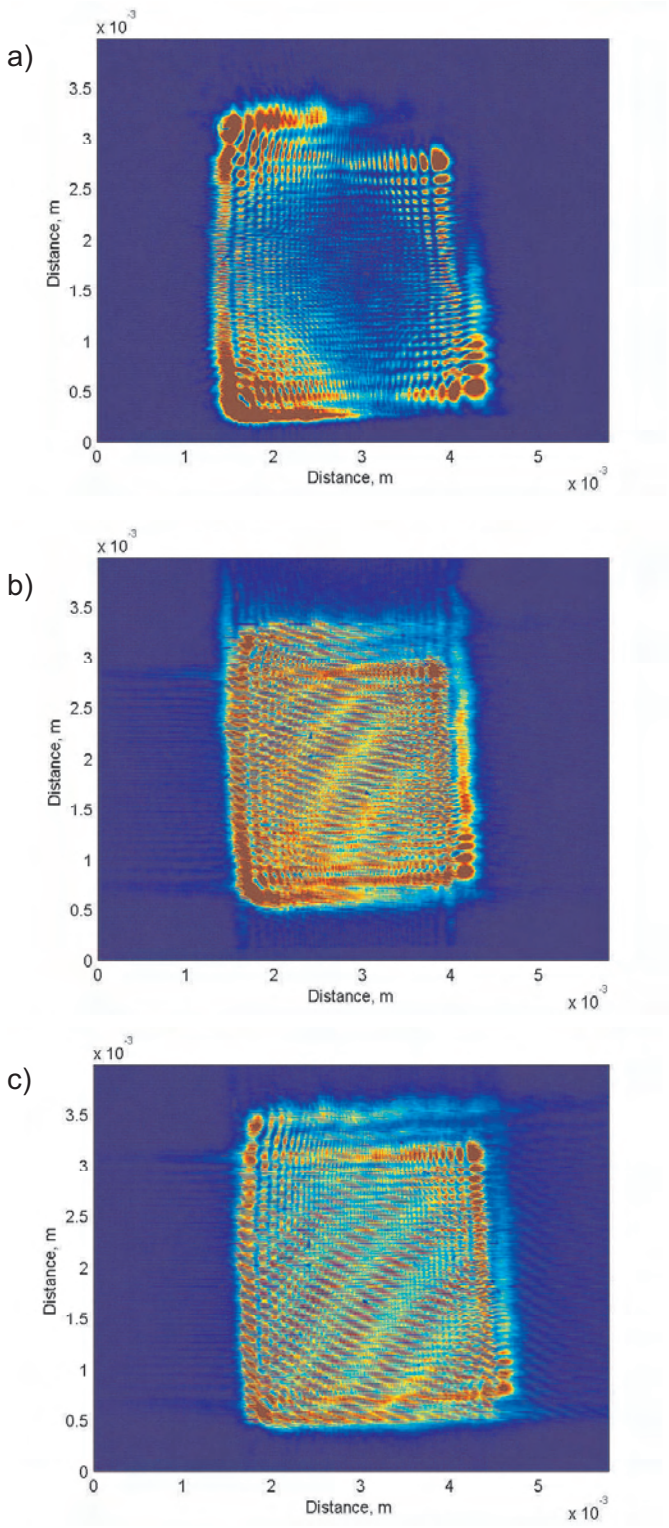

FIGURE 4.10: Profile of the HeNe laser beam through the tetra-prism with a working distance of 7 cm and a beam waist of a) 2 mm, b) 3 mm and c) 4 mm. These profiles demonstrate how the size of the beam waist affects the shape of the intensity profile produced using the tetra-prism heating method.

4.4 Conclusions

This chapter has described a novel substrate heating method based on a pyramid-shaped ZnSe tetra-prism in combination with a CO_2 laser. Experimental tests were performed that indicate the actual intensity pattern that results from combined diffraction and interference effects. It was also shown that the beam shape can be easily tailored to compensate for increased heat loss via radiative emission at the substrate edges and corners. The modelled substrate temperature distributions that result from different CO_2 laser-heating methods have been compared to the tetra-prism method. The model estimates that the standard deviation of the temperature profile on the deposition face of a 1 mm thick YAG substrate heated to 1076 K is 2.2 K. This is noticeably more homogeneous than other known CO_2 laser-heating methods, which produced modelled standard deviations greater than 7.3 K for substrates heated to similar temperatures.

Chapter 5

Femtosecond PLD of Nd:GGG

This chapter will present experimental results on the deposition of Nd:GGG on YAG substrates using a Ti:sapphire femtosecond laser. A systematic investigation of the deposition conditions and the effect of these conditions on the film properties will be discussed, including oxygen background pressure, target-substrate distance, substrate temperature, laser spot-size, fluence and laser repetition rate. It will be shown that highly textured growth of Nd:GGG material is possible at specific deposition parameters and that these differ to those necessary using a nanosecond laser (KrF excimer). An investigation of the ion-velocities produced from ablation of the target material using a planar Langmuir probe for both femtosecond and nanosecond lasers reveals the distinct differences in these two regimes.

This chapter will begin by presenting a review of the current efforts of short-temporal regime PLD of thin films, highlighting the key differences to the more conventional nanosecond laser regime.

5.1 Prior art

Table 5.1 shows a list of the materials deposited by short-temporal regime lasers with their relevant laser properties. One of the earliest examples of short pulse PLD was conducted in 1999 by Rode et al., who deposited carbon films using a 76 MHz repetition rate, low energy ($\sim$ 300 nJ), 60 ps pulse duration Nd:YAG laser at a wavelength of 1.064 µm. The films were shown to have a very high surface quality, with a density of particulates observed of less than one per mm^2 (visible with an optical microscope) and a very smooth surface with root-mean-squared (RMS) roughness of less than a nanometer.

Film composition	Substrate	Repetition rate	Wavelength	Pulse duration	Reference
Amorphous carbon	Si	76 MHz	1.064 µm	60 ps	Rode et al. (1999)
ZnO	Sapphire	10Hz	620 nm	90 fs	Millon et al. (2000)
TiN and BN	Si	10 Hz	780 nm	200 fs	Zhang et al. (2000)
PTFE, PHB, PGA, enzyme, pepsin and human teeth		10 Hz	248 nm	450 fs	Acquaviva et al. (2000)
SnO_2	Sapphire	10 Hz	780 nm	100 fs	Dominguez et al. (2002)
As_2S_3	Fused silica	76 MHz	532 nm	50 ps	Rode et al. (2002)
Er:$YAlO_3$ and Er:$Y_3Al_5O_{12}$	YAG	5 Hz	248nm	450 fs	Jelinek et al. (2002)
$BiTaO_3$	Si	10 Hz	620 nm	90 fs	Millon et al. (2003)
$Al_{65}Cu_{23}Fe_{12}$	Si	10 Hz	529 nm	250 fs and 1.3 ps	Teghil et al. (2003)
Diamond-like carbon	Si	1 kHz	800 nm	150 fs	Garrelie et al. (2003)
Silicon	Fused silica	1 kHz	775 nm	150 fs	Gamaly et al. (2004)
GaAs	Si	1 kHz	820 nm	150 fs - 500 ps	Trelenberg et al. (2004)
PTFE	Si	1 kHz	800 nm	120 fs	Womack et al. (2004)
$La_{0.5}Sr_{0.5}CoO_3$	MgO, Si and quartz	1 kHz	800 nm	50 fs	Brodoceanu et al. (2004)
3C - SiC nanoparticles	Si	1 kHz	800nm	120 fs	Dong & Molian (2004)
ZnO nanowires	Sapphire and Si	10 Hz	800nm	100 fs	Zhang et al. (2005)
TiC	Si	10 Hz	529 nm	250 fs	Teghil et al. (2006)
CdS	Quartz	1 kHz	800 nm	90 fs	Tong et al. (2006)
Carbon nitride	Si	10 Hz	248 nm	500 fs	Hopp et al. (2007)
Indium tin oxide	Glass	10 Hz	527 nm	250 fs	Teghil et al. (2007)
Nickle nanoparticles	Si	up to 200 kHz	1 µm	500 fs	Liu et al. (2007)
Indium	Si	2 Hz	800 nm	130 fs	Hafez & Elsayed-Ali (2007)

Table 5.1: Materials deposited using femtosecond and picosecond lasers.

The deposition rate was relatively high (2 - 6 Å/s) at a distance of 1.5 cm from the target, which is due to the high-repetition rate of the ablating laser. Of relevance to the current study in this thesis, and many other works on short-temporal regime PLD, work performed by Rode et al. (1999) is distinctly different: the high repetition rate of the laser effectively results in coupling between the plasma-plume and the successive pulses. This means that the energy of the laser is imparted into the heating volume during the formation of the plasma-plume, resulting in laser-plume interactions that would otherwise not occur with repetition rates less than a few MHz. Also the relatively long pulse durations (60 ps) mean that thermal relaxation of the irradiated volume may occur during the laser exposure. Rode et al. (2002) have deposited chalcogenide glass (AsSe) for waveguide applications using a similar picosecond laser (50 ps pulse duration laser at a wavelength of 520 nm). The measured loss of the waveguide was relatively low (0.2 dB/cm) and the density of particulates observed on the surface of the film was found to be less than on typical nanosecond-laser deposited films.

By using a spatially shaped pulse, Gamaly et al. (2004) have demonstrated a reduction in the number of particulates on the surface of the silicon films deposited using a 150 fs pulse duration, 775 nm wavelength laser at a repetition rate of 1 kHz with pulse energy of 0.42 mJ. In this work it is suggested that the low-intensity wings of the irradiating pulse are responsible for low-energy phase transformations, such as amorphisation, surface damage, and melting, which is believed to produce a mixture of phases in the laser plume such as liquid droplets, flakes, and micron-sized particles. By shaping the pulse using an aperture, these low-energy phase transformations can be reduced.

Millon et al. (2000) have demonstrated the deposition of epitaxial ZnO films onto sapphire using a 90 fs pulse duration laser with $\sim$ 1 mJ per pulse, 10 Hz repetition rate laser at a wavelength of 620 nm. The films were shown to consist of grain structures a few hundred nanometers in size. Rocking curve analysis around the (0002) film peak revealed a FWHM of 1.3°, compared to 0.007° for epitaxial ZnO films deposited by nanosecond excimer KrF lasers (Choopun et al. 1999). Millon et al. (2003) have also demonstrated the deposition of textured $BaTiO_3$ onto SiO_2/Si and MgO substrates using this laser system. The results revealed that the films consisted of coalesced particulates up to 1 µm in size with a crystallised $BaTiO_3$ phase. The X-ray diffraction analysis revealed broad diffraction peaks, corresponding to the textured $BaTiO_3$ growth with a very small crystallite size (12 nm).

One of the most promising candidate materials for femtosecond PLD is diamond-like carbon. The high-energy ions produced from the femtosecond ablated plume is predicted to result in implantation of the carbon species into the substrate (Garrelie et al. 2003), increasing the adhesion by forming a transition layer between the film and substrate. Diamond-like carbon films deposited by femtosecond PLD exhibit a lower internal stress than those deposited by conventional nanosecond PLD, which improves the coating adhesion to the substrate (Loir et al. 2004), and is particularly useful for tribological applications (articular prosthesis) where the adhesion of the coating is of crucial importance for the longevity of the film.

The first examples of the deposition of garnet crystal using a femtosecond laser was conducted by Jelinek et al. (2002) with a KrF excimer laser ($\lambda = 248\,\text{nm}$), combined with a a dye laser amplifier of pulse duration 450 fs, repetition rate 5 Hz and energy per pulse 5 mJ. They deposited yttrium aluminium garnet (YAG) and yttrium aluminium perovskite (YAP) onto YAG, YAP, fused silica and sapphire substrates. The films were shown to be covered in droplets up to 5 µm in size. Figure 5.1 shows an SEM micrograph of a film deposited on silicon using an Er:YAG target. X-ray diffraction analysis of YAG films deposited onto sapphire revealed that they consisted of polycrystalline YAG with a dominant presence of the $Y_4Al_3O_9$ phase (one peak detected corresponding to the YAG (220) plane and 5 to the $Y_4Al_3O_9$ phase). It was observed that the laser spot-size influenced the size of the droplets on the surface of the film. For larger ablation spot areas

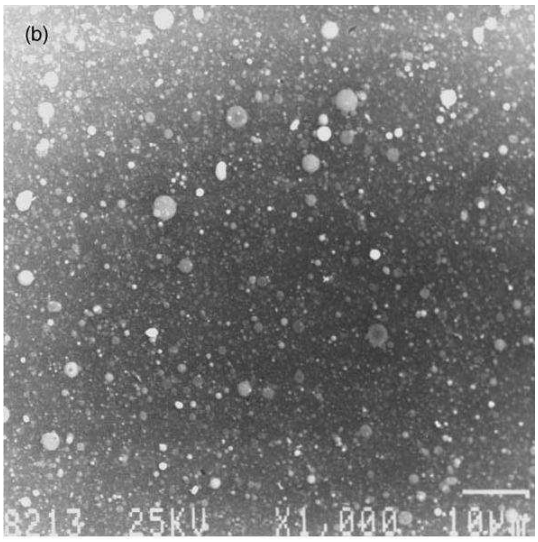

FIGURE 5.1: SEM of a film deposited with an Er:YAG target on Si using a femtosecond laser with a pulse duration of 450 fs, a repetition rate of 5 Hz and energy per pulse of 5 mJ (Jelinek et al. 2002).

(30×10^{-4} cm^2) droplets with diameters of less than 1 µm were detected, while for smaller spot-sizes (6×10^{-4} cm^2), droplets with larger diameters were observed of up to 5 µm. In this work (Jelinek et al. 2002), a comparison with KrF excimer nanosecond laser-deposited films (YAG on sapphire) revealed that they were also covered with droplets but with a lower density on the surface compared to the femtosecond laser-deposited films.

Nitride films (TiN and BN) have been deposited by Zhang et al. (2000) onto silicon substrates using a Ti:sapphire femtosecond laser with a pulse duration of 200 fs, repetition rate of 10 Hz, pulse energy of 20 mJ and a wavelength of 780 nm. The TiN film growth was observed by reflection high-energy electron diffraction (RHEED) and was found to initially form single-crystal material that subsequently converted to polycrystalline films as the film thickness increased (after 30 minutes of deposition). The films deposited using a nanosecond laser (frequency-tripled Nd:YAG) were shown to be characteristically different: initially growing epitaxial material that formed into highly textured films as the film thickness increased. An investigation of the ion-energy distributions revealed that both the boron and nitrogen ions in the femtosecond laser-produced plasma were much higher in energy than for the nanosecond laser case. It is suggested that the high kinetic energy particles result in either disoriented nucleation or disorientation of the islands (Zhang et al. 2000), which may explain the growth of polycrystalline films for the femtosecond PLD experiments.

More recently, crystalline ZnO nanowires have been grown by femtosecond PLD (Zhang et al. 2005) using a Ti:sapphire laser with 100 fs laser pulses at a wavelength of 800 nm. The benefit of femtosecond PLD (Zhang et al. 2005) for this technique is minimal formation of large (greater than 1 µm) particulates during the ablation process (observed for ZnO films deposited by Millon et al. (2000)), which can disrupt the growth of the nanowires. The homogeneity of femtosecond laser produced precursor vapour has been attributed to the good crystalline characteristics of nanowires with reasonably uniform diameters.

5.2 Experimental

Figure 5.2 shows the experimental set-up used for the femtosecond PLD experiments. The experiments were conducted in a vacuum chamber using oxygen as a background gas. A Ti:sapphire laser was used to ablate the target material with 130 fs pulses at a wavelength of 800 nm operating at a repetition rate of 10 Hz or 1 kHz. The target material was ablated with single pulse energies which varied from 0.1 to 1.2 mJ. Experiments were conducted for a range of spot-sizes (elliptical in shape due to the laser beam angle of incidence) ranging from 32 µm by 45 µm to 135 µm by 195 µm, corresponding to fluences ranging from 1.3 to 19 J/cm^2. The substrates were heated using a 25W CO_2

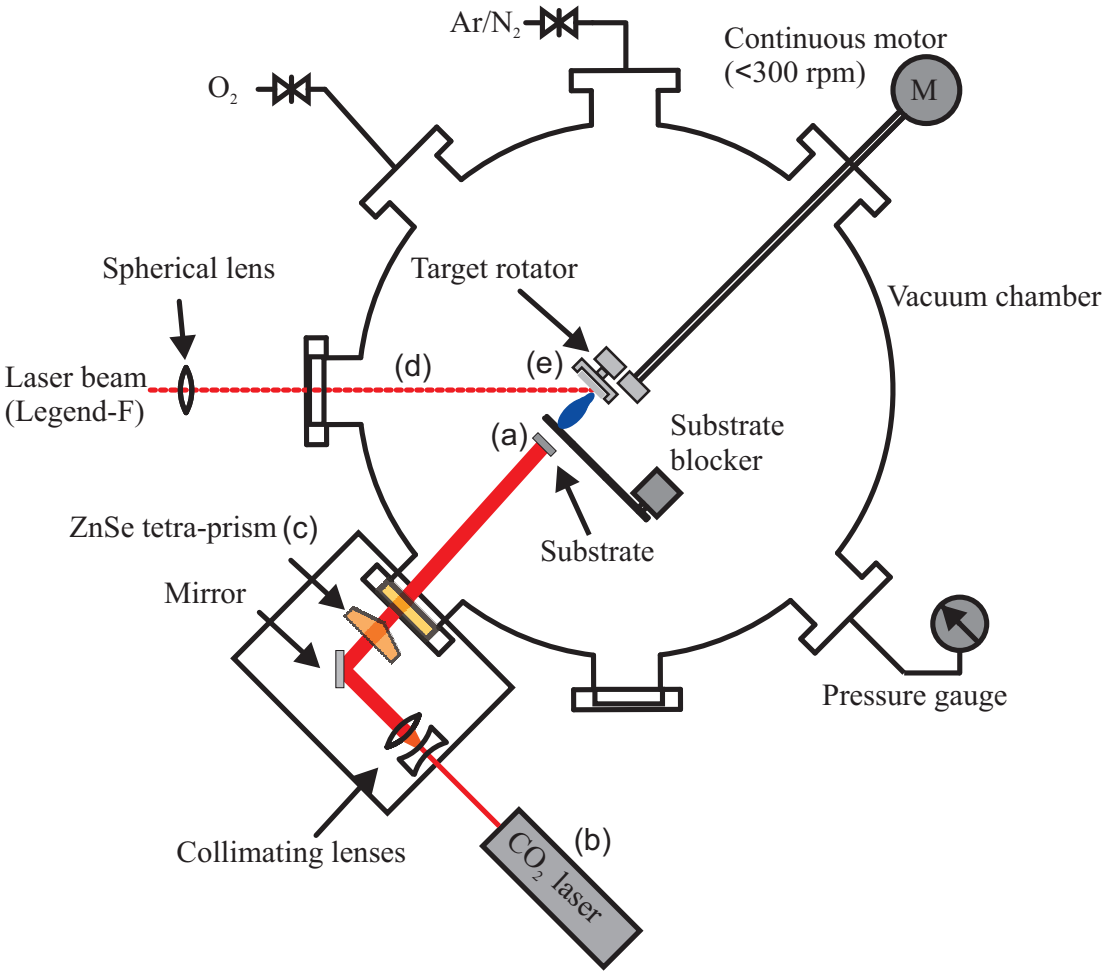

FIGURE 5.2: Experimental set-up for femtosecond PLD. The substrate (a) was heated using a 25W CO_2 10.6 µm wavelength laser (b) with the beam homogenised onto the back-face of the substrate using a ZnSe tetra-prism (c). The ablating laser beam (d) was focused onto the target (e) using a fused quartz lens. The target was rotated to produce an epitrochoidal laser ablation track.

10.6 µm wavelength laser, homogenised onto the back-face of the YAG substrate using either a ZnSe tetra-prism (see chapter 4) or a brass reflective beam pipe. Trial depositions were conducted for a duration of 10 minutes using an undoped GGG or Nd:GGG (1 at. % doped) target and once the conditions for epitaxial growth were established, films were grown for successively longer durations. The target-substrate distance was set to either 2.5, 3, or 4.5 cm. A remotely controlled substrate-shutter was used to prevent the plume from reaching the substrate during pre-deposition ablative cleaning of the target surface. The spot-size, and hence the incident laser fluence was estimated using the knife-edge technique. The deposition chamber was evacuated to a pressure below 10^{-4} mbar prior to deposition, and oxygen was then continuously introduced into the chamber to maintain the desired pressure for each experiment.

5.2.1 The femtosecond laser system

The femtosecond pulses were obtained from a regenerative amplifier (*Legend-F*) seeded by a Kerr lens mode-locked Ti:sapphire femtosecond laser (*MIRA-900*). This system provided 130 fs pulses with energy < 2.5 mJ at a wavelength of 800 nm, with a repetition rate of ≤ 1 kHz. Precise measurement of the pulse duration was performed using a standard second harmonic autocorrelator, yielding a value of 130 ± 5 fs (FWHM).

The system consists of several autonomous units: namely an oscillator, which produces low energy ultrashort-duration pulses, a stretcher that converts the femtosecond pulses into longer duration chirped pulses (100-200 ps), an amplifier stage to increase the pulse energy by several orders of magnitude and finally a compression stage that performs the reverse function of the stretcher, returning the pulse durations to the same as the oscillator. Figure 5.3 shows a schematic of the individual components (purchased from *Coherent plc*) making up the femtosecond laser system. The oscillator is pumped with a frequency-doubled Nd:YAG laser at a wavelength of 532 nm (*Verdi-10*). The pulses from the oscillator are used as a seed for the regenerative amplifier, which is pumped by a Q-switched solid-state (Nd:YLF) laser at a wavelength of 527 nm (*Evolution-30*). The seed pulse undergoes many (~ 9) round trips of the regenerative amplifier, where it is amplified through chirped pulse amplification.

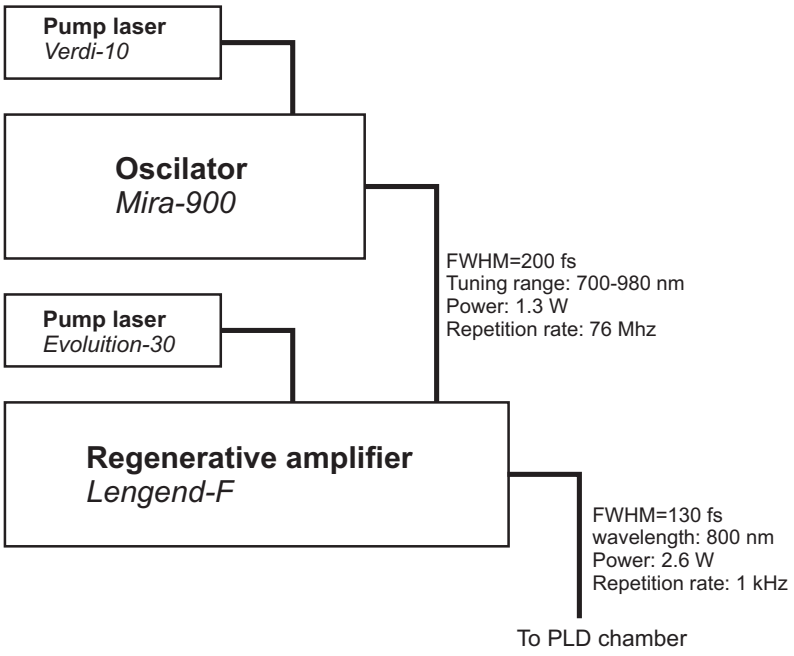

FIGURE 5.3: Schematic of the femtosecond laser system used for PLD experiments. The oscillator and the regenerative amplifier was pumped by a solid-state laser (*Verdi-10* and *Evolution-30*). The oscillator (*Mira-900*) was used as the seed for the regenerative amplifier (*Lengend-F*). The system produced $< 2.6\,\mathrm{mJ}$ energy pulses of $130 \pm 5\,\mathrm{fs}$ duration at a wavelength of 800 nm, with a repetition rate of 1 kHz.

5.2.1.1 Kerr-lens mode-locked laser

The femtosecond pulse used for the seed pulse for the regenerative amplifier is mode-locked; that is the pulse is made up of a superposition of many laser modes. The pulse is transform limited, such that its duration is $\tau_L \sim 1/\Delta\nu$, where $\Delta\nu$ is the bandwidth. The Ti:sapphire crystal has a large gain curve ranging from 600 to 1100 nm, the largest of any known material, a high saturation fluence of nearly $1\,\mathrm{J/cm^2}$, which makes it ideal for mode-locked amplifiers. The Ti:sapphire crystal acts as a focusing lens through the Kerr nonlinearity when the pulse intensity exceeds $\sim 10^{11}\,\mathrm{W/cm^2}$. A single short-pulse is left in the oscillator by blocking the unfocused cw modes with a slit, and dispersion compensation is used to correct for the inherent dispersion in the system. Femtosecond pulses ($< 200\,\mathrm{fs}$) within a tuning range of 700-980 nm are produced with pulse energies of a few nJ.

5.2.1.2 Regenerative amplification

The femtosecond pulses from the oscillator (*Mira-900*) have an energy of a few nJ. The next stage of the amplification involves increasing this energy by a factor of 10^3 through the method of regenerative amplification. The femtosecond pulses are stretched by a factor of $\approx 10^3$, using a pair of gratings before the seed pulse is injected into the amplifier. The gain medium is pumped for a short time with a solid state pulsed laser (*Evolution-30*) and accumulates energy, then the initial seed pulse is injected into the resonating cavity through an electro-optic switch and undergoes a number of round-trips. The pulse is then compressed to the same duration as the seed pulse using a pair of gratings.

5.2.1.3 Amplified spontaneous emission

Amplified spontaneous emission (ASE) is an undesirable effect produced in the gain medium of the laser and is an important consideration when ablating with femtosecond pulses, since the high amplification can lead to a significant amount of ASE. The ASE pulses are typically nanoseconds in duration (Cha et al. 2007, Ivanov et al. 2003). They are present before and after the main output pulse, however, their affect on the ablation process is considered negligible as their intensity ($< 3\times10^8$ W/cm^2) is not high enough to lead to nonlinear absorption mechanisms, which are necessary for ablation of Nd:GGG in this wavelength regime. Measurements were taken to confirm this. The power of the amplified spontaneous emission (ASE) was measured as roughly 1.5 % of the main femtosecond pulse without any injection seed pulse into the final amplifier (*Legend-F*). The laser manufacturer's data-sheet specifies a contrast (the level of the main pulse intensity relative to the pre-pulse) of $> 1000 : 1$. In normal amplified femtosecond operation we have a range of energy densities due to the ASE prepulse on the target from 0.0016 to 0.019 J/cm^2. Furthermore, the absorption coefficient of target material, Nd:GGG (1.6 at. % doped), at 800 nm is roughly 2 cm^{-1}. The intensities of the pre-pulses ($< 3 \times 10^8$ W/cm^2) are not high enough to be absorbed through multi-photon mechanisms, for which an intensity of roughly 10^{13} W/cm^2 is required. Therefore the target is not damaged or ablated until the main pulse arrives.

5.2.2 Spot-size measurements

The ablating spot-size of the incident laser was characterised using the knife-edge technique. The method involves scanning an opaque edge transversely across the beam profile while detecting the corresponding laser energy. Assuming the laser has a Gaussian beam profile, the whole intensity profile is given by

$$I(x,y) = I_0 \left(\frac{w_0}{w(z)}\right)^2 \exp\left[-2\frac{(x^2+y^2)}{w^2(z)}\right], \tag{5.1}$$

and

$$w(z) = w_0 \left[1 + \left(\frac{\lambda z}{\pi w_0^2}\right)^2\right]^{1/2}, \tag{5.2}$$

where I_0 is the peak intensity, w_0 is the minimum waist at the focus, given by

$$w_0 = \frac{\lambda f}{\pi w_l}, \tag{5.3}$$

where f is the focal length of the focusing lens and w_l is the beam radius at the lens.

When characterising the beam profile using the knife-edge technique, the intensity is integrated in x and y directions (both orthogonal to the direction of the laser: z). Assuming the motion of the knife-edge is in the x-direction, the integration in the y-direction can be carried out analytically and can be considered to be constant. The integration in the x-direction has no analytical solution and the error function must be used. Integrating equation 5.1 in the x and y directions gives the power measured as a function of scanning distance x:

$$P(x) = I_0 \frac{w_0^2}{4}\pi \operatorname{erfc}\left(\frac{\sqrt{2}}{w(z)}(x - x_0)\right), \tag{5.4}$$

where x_0 is the distance to the centre of the beam profile. The beam was characterised for various distances from the minimum waist (corresponding to a lens to target distance of 40 cm) using a translation stage with an accuracy of ± 1 µm. The measured power as a function of translational distance x was fitted to equation 5.4 to estimate the beam waist $w(z)$. Figure 5.4 shows the measured power as the knife-edge is transversely moved across the beam profile for various distances from the minimum waist ($z = 0.0$, 1.0, 2.5, 5.0 and 7.5 mm). A graph of the beam waist estimates against distance from the focus (the focus corresponds to $z = 0$) is shown in the inset of figure 5.4 and is fitted to

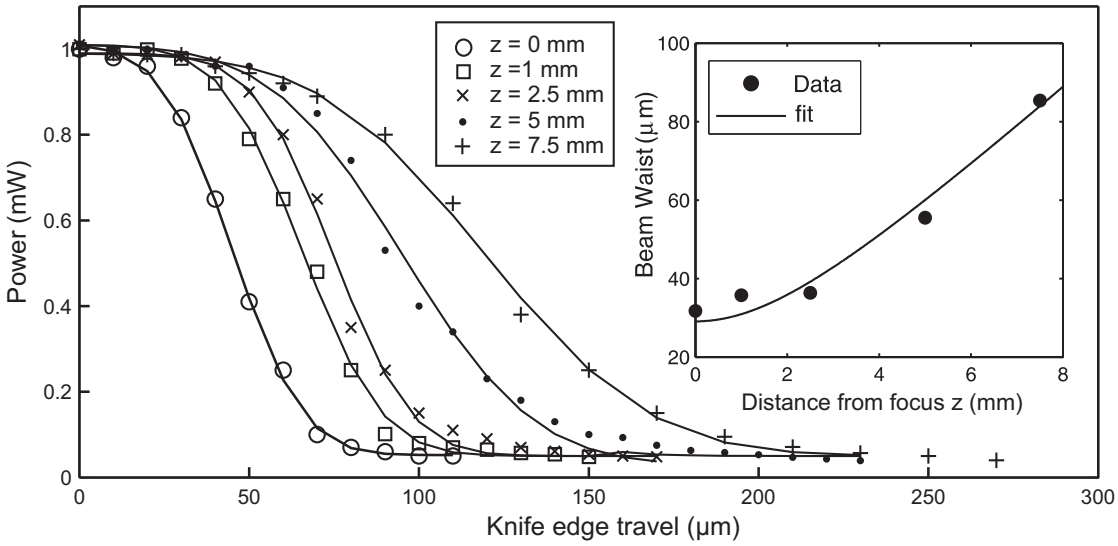

FIGURE 5.4: Measurements of the femtosecond laser beam power as function of translational distance of the knife-edge for various distances from the focus (the focus is defined as $z = 0$). The corresponding estimates of the beam waists are shown in the inset.

a Gaussian beam profile. The spot-size of the laser at the target was estimated by interpolating from this Gaussian fit.

To be precise, the fluence due to an irradiating pulse with a Gaussian profile is not single-valued and the area of the material that is ablated is dependent on the pulse power and the ablation threshold of the material. A more precise definition of the ablation spot would be the area exposed to an above-threshold fluence. However, this definition is material specific and the ablation threshold for GGG with femtosecond lasers is not well known. For clarity we define the *ablation spot-size* as the major and minor axis radii of an ellipse encompassing a laser intensity of $\geq 1/e^2$ of the peak intensity at the target's surface. Our calculation of fluence is based on this measurement: we define the fluence by

$$F = \frac{E}{\pi w_{\text{maj}} w_{\text{min}}}, \tag{5.5}$$

where E is the pulse energy, w_{maj} and w_{min} are the major and minor axis radii of an ellipse with area $\pi w_{\text{maj}} w_{\text{min}}$. For a laser incident angle of θ, $w_{\text{maj}} = w_{\text{min}}/\sin\theta$. The intensity distribution of the irradiating laser beam on the target surface is approximately given by

$$I(s_x, s_y) = I_0 \exp\left[-2\left(\frac{s_x^2}{w_{\text{maj}}^2} + \frac{s_y^2}{w_{\text{min}}^2}\right]\right), \tag{5.6}$$

where s_x and s_y are the distances on the target surface from the centre of the beam in the direction of the minor and major axis, respectively.

5.2.3 Epitrochoidal target rotation

The target was rotated such that the laser ablation track approximately followed an epitrochoidal path on the surface of the target. This significantly increased the usable area and longevity of the target. It is an important design feature compared to typical nanosecond PLD apparatus as the focused spot-size for femtosecond deposition ($\sim 50\,\mu$m) is a few orders of magnitude smaller than for nanosecond PLD ($\sim 1\,$mm). The small laser ablation area and the high laser repetition rate means that deep ablation channels are rapidly formed on the target material if the target is rotated about a single axis. A rotating mechanism was introduced to overcome this and is depicted in figure 5.5. The mechanism consisted of two discs (one attached to a pivoting arm)

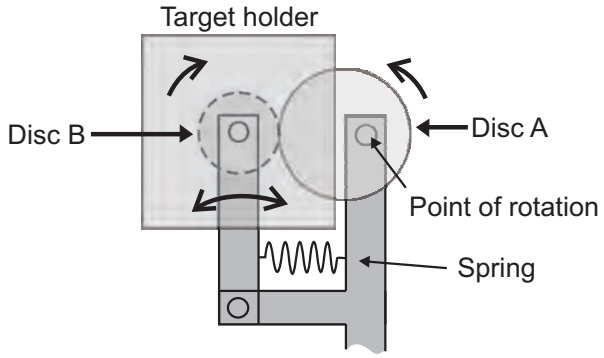

FIGURE 5.5: Schematic diagram of the epitrochoidal rotation mechanism. Disc A is rotated off-center and rotates disc B in the opposite direction while moving the target from side-to-side in one period of rotation.

held together with a spring with viton o-rings on the outer edges to improve grip during rotation. The point of rotation of one of the discs was off-center and the other disc held the target holder. The diameters were carefully chosen to ensure that the ablation track was not repeated upon rotation (i.e. the circumferences were not integer multiples of each other). Figure 5.6 shows a GGG target that has been rotated with an inner and outer radius of 0.8 and 2.1 cm. In this case, the majority of the target surface area is used for ablation and crater-formation only occurred at the inner edges of the ablated area after a relatively long time of target usage ($\sim 1\,$hour). Crater-formation had a detrimental effect on the transfer of target material to the substrate, which was noticed by a change in the plume direction when the laser was incident at these regions. When this occurred, the target was lapped to a flat surface. To minimize the overlap from successive pulses during deposition, the target was rotated at relatively high speeds

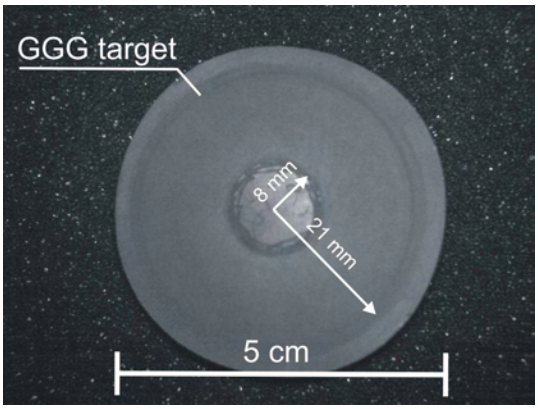

FIGURE 5.6: Photograph of a GGG target that was rotated during a deposition run with a lateral motion of 1.3 cm.

(~ 4 rev. per second). This resulted in a minimum distance between successive ablated areas on the target surface of roughly 200 μm (for laser repetition rate of 1 kHz).

5.2.4 Substrate heating and temperature calibration

The substrates were heated using a 25 W 10.6 µm wavelength CO_2 laser, with the Gaussian beam homogenized onto a 1 cm $\times$ 1 cm square substrate either using a brass reflective beam-pipe or a ZnSe tetra-prism. This laser-heating method is described in chapter 4. The temperature of the substrates was calibrated using a thermocouple attached to the surface of a $Y_3Al_5O_{12}$ (YAG) substrate. The temperature was measured under a pressure of 0.1 mbar. Figure 4.8 (see page 29) shows a graph of the incident power on YAG substrate plotted against the measured substrate temperature for the tetra-prism heating method. This data was used to give an indication of the substrate temperature.

5.2.5 Ion probe analysis

The ion emission flux of the plasma produced from femtosecond and nanosecond ablation regimes was characterised using a planar Langmuir probe. For nanosecond ablation, measurements were carried out in a second chamber[1] using a KrF excimer laser operating at a wavelength of 248 nm, with a pulse duration of ≈ 25 ns and pulse energy of 50 mJ. The laser spot-size at the target was 1 mm $\times$ 4 mm. The probe consisted of a copper plate of dimension 2×2.5 mm^2 for nanosecond ablated ion characterisation and 2.5×5 mm^2 for femtosecond ablated ion characterisation.

[1]This analysis was conducted in collaboration with J. Lunney and T. Donnelly (Trinity College Dublin)

For each measurement the probe was biased at $-30\,\mathrm{V}$, and the collected ion current was determined by the voltage signal recorded on a digital oscilloscope across a load resistor ($10\,\Omega$). The bias was maintained using a $1.2\,\mu\mathrm{F}$ capacitor. A diagram of the probe circuit (used for measurements of femtosecond ablated ions) is shown in figure 3.2 (see page 18). The Nd:GGG target, placed on a rotating target holder (epitrochoidal rotation was used for femtosecond ablation only), was ablated under vacuum conditions ($< 10^{-4}\,\mathrm{mbar}$). The time of incidence of the laser pulse was measured by calibrating the trigger output signal from the regenerative amplifier with a photo-diode measurement at the target. This was also confirmed by the detection of a photo-peak from the Langmuir probe. For measurements of ion signals for both the femtosecond and nanosecond regimes, the laser was operated on single-shot mode. The velocity distribution was calculated from $n = I/AvQ$, where n is the ion density, I is the probe current, A is the surface area of the probe, v is the flow velocity of the ions (calculated from TOF spectra) and Q is the ion charge (singly charged ions have been assumed). This could only be used for the characterization of ion velocities in a vacuum ($< 10^{-4}$), since the background gas plays a significant role in affecting the ion velocities.

5.3 Results

5.3.1 Optimisation of growth conditions

Table 5.2 shows the deposition conditions of films deposited on YAG (100) by femtosecond PLD using a Nd:GGG (1 at.% dopped) or undoped GGG target. The deposition parameters of background oxygen pressure, target-substrate distance, temperature, spot-size, pulse energy, laser repetition rate and duty cycle were all investigated. The effect of each of these deposition parameters on the crystallinity of the grown films was investigated by XRD, SEM, AFM and EDX analysis (EDX for selected films). All the XRD spectra were normalised to the position of the YAG (400) substrate peak. SEM and AFM analysis was undertaken on the centre of the film. Masking of the substrate (by the substrate holder) provided areas where the film is not deposited, and film thicknesses were measured using a surface profilometer (*Tencor P16*) at these regions. Measurements are presented as the range of thicknesses measured (min – max) at the four corners of the film.

A rough indication of the optimum deposition conditions was found by depositing a series of films with a constant deposition parameter and investigating crystalline quality

of these films using XRD analysis. The quality of the films was determined from the FWHM of the XRD peaks corresponding to the desired phase (with a higher quality film revealing a lower FWHM).

A series of films was deposited with an oxygen background gas pressure of 10^{-3}, 10^{-2} 10^{-1} mbar, with the other conditions of fluence, target-distance and ablation spot-size constant kept constant (films 1-3). The optimum oxygen pressure was found to be 10^{-1} mbar (film 3). A series of films was then deposited under an oxygen pressure of 10^{-1} mbar with fluences between 1.6 and 13 J/cm^2 (for constant pulse energy) (films 4-7) and 1.3 to 7 J/cm^2 (for constant ablation spot-size) (films 8-11). Films were also deposited with various substrate temperatures with constant fluence, pressure and target substrate distance (films 12-15). Another series of films was deposited with various target-substrate distances with constant fluence, pressure and temperature (films 16-17). All the films were then analysed by XRD to determine which conditions resulted to highest quality film. The highest quality film was found to be film 16. A final investigation of the effect of laser repetition rate and duty cycle on the quality of the films was then conducted using the optimum conditions. The following sections will describe these finding in more detail.

Film	Pres. (mbar)	Dist. (cm)	Temp. (°C)	Abl. spot-size, (μm)	Pulse energy (mJ)	Fluence (J/cm^2)	Rep. rate (duty cycle)	Duration (min)
Varying pressure								
1	10^{-3}	3	850	65 by 95	1.17	6.2	1 kHz	10
2	10^{-2}	3	850	65 by 95	1.17	6.2	1 kHz	10
3	10^{-1}	3	850	65 by 95	1.17	6.2	1 kHz	10
Varying fluence (constant energy)								
4	10^{-1}	4.5	850	45 by 65	1.2	13	1 kHz	10
5	10^{-1}	4.5	850	56 by 75	1.2	9.1	1 kHz	10
6	10^{-1}	4.5	850	90 by 135	1.2	3.1	1 kHz	10
7	10^{-1}	4.5	850	123 by 195	1.2	1.6	1 kHz	10
Varying fluence (constant spot-size)								
8	10^{-1}	4.5	800	57 by 80	1.0	7.0	1 kHz	10
9	10^{-1}	4.5	800	57 by 80	0.80	5.7	1 kHz	10
10	10^{-1}	4.5	800	57 by 80	0.56	3.9	1 kHz	10
11	10^{-1}	4.5	800	57 by 80	0.18	1.3	1 kHz	10
Varying temperature								
12	10^{-1}	4.5	750	45 by 65	1.1	12	1 kHz	10
13	10^{-1}	4.5	820	45 by 65	1.1	12	1 kHz	10
14	10^{-1}	4.5	900	45 by 65	1.1	12	1 kHz	10
15	10^{-1}	4.5	970	45 by 65	1.1	12	1 kHz	10
Varying target-substrate distance								
16	10^{-1}	2.5	850	32 by 45	0.85	19	1 kHz	10
17	10^{-1}	4.5	850	32 by 45	0.85	19	1 kHz	10
Optimised film (2 hour deposition)								
18	10^{-1}	4.5	850	32 by 45	0.85	19	1 kHz	120
Varying repetiton rate and duty cycle								
19	10^{-1}	2.5	850	32 by 45	0.9	20	1 kHz	10
20	10^{-1}	2.5	850	32 by 45	0.9	20	1 kHz (200/200)*	20
21	10^{-1}	2.5	850	32 by 45	0.9	20	1 kHz (50/50)*	20
22	10^{-1}	2.5	850	32 by 45	0.9	20	1 kHz (1000/1000)*	20
23	10^{-1}	2.5	850	32 by 45	0.9	20	10 Hz	100
24	10^{-1}	2.5	850	32 by 45	0.9	20	1 kHz	1

TABLE 5.2: Conditions of femtosecond PLD experiments (*duty cycle $x/y = x$ pulses on, y pulsed off).

5.3.1.1 Effect of changing pressure

Results from XRD analysis of films deposited under various oxygen pressures are shown in figure 5.7. The spectra are off-set on the intensity axis for clarity. These results reveal that the $Gd_3Ga_5O_{12}$ phase occurs preferentially at higher oxygen pressures (at these deposition conditions). Lower pressures resulted in polycrystalline films dominated by the Ga-deficient phase $Gd_3(GaO_4)O_2$, which is clearly identified in figure 5.7(d). The FWHM of the $Gd_3Ga_5O_{12}$ (400) peak is 0.5°. The peak corresponding to the (211) lattice planes from the $Gd_3(GaO_4)O_2$ phase is present at a relativity high pressure of 0.1 mbar, although it is significantly diminished in intensity compared to the films deposited at lower pressures. Aside from the corresponding GGG and YAG (800) peaks, other film peaks were not observed outside of the range of data presented. The absence of other peaks corresponding to the $Gd_3Ga_5O_{12}$ phase indicates this film has grown in the expected crystalline (100) orientation. The film thicknesses were measured to be 0.6-2.00 µm (0.1 mbar), 0.6-2.5 µm (0.01 mar) and 0.6-2.5 µm (0.001 mbar). By scanning the profiler needle along the surface of the films it was revealed that there was a large fluctuation in the height from the surface of the substrate. This was due to the presence of large particulate-like structures on the surface of the films, and this was confirmed by SEM analysis. Figure 5.8 shows an SEM micrograph of a film deposited at a pressure of 0.1 mbar (film 1). Visible on the film are particulates approximately $\leq$0.5 µm in size that cover the film.

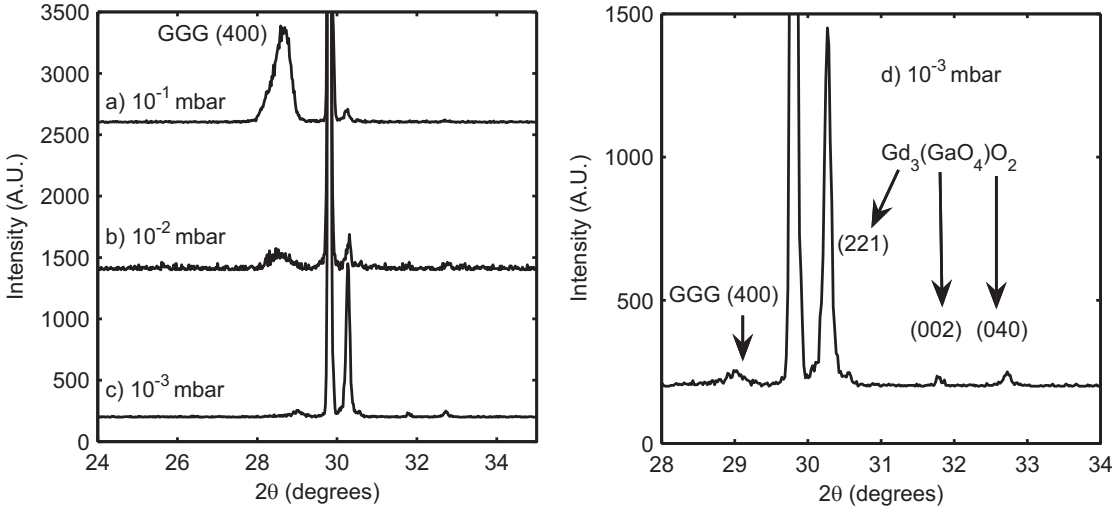

FIGURE 5.7: XRD spectra from GGG films 1-3 deposited under oxygen pressures of a) 0.1 mbar (film 3); b) 10^{-2} mbar (film 2); c) 10^{-3} mbar (film 1); d) 10^{-3} mbar (peaks identified) (film 1).

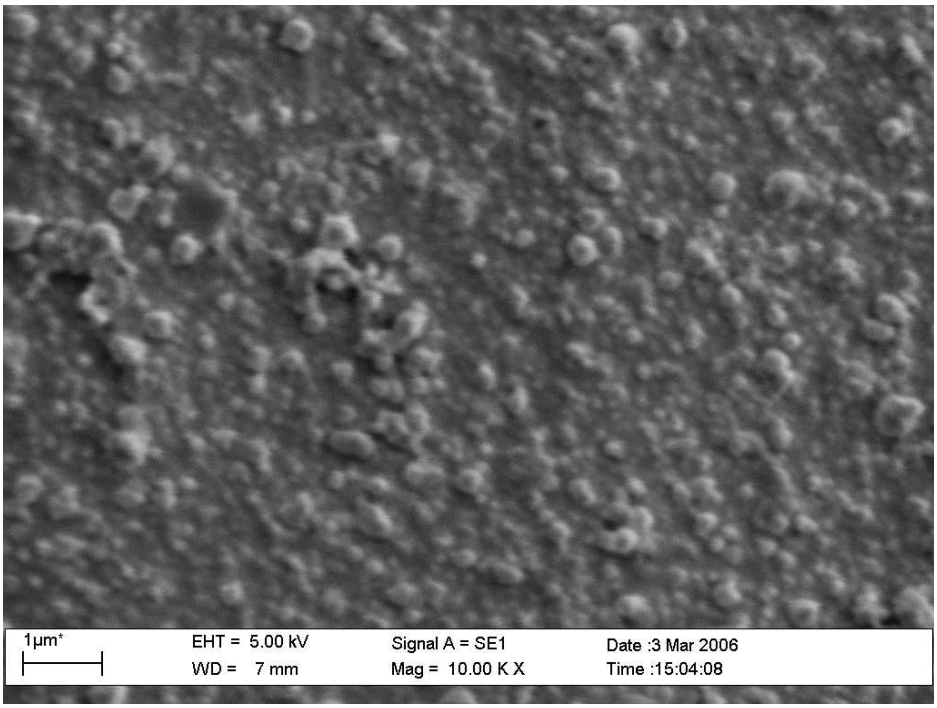

FIGURE 5.8: SEM micrograph of a film deposited at a pressure of 0.1 mbar (film 1).

The visible appearance of the film deposited at a pressure of 0.1 mbar (film 1) was clear with only a slight frosty trace. Films deposited at pressures of 0.01 mbar and 0.001 mbar were noticeably more opaque (films 2 and 3).

A deposition was also conducted at a pressure of 0.01 mbar, using a spot-size of 32 by 45 µm, a pulse energy of 0.85 mJ (corresponding fluence of 19 J/cm^2), a temperature of 850°C and a target-substrate distance of 4.5 cm. XRD analysis revealed that the GGG phase was not present. The film's appearance was white and frosty, noticeably more opaque than films deposited at higher pressures for the same laser conditions.

5.3.1.2 Effect of changing fluence (constant energy)

Figure 5.9 shows XRD spectra for films deposited using laser fluences (with constant energy per pulse) ranging from 1.6 J/cm^2 to 13 J/cm^2 and ablation spot-sizes ranging from 45 µm by 65 µm to 137 µm by 195 µm. All other deposition parameters were kept the same and are listed in table 5.2 (films 4-7). These results show that the optimum fluence for epitaxial growth (under these conditions) was above 3.1 J/cm^2 and lower fluences gave rise to multi-phase growth of GGG and other anomalous phases, which have not been possible to unambiguously assign. The FWHM of the (400) peak was 0.2° for

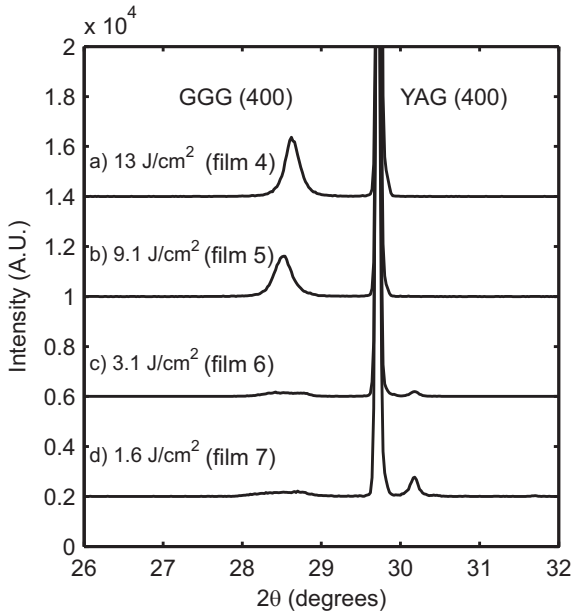

FIGURE 5.9: XRD spectra from GGG films $4-7$ deposited with a laser fluence (and *ablation spot-size*) of a) 13 J/cm^2 (45 µm by 65 µm), b) 9.1 J/cm^2 (56 µm by 75 µm), c) 3.1 J/cm^2 (90 µm by 135 µm) d) 1.6 J/cm^2 (123 µm by 195 µm). Film thicknesses were measured to be a) $80-120$ nm; b) $80-130$ nm; c) $40-70$ nm; d) $60-70$ nm.

films deposited above 9.1 J/cm^2, which is a clear improvement on the crystalline quality of film 3 (with a FWHM 0.5°). Although the films were considerably thinner, with measured thicknesses ranging from 80 - 120 nm (13 J/cm^2), 80 - 130 nm (9.1 J/cm^2), 40 - 70 nm (3.1 J/cm^2) and 60 - 70 nm (1.6 J/cm^2). The thinner films can be explained by the larger target-substrate distance and the smaller ablation spot-size used for these depositions, resulting in less material being ablated and less material reaching the substrate. A notable observation is the position of the GGG (400) peak for fluences of 9.1 and 13 J/cm^2. The peak position for the film deposited at a higher fluence of 13 J/cm^2 is 0.12 degrees higher, closer to the bulk (400) peak position of 28.839 ° (Sawada 1997) at a 2θ position of 28.63 °, indicating a lattice parameter that better matches stoichiometric GGG.

The appearance of the films 4-7 was again clear with only a slight frosty trace. Figure 5.10 shows an SEM micrograph of a film deposited at a fluence of 9.1 J/cm^2 (film 5). This evidence reveals that the film was covered in microscopic particulates roughly 0.5-1 µm in size, and it was not noticeably different from the surface of film 1.

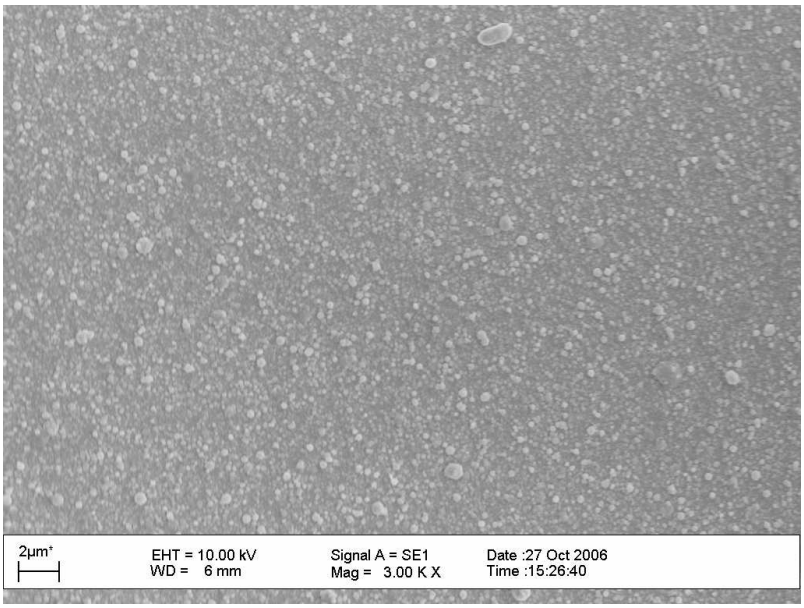

FIGURE 5.10: SEM micrograph of a film deposited at a fluence of 9.1 J/cm^2 (film 5).

5.3.1.3 Effect of changing fluence (constant spot-size)

Figure 5.11(a)-(d) shows XRD spectra of films deposited with various fluences (with a constant spot-size of 57 by 80 µm). The energy per pulse ranged from 1 to 0.18 mJ. All the films (8-11) produced diffraction peaks that corresponded to the GGG phase in the expected epitaxial (100) crystalline orientation. The intensity of the diffraction from the GGG (400) lattice plane was higher for films deposited with higher energy pulses. The thicknesses of the films was measured to be in the range 30 - 40 nm (1.3 J/cm^2), 30 - 60 nm (3.9 J/cm^2), 100 - 120 nm (5.7 J/cm^2) and 110 - 150 nm (7.0 J/cm^2). Figure 5.11(f) shows a plot of the GGG (400) peak position (2θ) against laser fluence. The peak position was closer to that for stoichiometric GGG ($2\theta = 28.839$) for lower fluences.

A notable point is that the GGG phase is present even for lower fluences (1.3 J/cm^2) with a relatively small ablation spot-size of 57 by 80 µm (film 11), whereas film material deposited with a higher fluence (3.1 J/cm^2) and a larger spot-size of 90 by 135 µm (film 6) shows poor growth of the GGG phase. This demonstrates that the spot-size is a critical parameter for optimum growth.

Studies have shown that the influence of the spot-size plays an important role in the emission of nanoparticles and macroscopic droplets by femtosecond ablation. It has been shown by Perrière et al. (2007) that in the case of smaller spot-sizes the emission of macroscopic droplets is observed, while for larger spot-sizes the emission

of nanoparticles is more dominant. Also, the emission of nanoparticles is shown to decrease for higher fluences. A similar effect has been noticed by Jelinek et al. (2002). The role of spot-size is clearly having an influence on the crystallinity of the films we have deposited, evidenced by the difference in film quality of films 11 and 6. The reported reduction of nanoparticle emission for smaller spot-size may be leading to the differences we have observed here, since the presence of nanoparticles will inevitably have a negative influence on the crystalline quality of the deposited film. However, it also well-known that the ablation spot-size affects the distribution of the elemental species in the plasma plume (Kools et al. 1992), and this may have lead to the differences in film crystallinity.

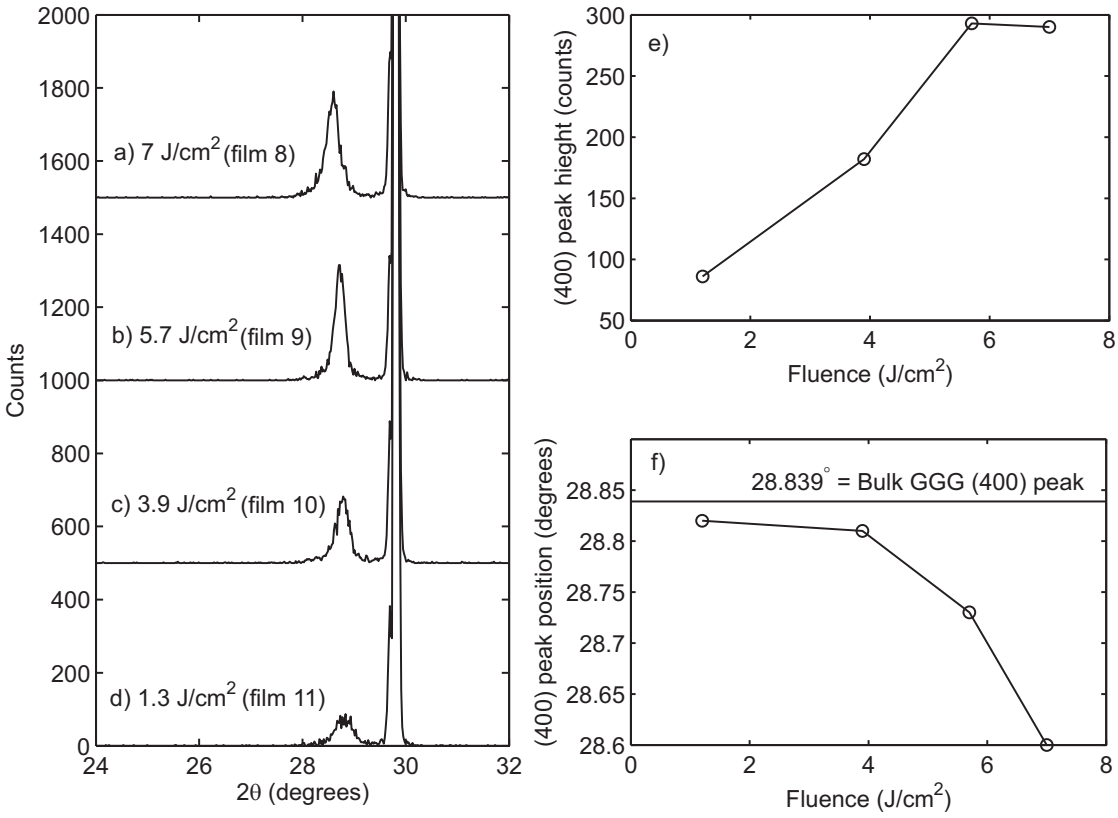

FIGURE 5.11: (a)-(d) XRD spectra of films deposited using various laser fluences with a constant spot-size of 57 by 80 µm (films 8-11). The spectra are offset on the counts axis for clarity. (e) Peak counts detected from the GGG (400) peak for various fluences. (f) 2θ position of the GGG (400) peak for various fluences.

5.3.1.4 Effect of changing temperature

Figure 5.12 shows the XRD spectra of films grown with various substrate temperatures (films 12-15). Incident CO_2 laser heating powers upon the substrate were varied from

8 W to 15.5 W, which corresponded to a temperature variation of approximately 750 ℃ to 970℃. Film thicknesses were measured to be in the range 60 - 100 nm (film 12), 80 - 90 nm (film 13), 80 - 100 nm (film 14) and 80 - 100 nm (film 15). XRD analysis revealed the optimum temperature for GGG growth is less than 900 ℃, and films deposited at a temperature of ≥900℃ showed multi-phase growth. At a temperature of 970℃ the garnet phase of GGG was no longer evident. Figure 5.13 shows SEM micrographs of films deposited at temperatures of 820℃, 900℃ and 970 ℃ (films 13-15).

Clearly visible on the surface of the films are structures, which are more irregular on films deposited at higher substrate temperatures. It is possible that these features are the result of particulates that are acting as growth nuclei. X-ray diffraction spectra of the film deposited at a temperature of 970℃ revealed another phase of material was present, although this could be not be identified with certainty.

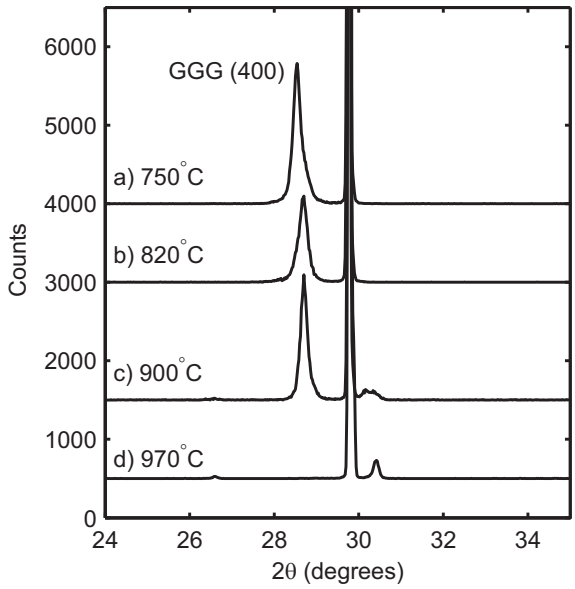

FIGURE 5.12: XRD spectra of films grown at various substrate temperatures of a) 750 °C (film 12) b) 820 °C (film 13) c) 900 °C (film 14) d) 970 °C (film 15), with laser fluence 12 J/cm^2. See table 5.2 for deposition conditions.

5.3.1.5 Effect of changing target-substrate distance

Noticeable improvements in the films' crystallinity were made by decreasing the target-substrate distance. Figure 5.14 shows XRD spectra of films deposited at target-substrate distances of 4.5 and 2.5 cm (films 16 and 17). The thicknesses were measured to be in the range 460 - 490 nm (target-substrate distance 2.5 cm) and 70 - 90 nm (target-substrate distance 4.5 cm). For a target substrate distance of 2.5 cm, the GGG (400) 2θ peak

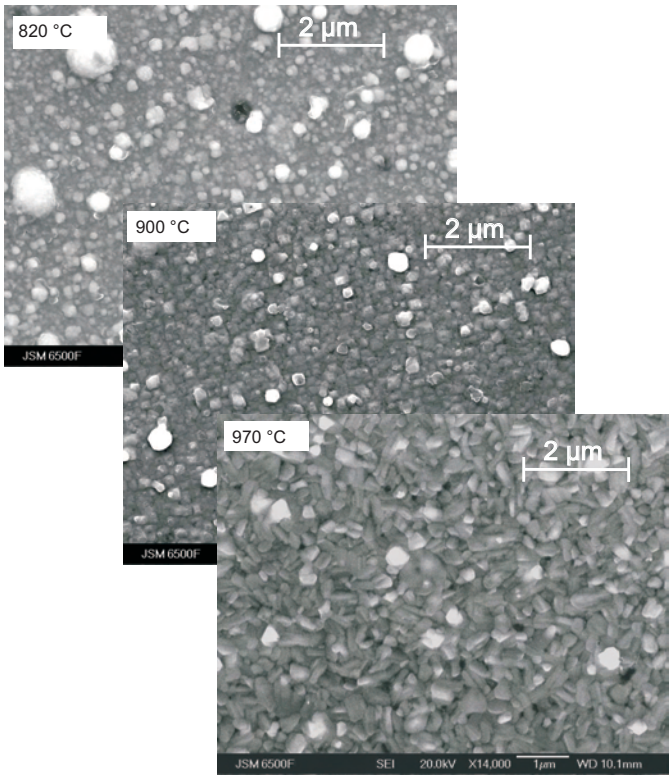

FIGURE 5.13: SEM micrographs of films deposited with a temperature of 820℃, 900℃ and 970℃ (films 13-15).

position is higher, with a lattice parameter that more closely matches stoichiometric GGG. This peak is also sharper, with a FWHM of 0.2° compared to 0.3° for a larger distance of 4.5 cm.

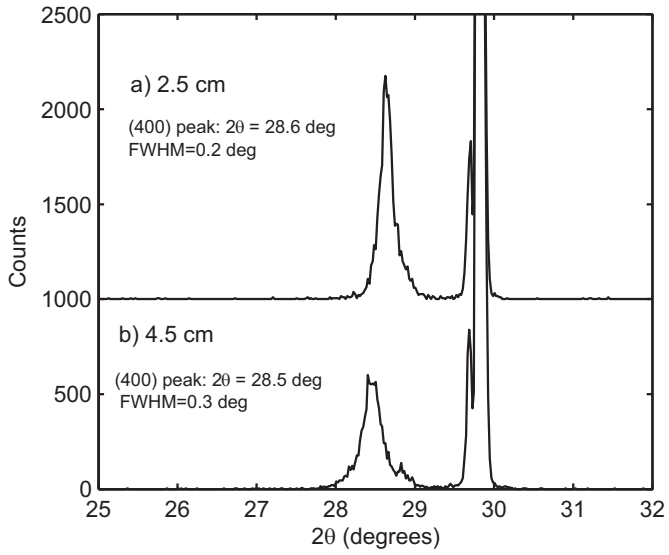

FIGURE 5.14: XRD spectra of films deposition with a target-substrate distance of 4.5 cm and 2.5 cm (films 16 and 17).

5.3.1.6 Effect of laser repetition rate and duty cycle

An investigation of the effect of the laser repetition rate and duty cycle using the growth conditions used for film 18 was undertaken. There have been reports that suggest improved growth can occur by depositing material for short intervals followed by a short time when no deposition occurs (Blank et al. 2000, Rijnders et al. 2000). Work conducted by Rijnders et al. (2000) has shown that it is possible to impose layer-by-layer growth of oxide materials in a growth regime where usually a multilevel growth mode is observed. In this case, improved growth of $SrTiO_3$ was demonstrated by manipulating the deposition intervals: depositing an amount of material that is sufficient to result in one unit cell of growth, followed by a short time when no deposition occurs. Films were deposited with laser duty cycles of 50/50, 200/200, 1000/1000 (Duty cycle: $x/y =$ x pulses on, y pulses off) at a repetition rate of 1 kHz. A film was also deposited at a frequency of 1 kHz for 1 minute and another film was deposited at 10 Hz for 100 minutes (note they were deposited using the same number of pulses). Figure 5.15 shows SEM micrographs of film deposited with various laser duty cycles (50/50 and 1000/1000) and laser repetition rates (1 kHz and 10 Hz). Reducing the repetition rate to 10 Hz did not result in any significant difference in the surface quality of the film. Changing the laser duty cycle to 50/50 or 1000/1000 also did not show any improvements in the films' surface quality.

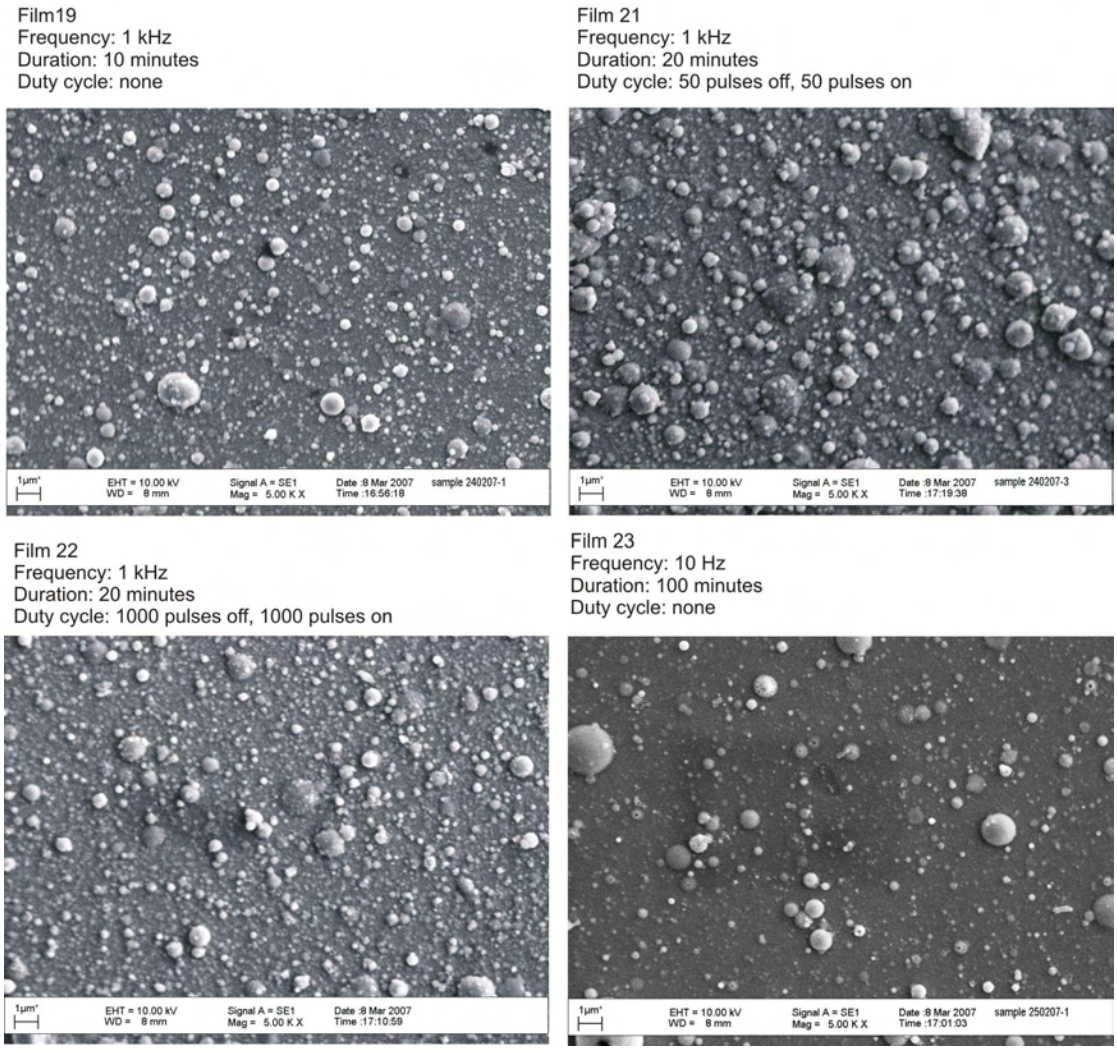

FIGURE 5.15: SEM micrographs of films deposited with various laser duty cycles and repetition rates (films 19, 21, 22, 23).

5.3.1.7 Longer duration depositions

Films were grown for successively longer durations to investigate whether the crystalline quality degrades progressively for thicker film material. In view of the surface quality of these films, it may be expected that particulate contamination will disrupt the growth of the epitaxial layers. Figure 5.16 shows XRD spectra of films deposited for durations of 10, 30 and 60 minutes using the same deposition conditions used to grow film 18. All films produced XRD spectra in the expected (100) crystalline orientation. Plotted in figure 5.16(d) is the GGG (400) peak position against the corresponding deposition time. The FWHM of the GGG (400) peak was not found to increase significantly for a longer deposition of 60 minutes compared to 10 minutes. The large degree of error in the estimate FWHM was due to the angle increment value of the diffractometer (0.05°). SEM analysis did not reveal any significant difference in the surface quality of the films, producing SEM micrographs that are not noticeably different to those presented in the preceding sections. The counts from the GGG (400) peak were higher for longer duration depositions. The thicknesses of the films were measured to be in the range 70 - 90 nm (10 minutes), 180-210 nm (30 minutes), 200 - 330 nm (60 minutes) and 310 - 750 nm (120 minutes), indicating a deposition rate of roughly 3-9 nm per minute. Note that

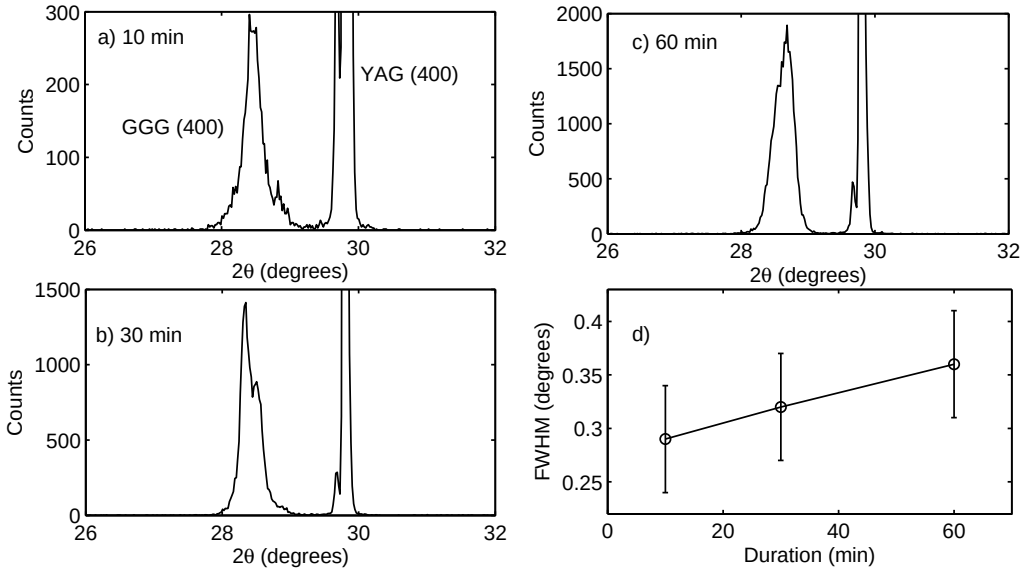

FIGURE 5.16: XRD spectra of films deposited for durations of a) 10 minutes, b) 30 minutes and c) 60 minutes, and d) a plot of the FWHM of the GGG (400) peak against the corresponding deposition time. The other deposition parameters were the same as those used for the growth of film 18.

film thickness measurements were taken at the edges of the films. The variation in film thickness was most likely caused by a slight misalignment of plasma plume with the centre of the substrate or a variation of the plume position (and hence plasma flux) during the deposition, both of which may result in an uneven deposition rate.

Figure 5.17 shows a wide θ-2θ (10 - 80 degrees) XRD spectrum of a film grown for 2 hours (310 - 750 nm thick) using the optimum deposition conditions. The GGG (400) peak is higher than its corresponding YAG peak and there are no other peaks from the $Gd_3Ga_5O_{12}$ phase, indicating that the film remains highly textured for thicker film material. This film's appearance was transparent with only a slight frosty trace. Further analysis of this film by XRD will be discussed in the next section.

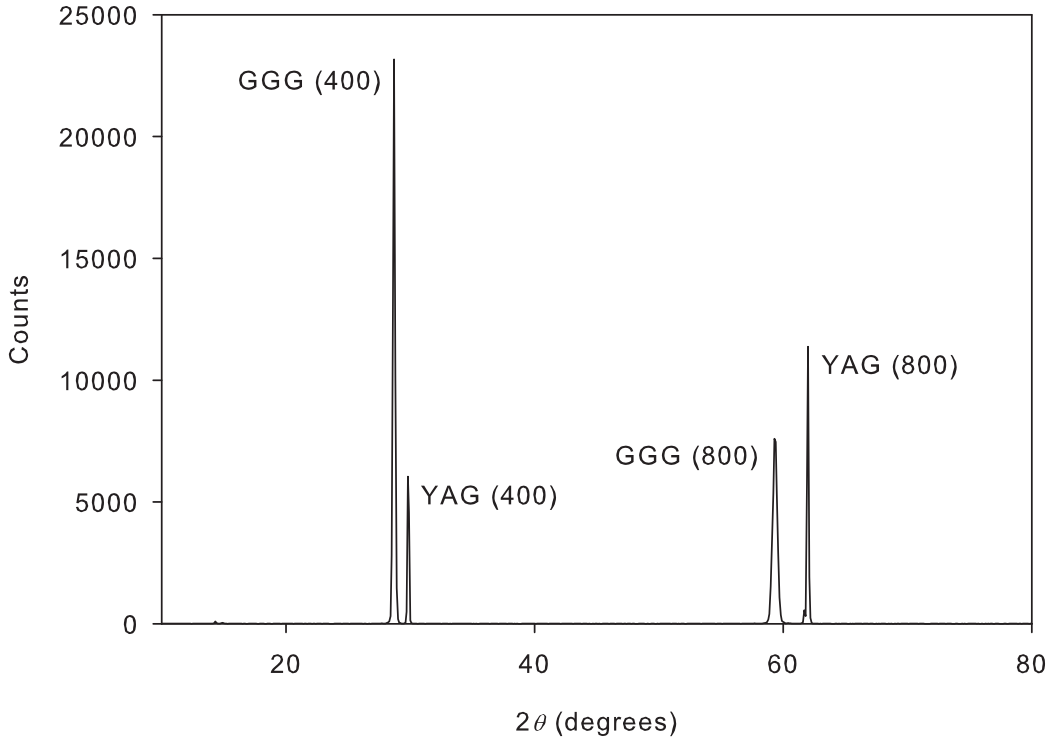

FIGURE 5.17: XRD spectrum of film 18.

5.3.2 Rocking curve analysis

More detailed analysis[2] of the film's crystal structure was demonstrated by a series of rocking curves that focused on the (400) GGG maximum and its associated YAG peak.

[2]The analysis presented here was performed by K. D. Rogers and co-workers (Cranfield University) and by M. Tremblay and J. F. Woitok (PANalytical, Netherlands)

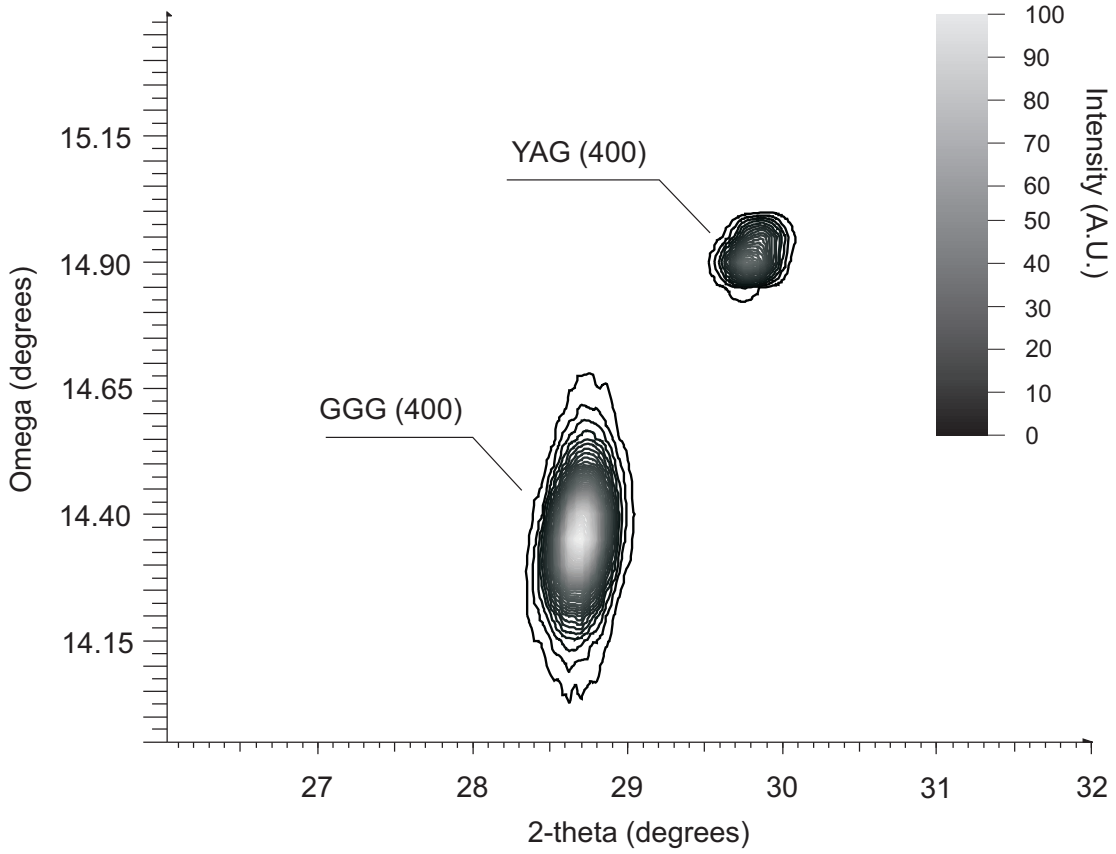

FIGURE 5.18: 2D rocking curve analysis of film 18 showing the GGG (400) and YAG (400) peaks.

Examination using the general area detector diffraction system (GADDS) produced strong evidence for the textured nature of the film examined. Film peaks were detected at 28.7° and 59.3° (±0.05°) which correspond to the (400) and (800) GGG crystalline planes respectively (Sawada 1997). Figure 5.18 shows a ω-2θ X-ray diffraction scan of a film grown for 2 hours (film 18). The 2θ data was measured at systematically increasing ω angles. The 2D diffraction patterns consisted of pairs of well-defined Bragg maxima that could be indexed to the YAG and GGG cubic lattices. Clearly shown in figure 5.18 is the diffraction peak from the GGG (400) plane consistent with epitaxial growth. The FWHM of the GGG (400) film peak in the ω axis is 0.17° ± 0.01°, and in the 2θ axis is 0.25° ± 0.01°. No evidence of polycrystalline films, which would produce diffraction maxima spread along loci of constant d-spacing was observed for any of the films examined (films 16 and 18). Scattering distributions did not change significantly and peak intensity varied by $< 10\%$ over a 3 mm range of the locations measured.

Figure 5.19 shows a 2D diffraction pattern in the ω and 2θ axis for film 4. This represents multiple ω-2θ scans at different ω offsets where the diffracted intensity is presented using a logarithmic colour scale. The intensity spread along the ω axis indicates that the film has a certain mosaicity and consists of multiple single crystal domains slightly tilted with respect to each other.

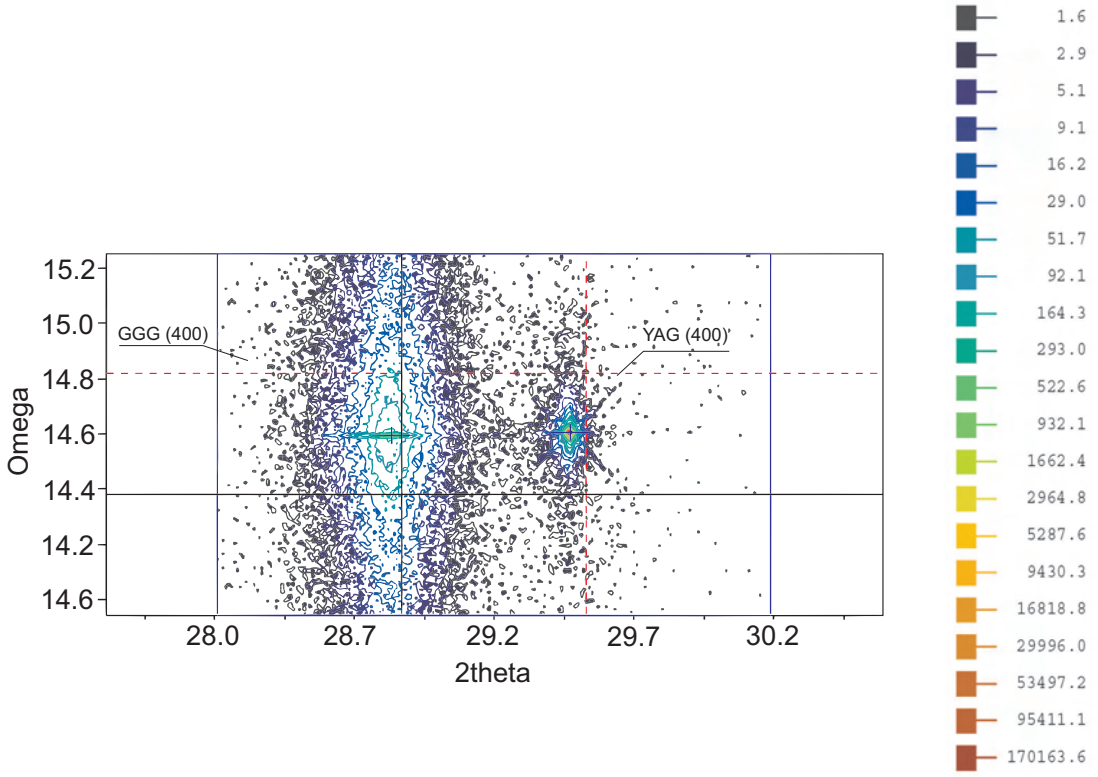

FIGURE 5.19: 2D rocking curve analysis of film 8 showing the GGG (400) and YAG (400) peaks. The 2θ data was measured at systematically increasing incident ω angles.

5.3.3 Surface morphology

All films deposited by femtosecond PLD showed a surface morphology that was not as smooth as nanosecond PLD. Figure 5.20 shows a comparison of AFM micrographs of Nd:GGG films grown by femtosecond and nanosecond PLD grown films. Figure 5.20(b) shows the random stacking of particulates of approximately 1 µm in diameter. Figure 5.21 shows an area of 20 µm by 20 µm examined by AFM for a film deposited by femtosecond PLD (film 16). From this micrograph we can see that the particulate-like features have a broad range of size distributions, some ranging up to roughly 2 µm for this film. However, most of the film appears to be covered in ∼micron-sized features. Further analysis using SEM was conducted on this film. Figures 5.22, 5.23 and 5.24 show

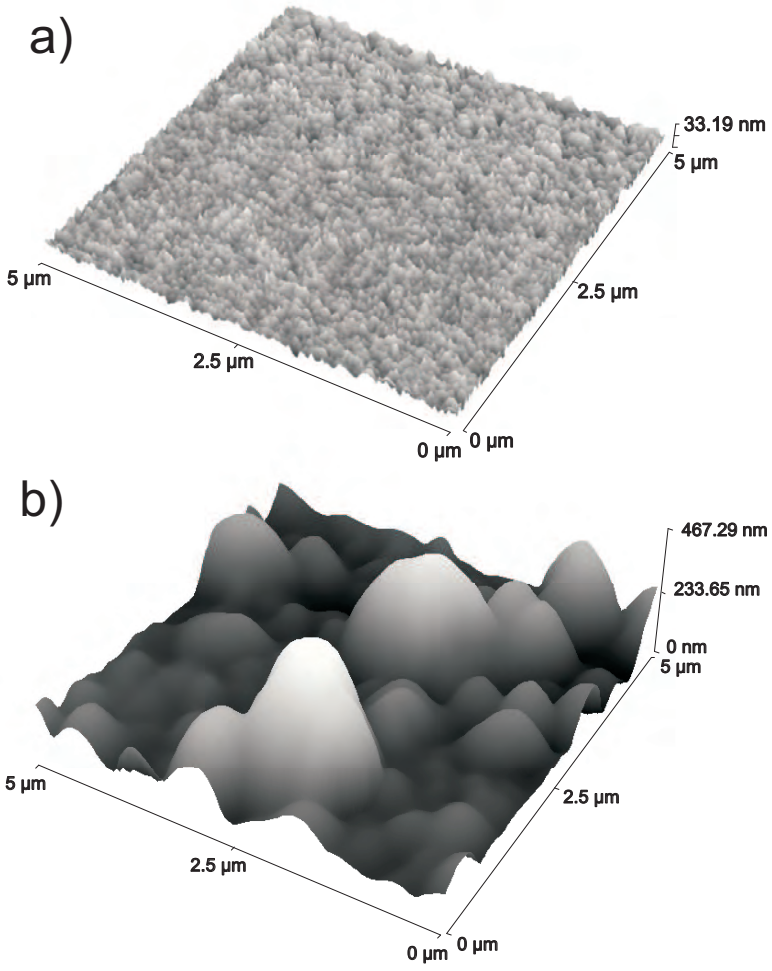

FIGURE 5.20: AFM micrographs of a film of Nd:GGG film deposited using a) nanosecond PLD (with the conditions: fluence 2 J/cm^2; spot-size 2 mm by 5 mm; energy per pulse 200 mJ; repetition rate 10 Hz; duration 40 minutes; target-substrate distance 4.5 cm; oxygen pressure 2×10^{-2} mbar and temperature 800℃) and b) femtosecond PLD (film 18).

SEM micrographs of a film 16 under a range of magnifications. This evidence clearly shows that the film consists of small (roughly 0.5µm to 2µm in diamter) particulates which have formed clusters.

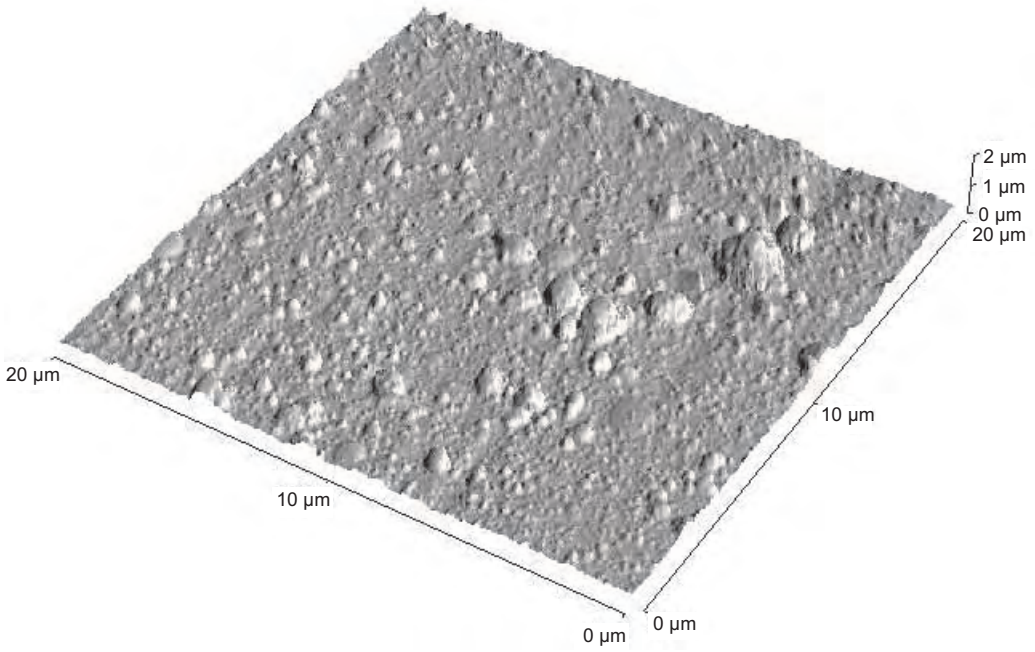

FIGURE 5.21: AFM micrograph of film 16.

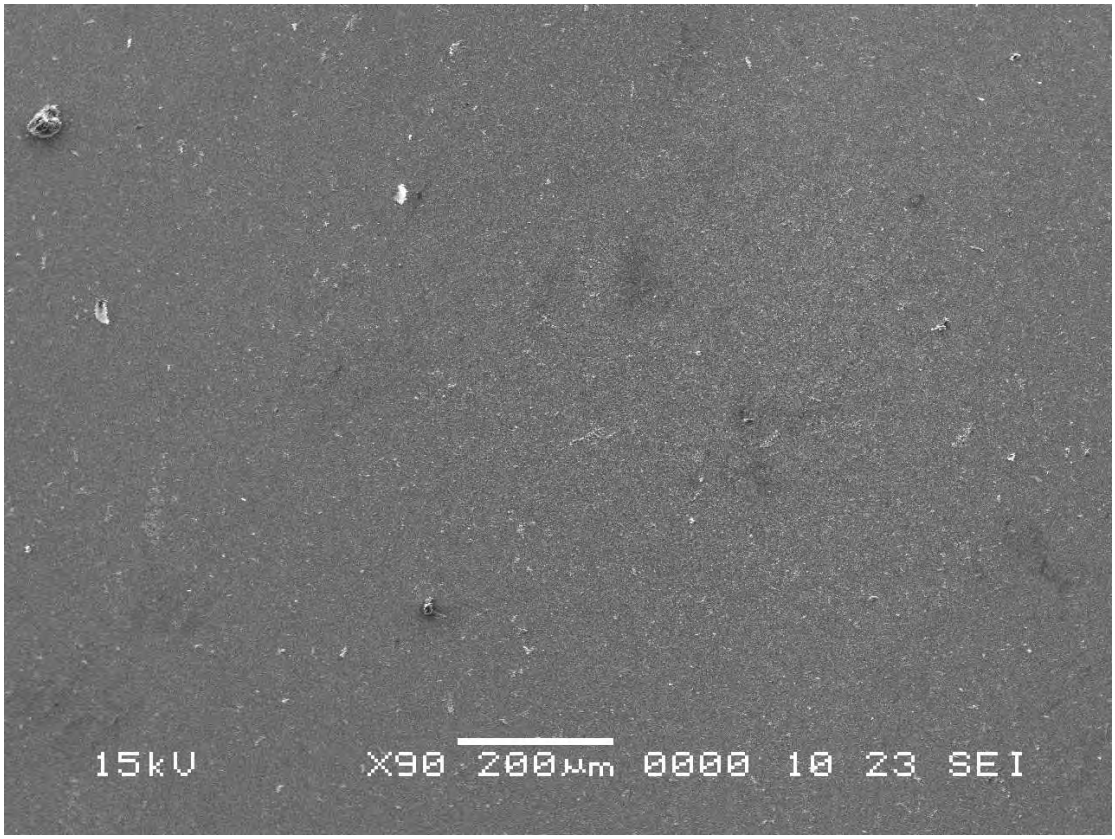

FIGURE 5.22: SEM micrograph of film 16.

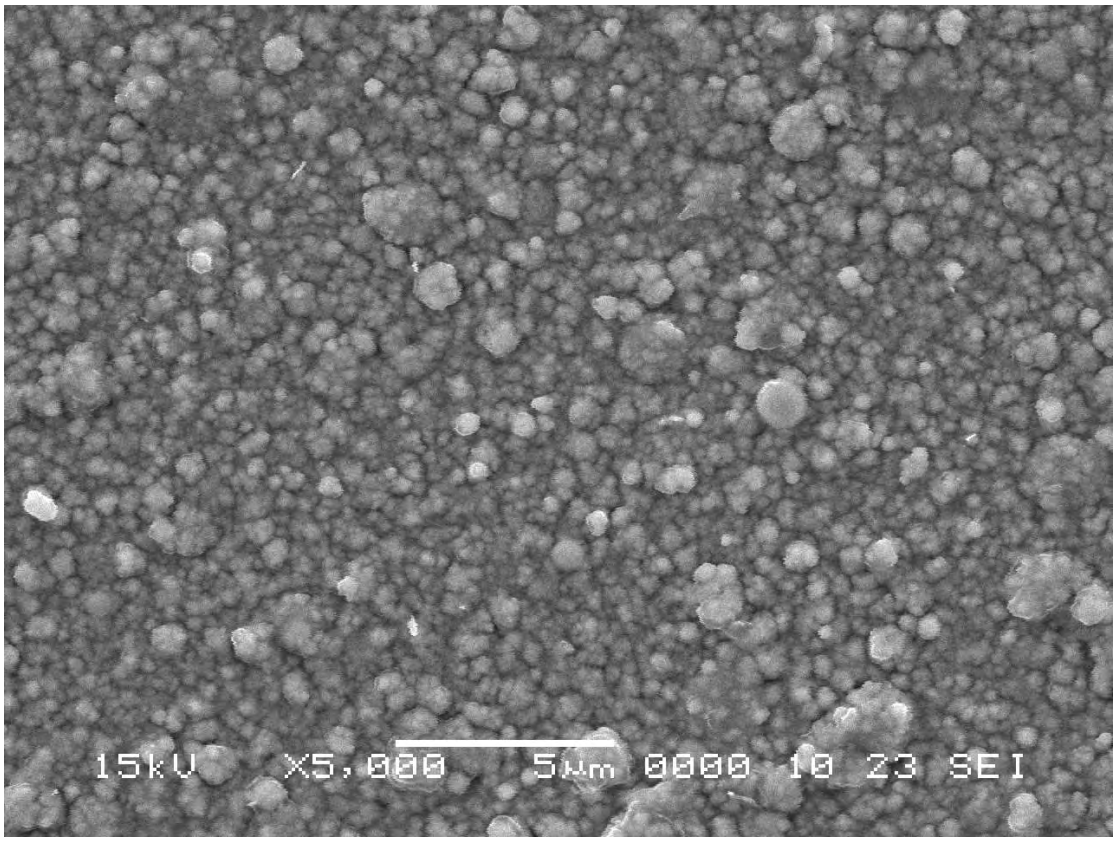

FIGURE 5.23: SEM micrograph of film 16.

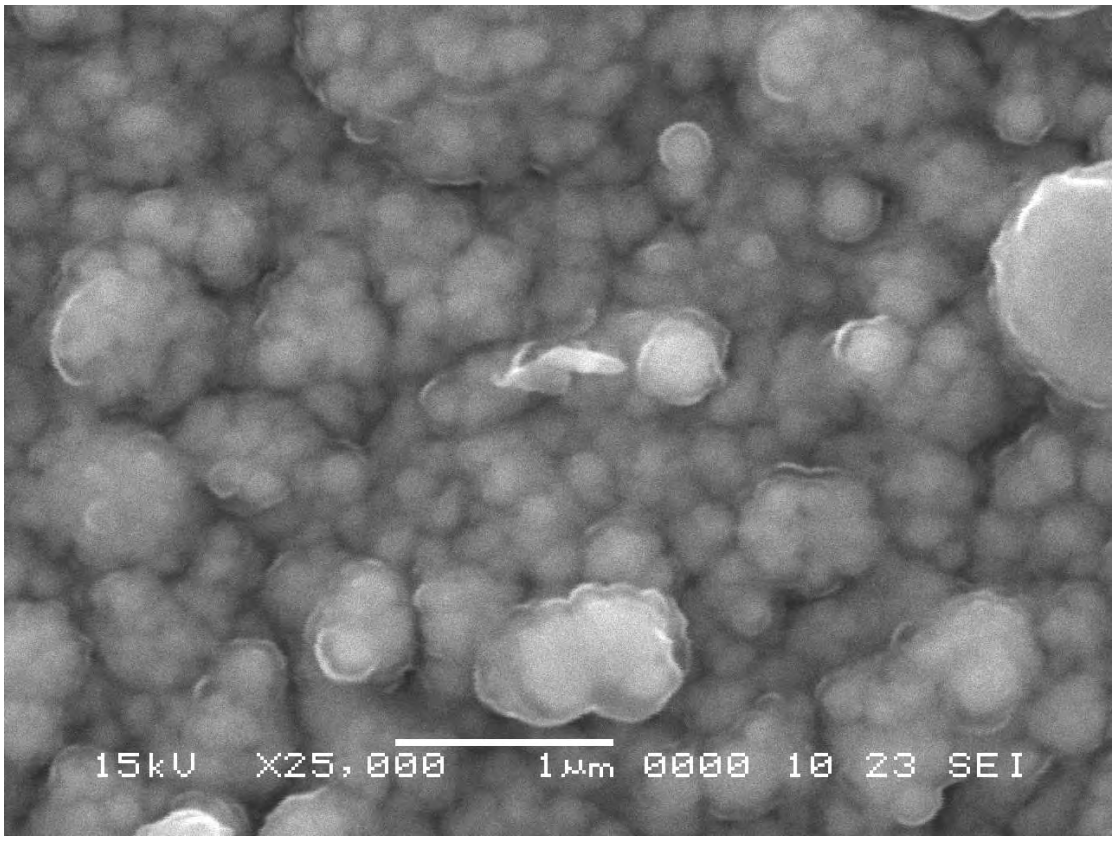

FIGURE 5.24: SEM micrograph of film 16.

5.3.4 Target surface

The target surface was examined to investigate the possible origins of the particulates observed on the films. Particulates can be produced from the surface of the target from protruding surface features, pits or cracks, which are progressively formed from ablation. These can be mechanically dislodged from laser-induced thermal or mechanical shock. Figure 5.25 shows an SEM micrograph of a Nd:GGG target that has been used for a 2 hour deposition. The surface of the target is shown to be relatively smooth and is covered with an arrangement of nm-wide cracks. A large area of roughly 1 cm by 1 cm of the target was examined at different locations, typically producing SEM micrographs that are not noticeably different to figure 5.25. From the SEM micrographs, there were very few fragments observable on the surface of the target and it is unlikely that these would have resulted in the high-density of particulates we have observed on the films.

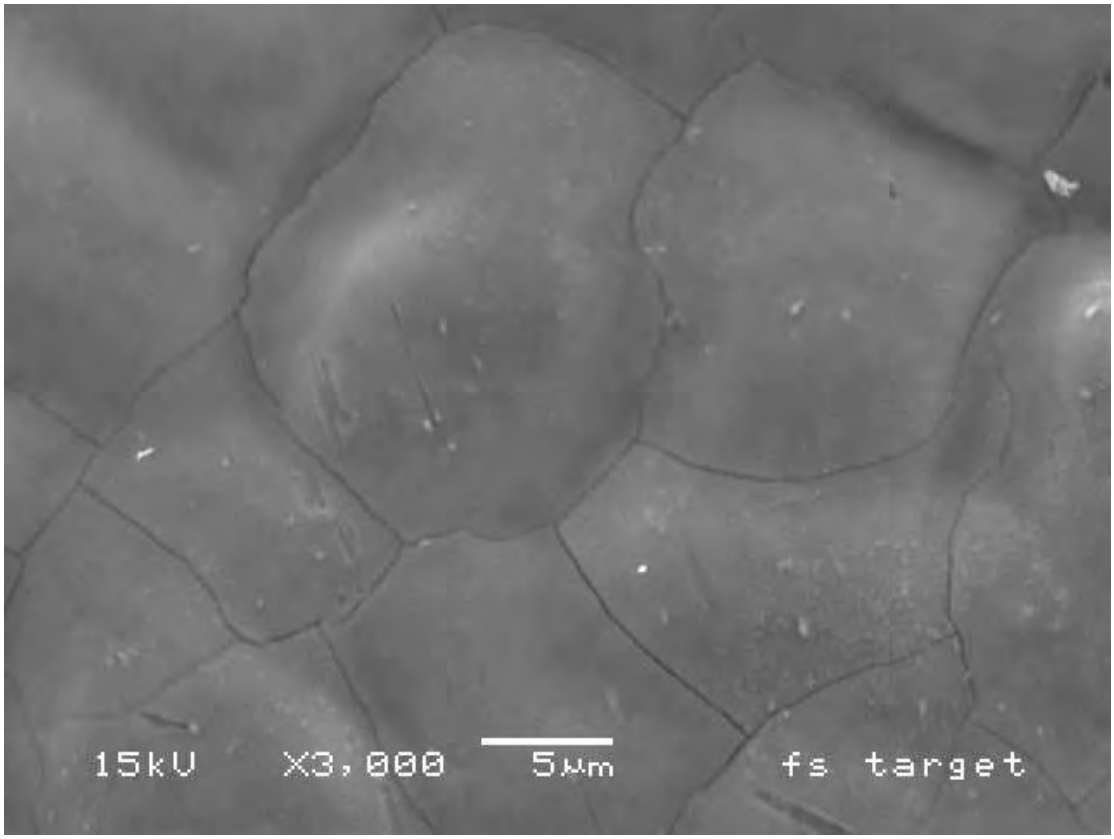

FIGURE 5.25: SEM micrograph of the surface of a Nd:GGG target used for a 2 hour deposition (used to deposit film 18).

5.3.5 EDX analysis of selected samples

EDX analysis was undertaken on a few selected samples (films 1 - 3, and 18) and the results are shown in table 5.3. The results show that film material deposited at lower pressures are increasingly deficient in gallium. Film material deposited under high pressures with high laser fluences (film 18) has a composition of gallium and gadolinium that is closer to stoichiometric GGG. The higher fluences or the closer distances used to deposit this film have affected the gallium and gadolinium concentration. XRD analysis of the corresponding films shows that shorter target-substrate distances and higher fluences results in a film with a GGG (400) peak that is narrower. Also, from the XRD diffraction spectra of films deposited at pressures of 10^{-2} mbar and 10^{-3} mbar (films 2 and 3) there is evidence of multiphase growth, which is predicted to be the gallium deficient phase $Gd_3(GaO_4)O_2$ and $Gd_3Ga_5O_{12}$. EDX analysis of these films confirms that they are gallium deficient.

Sample	Pressure (mbar)	Distance (cm)	Fluence (J/cm^2)	Composition
GGG target	-	-	-	Gd_3Ga_5
1	0.1	3.5	6.1	$Gd_{4.55}Ga_{3.45}$
2	0.01	3.5	6.1	$Gd_{4.76}Ga_{3.24}$
3	0.001	3.5	6.1	$Gd_{4.82}Ga_{3.18}$
18	0.1	2.5	19	$Gd_{3.24}Ga_{4.76}$

TABLE 5.3: List of composition measurements for selected films.

5.3.6 Optimisation of growth conditions: concluding remarks

The preceding sections have presented the experimental results used to optimise the conditions of the growth of Nd:GGG by femtosecond PLD. It is worth noting that the effect of each deposition parameter on the quality of the film material is not independent, that is to say, enhancement of film quality by varying one deposition parameter cannot be considered to be the absolute refinement of that parameter. More thorough improvements are made by an iterative process of optimisation. Therefore, although these experiments have investigated each parameter systematically, the PLD conditions presented as optimised cannot be considered the ultimate or best conditions. There may well be conditions of PLD growth that result in better film quality.

The notable effects of the deposition parameters on the film properties are listed below.

- A pressure of 0.1 mbar resulted in better growth of the GGG phase. Pressures of 0.01 mbar and below resulted in a dominant presence of the $Gd_3(GaO_4)O_2$ phase.
- Better growth of the GGG phase occurred at temperatures less than 900℃. Temperatures higher than 900℃ resulted in growth of other phases.
- Better crystallinity (i.e. lower FWHM of the GGG (400) peak) occurred at distances of 2.5 cm as compared to 4.5 cm. The lattice parameter of the GGG film is closer to stoichiometric GGG for closer distances of 2.5 cm.
- Film material remains highly textured even for a deposition duration of up to 2 hours (310 – 750 nm thick film).

The important point about the deposition conditions is that there is a narrower range of pressures in which the GGG phase can grow. The relatively high pressure of 0.1 mbar required is quite unlike that necessary for conventional nanosecond regime PLD for GGG. The GGG phase can be deposited under an oxygen pressure of 0.01 mbar using nanosecond lasers. Also, the surface quality of the films remains poor, revealing a high particulate density and does not appear to be significantly improved by changing the deposition parameters. The rough surface appears to be due to the emission of particulates, which become clearly evident from the SEM micrographs. The particulate contamination was not shown to significantly affect the quality of successively thicker film material, as might be expected, however, the longest duration deposition we have attempted is 2 hours, producing an epitaxial film of between 350 - 750 nm in thickness, and it may be the case that particulate contamination will have an effect on the quality of film material for film thickness greater than than those studies here.

5.3.7 Ion probe analysis: nanosecond and femtosecond regimes

Figure 5.26 shows time of flight (TOF) spectra for nanosecond and femtosecond laser produced plumes at various fluences and table 5.4 shows a list of the plasma plume properties for similar laser fluences (nanosecond: 1.45 J/cm^2 and femtosecond: 2 J/cm^2). The ablation spot-size and probe distance for femtosecond ion probe measurements were 90 µm by 130 µm and 5.5 cm, respectively. For the nanosecond ion probe measurements, the spot-size and the probe distance was 1.5 mm by 2.5 mm and 4.0 cm, respectively. The fluence was changed by attenuating the pulse energy and keeping the spot-size constant. Between each measurement the probe was cleaned with acetone to remove any deposit.

These measurements reveal some overwhelming differences between femtosecond and nanosecond regimes. Firstly, the peak TOF of the femtosecond ablated ions is over five times shorter than the nanosecond case, and the TOF of the femtosecond ablated ions is distinctively non-Maxwellian, indicating the possible non-thermal ablation mechanisms. The TOF spectra for the femtosecond case appears to have a dual-peak distribution

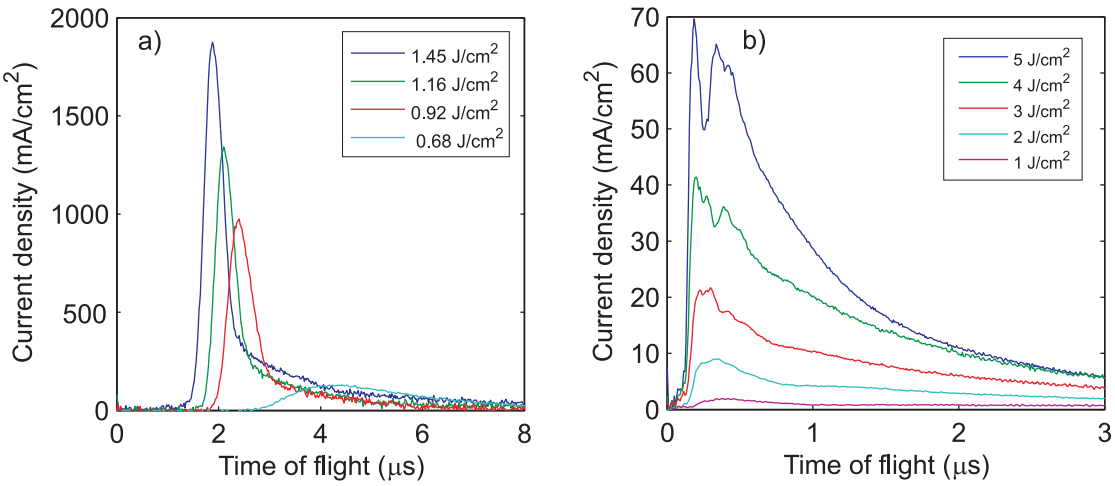

FIGURE 5.26: TOF spectra for a) nanosecond and b) femtosecond ablated ions in vacuum ($< 1 \times 10^{-4}$ mbar). The probe distance was 5.5 cm for the femtosecond measurements and 4.0 cm for the nanosecond measurements.

	Femtosecond (2 J/cm^2)	Nanosecond (1.45 J/cm^2)
Probe area (m^2)	1.25×10^{-5}	5×10^{-6}
Probe distance (cm)	5.5	4.0
Peak TOF (µs)	0.34	1.88
Peak velocity (m/s)	160,000	21,000
Most probable velocity (m/s)	29,000	21,000

TABLE 5.4: Comparison of plasma properties from femtosecond and nanosecond ablation at similar fluences.

at higher fluences of $5\,\mathrm{J/cm^2}$. The fast ion peaks could be due to the emission of highly energetic ions, possibly caused by non-thermal ablation mechanisms such as coulomb explosion. The double peaks in the signal may also be due to different ion components or even contamination of the target's surface. The use of an energy sensitive time of flight mass spectrometer could be used to identify which of these is the case. The peak velocity (velocity at the peak TOF) is over seven times faster than for the nanosecond case. The most probable velocity (velocity at the peak of the velocity distribution) however, is more comparable: $21,000\,\mathrm{m/s}$ for the femtosecond case and $15,000\,\mathrm{m/s}$ for the nanosecond case. This can be explained by the comparatively fewer higher velocity ions that have a more pronounced affect on the ion probe measurements, since the ion probe measures flux (in units of $\mathrm{mA/cm^2}$ for our case), and subsequently magnifies the higher velocity ion component.

Further analysis of the femtosecond ablated ions was conducted at lower fluences with a probe distance of 2.5 cm. Figure 5.27 shows TOF spectra for femtosecond ($0.82\,\mathrm{J/cm^2}$) and nanosecond ($0.92\,\mathrm{J/cm^2}$) ablated ions in vacuum ($< 1.6 \times 10^{-4}\,\mathrm{mbar}$). The probe distance was 4 cm for the nanosecond the measurements. The corresponding velocity distributions are also shown in figure 5.27. The results again reveal the high velocities of the femtosecond ablated ions and the double-peak velocity distribution. These results clearly show a higher velocity ion population travelling ahead of the majority of the plume at a velocity of $\sim 1.3 \times 10^5\,\mathrm{m/s}$ (peak TOF). The nanosecond ablated ions have a peak velocity of $1.6 \times 10^4\,\mathrm{m/s}$. The femtosecond ablated ions have a significantly broader range of velocities compared to the nanosecond ablated ions, with a range from 1.5×10^4 to $2 \times 10^5\,\mathrm{m/s}$. The nanosecond ablated ions have a much more narrow range (roughly 1×10^4 to $2 \times 10^4\,\mathrm{m/s}$).

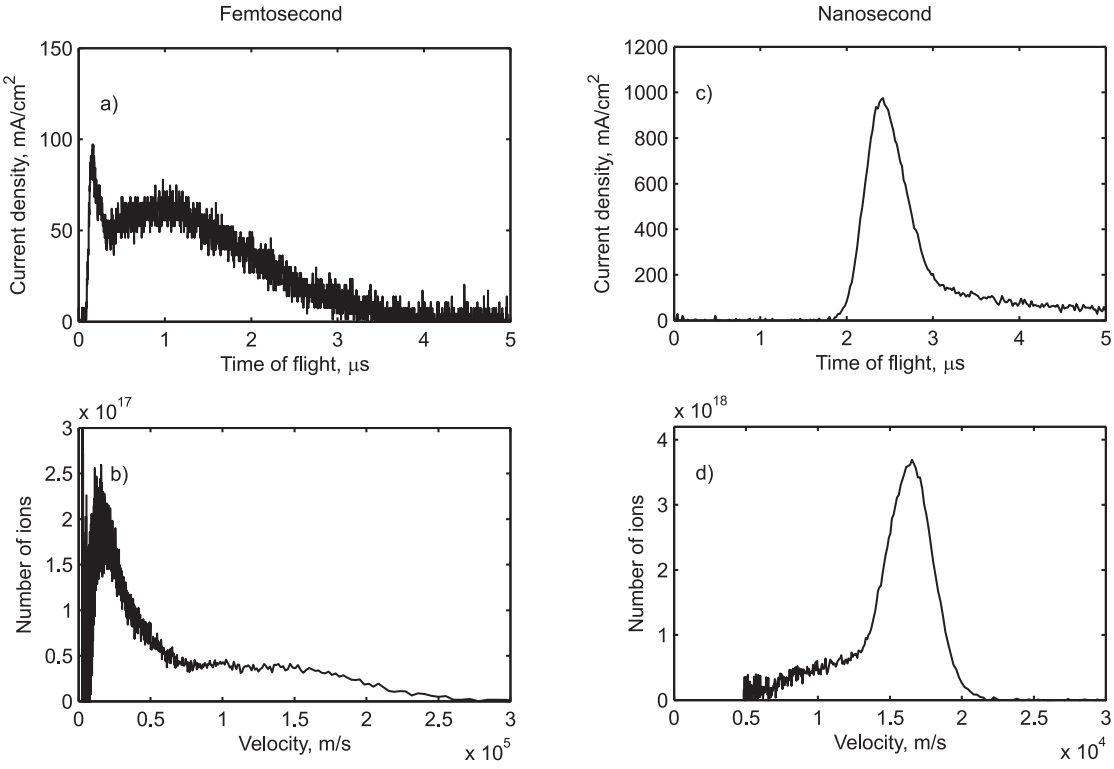

FIGURE 5.27: TOF spectra and corresponding velocity distributions of femtosecond (a and b) and nanosecond ablated ions (c and d) in a vacuum for similar laser fluences (femtosecond 0.82 J/cm^2, nanosecond 0.92 J/cm^2). The probe distance was 2.5 cm for measurement of femtosecond ablated ions and 4.0 cm for the measurement of nanosecond laser ablated ions.

5.3.7.1 Mass ablated per pulse

The mass removed from the GGG target was estimated by ablating a Nd:GGG target for 70 minutes and measuring the mass of the target before and after the laser exposure. The laser conditions were the same as those used for the growth of film 18 (see table 5.2) and the target was rotated during the exposure.

The total mass loss from 70 minutes of ablation at a laser repetition rate of 1 kHz was (33.0 ± 2.0) mg, corresponding to (7.9 ± 0.5) ng of mass ablated per pulse. The average ablation depth, assuming uniform removal of the target material occurs over an ablation spot-size of 45 by 35 µm, is therefore (225 ± 14) nm.

5.3.7.2 Ablation of silver

Ion probe measurements were also carried out on a silver target using a femtosecond laser. The ion probe distance from the target was 2.5 cm. Unlike the GGG target, the silver deposit on the surface of the conducting area of the ion probe did not degrade the signal quality and cleaning of the conducting area was not necessary. Some interesting differences can be observed from these measurements. Figure 5.28 shows TOF spectra and the corresponding velocity distributions of femtosecond ablated ions from silver and GGG targets for various fluences. The peak TOF of ions produced from femtosecond ablation of silver is significantly longer than that for ions produced from the ablation of GGG. The peak TOF is 1.3 µs compared to 0.18 µs for ions produced from GGG target (with a fluence of 5J/cm^2). The most probable ion velocity is $12,000$ m/s compared to $60,000$ m/s for ions produced from a GGG target.

5.4 Processes in PLD that can influence film topography

The features of the deposition process which may influence the topography of the films are a) fast ion emission (Albert et al. 2003), b) nano-particle production (Amoruso et al. 2004a), c) cluster-formation in the vapour phase (Lowndes et al. 1999), d) low mobility of adatoms resulting in island growth modes and e) the spatial distribution of the ablating pulse (Gamaly et al. 2004). The fast ions can have energies sufficient to cause sputtering, which may influence the growing surface. Energetic particles impacting on the surface of a growing film can influence the nucleation, energy and mobility of the adatoms on the surface of the film by colliding with atoms already adhered to

the existing islands, causing them to break their bonds or even become delocalised from the surface (sputtering). Energetic ions can have other deleterious effects on the growth of crystalline films, processes such as defect formation, sub-plantation, lattice damage. Recent studies examining the generation of nano-particles from femtosecond laser ablation has attributed the production of nanoparticles to a very high strain rate in the material during the ablation process, which can lead to fractures and the expulsion of fragments (Glover et al. 2003, Perez & Lewis 2002). Nano-particles produced in the ablation process can arrive intact at the growing surface and cluster together to from larger particulates. It is also possible that surface features can be caused by vapour condensation and the formation of clusters on the surface of the film.

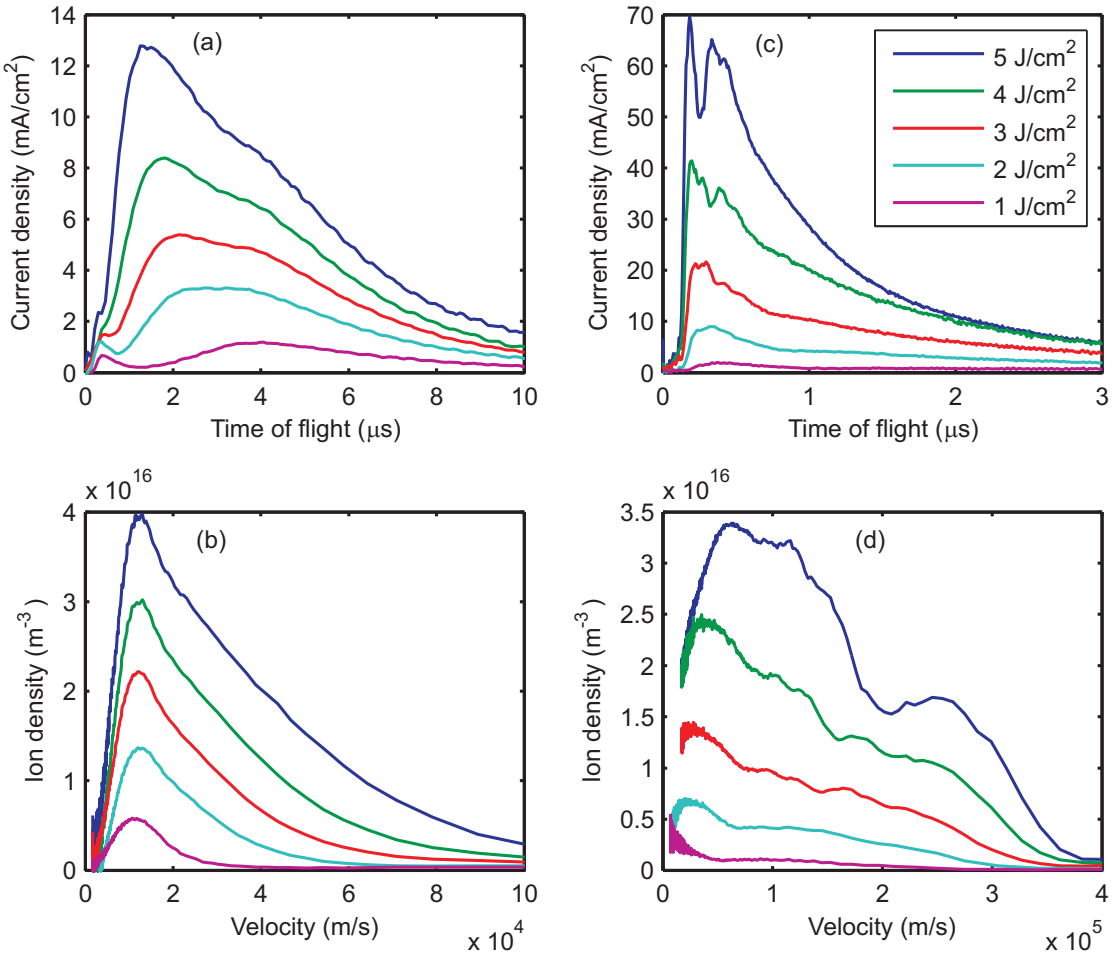

FIGURE 5.28: TOF spectra and corresponding velocity distributions of femtosecond ablated ions from a silver (a and b) and GGG target (c and d) in a vacuum ($< 1.6 \times 10^{-4}$ mbar).

5.5 Conclusions

This chapter has demonstrated highly textured growth of Nd:GGG on YAG substrates by femtosecond PLD and analysed the plume characteristics by the Langmuir probe technique for both nanosecond and femtosecond ablation. By systematic analysis via XRD of film grown under various deposition parameters, the conditions necessary for highly textured growth have been found. The velocities of the ions produced from femtosecond laser ablation were found to be up to eight times faster than those produced by nanosecond ablation for similar laser fluences. The topography of the films remains poor however, revealing a comparatively rough surface, which appears to have consisted almost entirely of particulates.

Chapter 6

Femtosecond and Nanosecond PLD of GLSO

This chapter will present experimental results on the deposition of gallium-lanthanum-oxysulphide glass (GLSO) using femtosecond and nanosecond regime lasers for a range of deposition conditions. The effect of the deposition parameters on the compositional properties of the films is investigated, and it is shown that femtosecond PLD is comparatively more non-stoichiometric as a method of film production than nanosecond PLD. Both nanosecond and femtosecond PLD can result in amorphous GLS film material with normalised percentages of gallium, lanthanum and sulphur that are outside the range of the reported region of glass-formation for this material. An investigation into the resultant compositional spread on the substrate shows that femtosecond PLD is comparatively richer in the heavier element lanthanum at greater off-axis distances. The femtosecond-laser deposited films are shown to consist almost entirely of particulates with an appearance that indicates that they have formed from either a molten phase or condensation of the vapour species. The nanosecond-laser deposited films are found to be very smooth, with comparatively few micron-sized particulates, most of which are presumed to have formed from fragments that have been dislodged from the target.

6.1 Introduction

6.1.1 Gallium-lanthanum-sulphide glass

Gallium-lanthanum-sulphide (GLS) glass was discovered over 30 years ago (Loireau-Lozac'h et al. 1976) and has provided an attractive non-toxic alternative to As- and

Ge-based chalcogenides. These glasses have many useful properties that make them attractive for optical or electronic devices. They are low-phonon-energy materials, are optically highly non-linear and are transparent from the visible up to the infrared. They are sensitive to the absorption of electromagnetic radiation, exhibit a variety of photo-induced effects (Zakery & Elliott 2003), and are a promising candidate for phase-change memory.

Bulk GLS glasses are produced by melting a mixture of gallium sulphide, lanthanum sulphide and lanthanum oxide with a typical molar composition of $70\,GaS_{1.4}$ – $24\,La_2S_3$ – $6\,La_2O_3$. For many of the applications of GLS glass it is desirable to fabricate it in thin film form. There are many methods that can be used to achieve this, for example hot spin coating, evaporation of material at low pressures and high temperatures in vacuum, sputtering, sol-gel methods and chemical vapour deposition. PLD has been used to deposit GLS films for more than a decade (Gill et al. 1995, Youden et al. 1993). The fast-quenching of each deposited layer, inherent in the PLD technique, induces the film to assume an amorphous phase that can potentially lead to new amorphous compositions far from the compositions attainable with conventional glass melting. PLD has the advantage over other techniques of being able to deposit a range of compositions on the same substrate by depositing material off-axis to the direction of the plasma-plume, which can be especially useful for investigating the effect of the composition on the properties of GLS films. This combinatorial chemistry approach to thin film fabrication provides a means of increasing the productivity of thin film analysis.

6.1.2 Phase-change memory

One application of GLS thin films is that of phase-change memory, in which information can be stored by inducing small regions of a thin film to switch between a crystalline and an amorphous state. Amorphous spots can be recorded by a pulsed laser beam that causes the temperature of the material to be locally higher than the melting point for a short period of time, and after the pulse, the molten region is quenched to the amorphous state. The amorphous spots can be erased by re-heating the material with the same focused laser beam above the crystallisation temperature but below the melting temperature. Due to the increased mobility of the atoms at increased temperature, the amorphous state returns to the thermodynamically more stable crystalline state. Phase-change optical recording has reached an industrial level, and the technology is applied

in the re-writable optical data storage devices, such as rewritable CDs (compact discs) and DVDs (digital versatile discs).

The phase-change of chalcogenide materials was first demonstrated in 1968 where it was shown that an Ar-ion laser with powers varying between 10 mW and 100 mW, focussed through an objective, could be used to reversibly change a material's phase (Ovshinsky 1968). The phase or state of the material can be read by measuring either the optical reflectivity or the electrical resistance, both of which exhibit different characteristics depending on the materials phase. GLS is a promising candidate because it has a high thermal stability compared with other chalcogenide glasses used in these devices. The electrical switching of thin films of GLS deposited by sputtering has been demonstrated (Simpson et al. 2007).

6.1.3 Glass-formation in the GLS system

The preparation of GLS glass by melting is limited in the range of compositions that are possible with selected precursor materials. This is known as the *glass-formation region*, and outside this region, a melt consisting of the incorrect compositions will form undesirable crystalline phases. The absence of crystals in a glassy matrix is a prerequisite for any optical application as the presence of crystals will increase the scattering losses of the medium.

The glass-formation region is influenced by many factors, such as the temperature of the melt, the quenching rate and the concentration of oxygen. Research into the compositions of GLS systems by Flahaut et al. (1983) mapped the full compositional range (figure 6.1). Table 6.1 shows the vitreous regions of GLS and GLSO systems fabricated with the highest quenching temperature, and hence the largest glass-formation region. These results show the compositions of GLS and GLSO that have been made without the presence of crystalline phases.

Early work by Loireau-Lozac'h et al. (1976) has shown that quenching a melt consisting of La_2S_3 and Ga_2S_3 from 1100℃ limits the glass-forming region to $m = 0.5$ –

System	Ga/(Ga + La)	Quenching temperature of (℃)
La_2S_3 – Ga_2S_3	0.50 – 0.85	1200
La_2O_2S – Ga_2S_3	0.60 – 0.80	1100
La_2O_3 – Ga_2S_3	0.70 – 0.85	1100

TABLE 6.1: Vitreous regions for various GLS and GLSO systems (after Flahaut et al. (1983)).

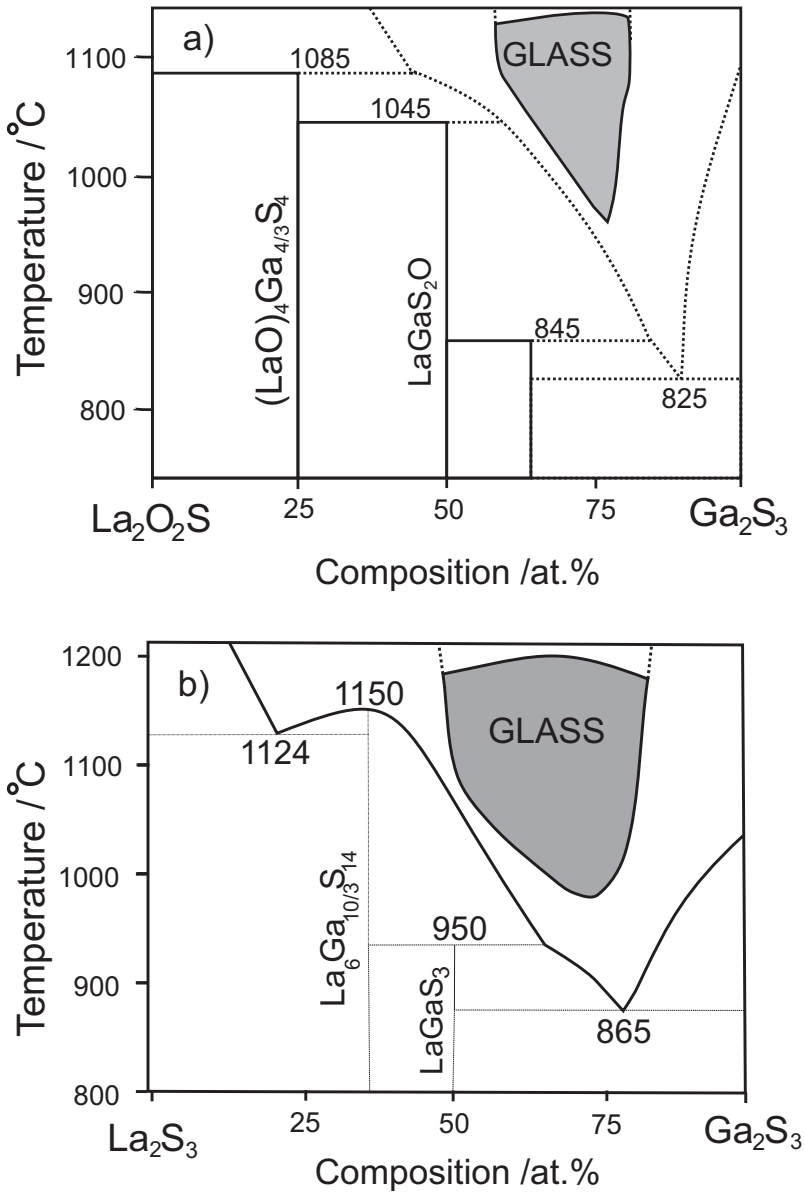

FIGURE 6.1: Phase diagram of a) the La_2O_2S – Ga_2S_3 system and b) the La_2S_3 – Ga_2S_3 system (after Flahaut et al. (1983)).

0.75, where m is the cationic fraction of Ga and is given by $m = \mathrm{Ga}/(\mathrm{Ga} + \mathrm{La})$, while quenching from 1200°C extends this region to m=0.5 – 0.85. and found the eutectic point for GLSO and GLS to be approximately 90 Ga_2S_3 – 10 La_2O_2S (at. %) and 79 Ga_2S_3 – 21 La_2S_3, respectively.

The oxygen content plays an important role in the formation of GLS glass. A threshold of 0.21 wt.% of elemental oxygen must be present to form crystal-free GLS via melting (Li et al. 1999). The inclusion of oxygen is shown to cause a shift of the visible absorption edge to shorter wavelengths and an increase of absorption intensity in the infrared (IR) region (Li et al. 1999). For the many applications of GLS that ultize the

low-phonon energy, such as a laser host in the IR region, this is a drawback, and therefore GLS glass is normally fabricated with the minimum amount of oxygen required to make it glassy.

6.1.4 Prior art

GLS thin films have previously been deposited by PLD using a KrF excimer (λ = 248 nm) laser and the films produced showed photo-stimulated changes (Gill et al. 1995). The refractive index from illumination with an argon ion laser produced a negative refractive index change of roughly 1%. An irreversible shift in the visible absorption edge to shorter wavelengths was also observed ($\sim$10 nm).

Arsenic-sulphide chalcogenide films have been deposited using a high repetition rate, 50 ps, 532 nm wavelength laser (Rode et al. 2002). The films were highly photo-sensitive and had a propagation loss of 0.2 dB/cm (at 1550 nm). The films were reported to have very smooth surfaces with no visible particulates, and stoichiometries that were very close to that of the target ($\pm$5 at. %).

To date, there has not been a study of the effect that the deposition parameters have on the compositions of the GLS or GLSO material deposited; the aim of previous reports has been to produce films with the same composition as the target and use its known properties in thin film form. However, the film composition plays an important role in the properties of the these films, and certain attractive features may well be enhanced with compositions outside the GLS glass-formation region. The study presented in this chapter contributes to this area of research by revealing the range of amorphous compositions that are possible in both laser regimes.

6.1.4.1 Other deposition methods

Many other methods have been used to deposit thin films of chalcogenide glass, which include:

- Hot spin-coating (Mairaj et al. 2004);
- Chemical vapour deposition (Huang & Hewak 2004);
- Sol-gel (Xu & Almeida 2000a);
- Sputtering (Frantz et al. 2006).

A relatively new method of producing thin films of GLS is that of *hot spin-coating*, which was first demonstrated for fluoride glasses (Harwood et al. 2003) and later for GLS (Mairaj et al. 2004). This differs from conventional spin-coating as it does not require the glass to be dissolved in a solvent solution (for example see Chern & Lauks 1982). In this process, a preheated substrate is dipped into a crucible containing molten glass, the substrate is then withdrawn and is spun at a high angular velocity to result in a thin viscous melt, which is subsequently quenched. Buried GLSO planar waveguides with a propagation loss of <0.2 dB/cm have been fabricated using this method (Mairaj et al. 2005).

RF magnetron sputtering has been used to deposit Er^{3+}-doped GLS glass waveguide amplifiers with a reported gain of 2.8 dB/cm at 1550 nm (Frantz et al. 2006).

Chemical vapour deposition (CVD) has been used to deposit high-purity chalcogenide glass (Ge:S) thin films using the reaction $GeCl_4+2H_2S_2 \longleftrightarrow GeS_2+4HCl$ (Huang & Hewak 2004). The impurity concentration in the resultant films was found to be much lower than those observed for chalcogenide glasses fabricated by melting. Also germanium sulfide planar waveguides have been prepared by sol-gel processing (Xu & Almeida 2000a) using germanium ethoxide as the precursor. The solution was spin-coated on to substrates and were sulphurised in an H_2S atmosphere and resultant films were found to have an optical loss of 3-4 dB/cm.

6.2 Experimental

The femtosecond PLD experiments were conducted in a vacuum chamber with an argon ambient gas pressure ranging between 2×10^{-4} mbar and 2×10^{-1} mbar. The set-up is described in a previous chapter (see section 5.2). The Ti:sapphire femtosecond laser was used to ablate GLSO targets with a fluence of 0.18 to 4.1 J/cm^2. The fluence was varied by adjusting the position of a focusing lens to alter the incident ablation spot-size.

The nanosecond PLD experiments were conducted in the same vacuum chamber using a flash-pumped frequency-quadrupled Nd:YAG laser ($\lambda = 266$ nm) with a repetition rate of 10 Hz. The fluence was varied by adjusting the output power of the ablating laser. All depositions, both in the nanosecond and femtosecond regimes, were conducted for a duration of five minutes and all films were deposited at room temperature. Various targets of GLS glass were used to deposit material on silicon, CaF_2 and quartz substrates.

Compositional measurements of each sample were taken at the centre of the film using a scanning electron microscope to which an energy dispersive X-ray analyser (EDX) was attached. The composition of the film was analysed over an area of 20 µm by 20 µm at evenly spaced points (a 4 by 4 array). An estimation of the error in EDX analysis was made by analysing twelve points in a 20×20 µm area of film and calculating the standard deviation. This provided an estimate for the measurement error of $\pm 0.5\%$. The error in the measured atomic percentage was less than 1%. Compositional data is presented in the form of normalised percentages of gallium, lanthanum and sulphur. For analysis of the compositional variation, measurements were taken over a range of distances along the surface of the film up to 20.5 mm away from the centre of the film, which corresponded to the location on the substrate where the centre of the plasma plume was incident. The central region of the films was analysed by SEM and the micrographs presented in this chapter are typical examples. XRD was used to investigate the crystallinity of the films. Film thicknesses were measure at the edge of the sample using a surface profiler.

The target materials were made using a high purity $GaS_1.4$ precursor material, which was synthesised by flowing H_2S gas over a gallium metal (9N purity) at 965℃ for 36h hours[1]. To synthesise the La_2S_3, LaF of 4N purity was heated to 1250℃ to remove water molecules from the crystal structure before sulphurisation in a flowing H_2S atmosphere at 1150℃. La_2O_3 was purchased from a commercial supplier. The precursor materials for a range of GLSO targets were then batched into vitreous carbon crucibles under a nitrogen atmosphere. The compositions of the GLSO targets used for the experiments reported here are shown in table 6.2. Each glassy target was formed by melting the load inside the crucibles at 1150℃ in a flowing argon atmosphere for 24 hours, followed by quenching in a water-cooled jacket. In order to remove any residual stress from the targets, the resultant glasses were then annealed for 6 hours at 550℃ before cutting and polishing to an optically flat surface.

Target	Measured composition (%)		
	Ga	La	S
A	33.1	11.4	55.5
B	33.1	11.4	55.5
C	32.6	11.5	55.9
D	19.7	20.3	60.0

TABLE 6.2: List of target compositions used for femtosecond and nanosecond PLD.

[1]Targets were fabricated by D. W. Hewak and co-workers (ORC).

6.3 Results and discussion

Table 6.3 shows the deposition conditions of films deposited by femtosecond and nanosecond PLD.

6.3.1 Comparison between femtosecond and nanosecond regimes

Figure 6.2 shows a ternary diagram of the measured compositions of films deposited by femtosecond and nanosecond PLD using targets with roughly the same compositions (targets A-C). Plotted on the same diagram is the conventional glass-formation region of GLSO material (from the La_2O_3 – La_2S_3 – Ga_2S_3 system reported by Flahaut et al. 1983). The films deposited by nanosecond PLD have been deposited with a range of deposition conditions of fluence, target-substrate distance and background pressure (films 1-10). The films deposited by femtosecond PLD have been deposited with various background pressures only (films 21 - 26). We can see from this diagram that the compositions of the films deposited by femtosecond PLD are richer in lanthanum. The higher pressure of 10^{-2} mbar compared to 10^{-4} mbar is shown to increase the lanthanum content by roughly 10%. None of the films (21-26) deposited by femtosecond PLD are within the conventional glass-formation region (Flahaut et al. 1983) for GLSO material. Films deposited by nanosecond PLD are shown to contain a roughly constant normalised gallium percentage and many of the films are close to the measured target composition. The films that are richer in lanthanum (and deficient in sulphur) have been deposited with relatively high background pressures of 10^{-2} and 10^{-1} mbar (films 6 and 7 respectively).

Figure 6.3 shows the measured composition of films deposited by nanosecond PLD for various deposition parameters of fluence, target-substrate distance and pressure using the same target (target A). The effect of fluence between the values we have used (0.6 - 2.4 J/cm^2) does not influence the film's normalised gallium, lanthanum or sulphur percentages by a significant amount (variation of $< 2\%$). Increasing the target-substrate distance was found to decrease the normalised sulphur percentage while increasing the gallium and lanthanum percentage. Increasing argon background gas pressure was found to reduce the sulphur and increase the gallium and lanthanum concentrations.

Figure 6.4 shows the measured composition of films deposited by femtosecond PLD for various deposition conditions of fluence, target-substrate distance and pressure using the same target (target D). Varying the deposition parameters for femtosecond PLD

Sample	Regime	Target	Energy per pulse (mJ)	Ablation spot-size	Fluence (J/cm^2)	Pressure (mbar)	Distance (cm)	Thickness (nm)
Varying laser fluence (constant spot-size)								
1	ns	A	72	0.75 mm by 1.25 mm	**2.4**	2×10^{-4}	4	770
2	ns	A	54	0.75 mm by 1.25 mm	**1.8**	2×10^{-4}	4	830
3	ns	A	36	0.75 mm by 1.25 mm	**1.2**	2×10^{-4}	4	520
4	ns	A	18	0.75 mm by 1.25 mm	**0.6**	2×10^{-4}	4	370
Varying argon background gas pressure								
5	ns	A	54	0.75 mm by 1.25 mm	1.8	$\mathbf{1 \times 10^{-3}}$	4	550
6	ns	A	54	0.75 mm by 1.25 mm	1.8	$\mathbf{1 \times 10^{-2}}$	4	360
7	ns	A	54	0.75 mm by 1.25 mm	1.8	$\mathbf{1 \times 10^{-1}}$	4	400
Varying target-substrate distance								
8	ns	A	54	0.75 mm by 1.25 mm	1.8	4×10^{-4}	**6**	210
9	ns	A	54	0.75 mm by 1.25 mm	1.8	4×10^{-4}	**3**	810
10	ns	A	54	0.75 mm by 1.25 mm	1.8	4×10^{-4}	**2**	1500
Varying fluence (constant energy per pulse)								
11	fs	D	1.1	78 µm by 110 µm	**4.1**	5×10^{-4}	3	530
12	fs	D	1.1	127 µm by 180 µm	**1.5**	5×10^{-4}	3	2110
13	fs	D	1.1	315 µm by 455 µm	**0.25**	5×10^{-4}	3	1180
14	fs	D	1.1	370 µm by 520 µm	**0.18**	5×10^{-4}	3	650
Varying Argon background gas pressure								
15	fs	D	1.1	127 µm by 180 µm	1.5	$\mathbf{5 \times 10^{-2}}$	3	2040
16	fs	D	1.1	127 µm by 180 µm	1.5	$\mathbf{5 \times 10^{-3}}$	3	2010
17	fs	D	1.1	127 µm by 180 µm	1.5	$\mathbf{1 \times 10^{-3}}$	3	2230
Varying target-substrate distance								
18	fs	D	1.1	127 µm by 180 µm	1.5	5×10^{-4}	**6**	450
19	fs	D	1.1	127 µm by 180 µm	1.5	5×10^{-4}	**4.5**	700
20	fs	D	1.1	127 µm by 180 µm	1.5	5×10^{-4}	**2**	2560
Samples deposited using different target compositions								
21	fs	A	1.1	127 µm by 180 µm	1.5	5×10^{-4}	4.5	632
22	fs	B	1.1	127 µm by 180 µm	1.5	5×10^{-4}	4.5	632
23	fs	C	1.1	127 µm by 180 µm	1.5	5×10^{-4}	4.5	616
24	fs	A	1.1	127 µm by 180 µm	1.5	5×10^{-2}	4.5	340
25	fs	B	1.1	127 µm by 180 µm	1.5	5×10^{-2}	4.5	370
26	fs	C	1.1	127 µm by 180 µm	1.5	5×10^{-2}	4.5	360
27	fs	A	1.1	110 µm by 156 µm	2.0	2×10^{-4}	2.5	2300

TABLE 6.3: Deposition conditions of GLSO films deposited by femtosecond and nanosecond PLD.

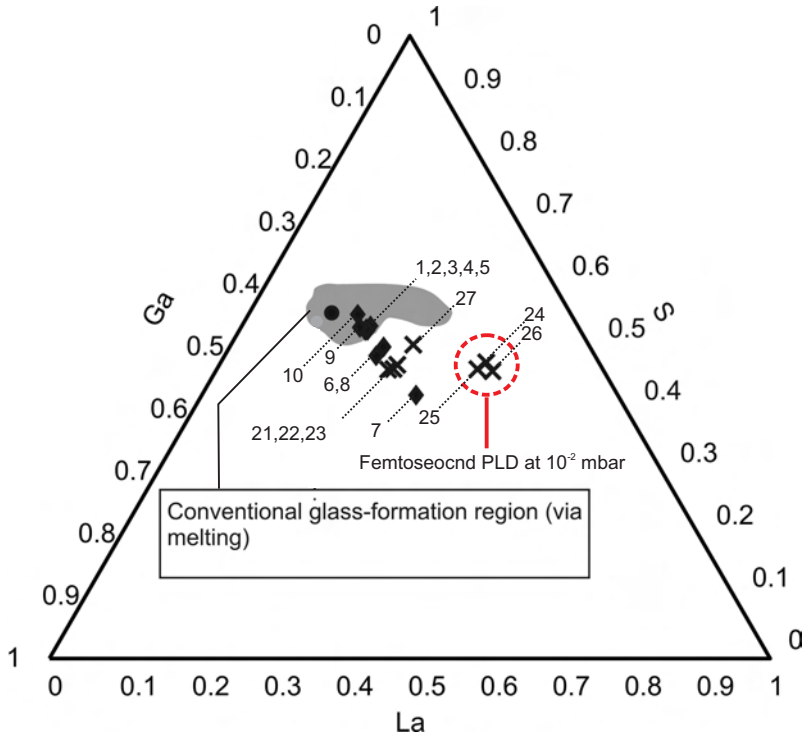

FIGURE 6.2: Ternary diagram of the measured film compositions deposited by femtosecond PLD (crosses: films 21-27) and nanosecond PLD (diamonds: films 1-10) using targets with roughly the same composition (targets A-C). The measured composition of target A is plotted on the diagram (circle). The numbers on the ternary diagram correspond to the sample number for the data-point (see table 6.3 for the deposition conditions).

was found to have a more pronounced effect on the composition of the films. Increasing fluence between 0.18 and 4.1 J/cm^2 was found to decrease the sulphur and increase the gallium and lanthanum concentrations by roughly 10%. Increasing the target-substrate distance had the effect of decreasing the sulphur concentration and increasing the gallium concentration. The lanthanum concentration was found to be higher when the target-substrate distance was increased from 2 cm to 3, cm and lower for distances greater than 3 cm. Films deposited at relatively low background gas pressures ($< 10^{-3}$ mbar) were found to be richer in gallium and contained less sulphur and lanthanum. At higher pressures the films were considerably richer in lanthanum and more defficient in sulphur.

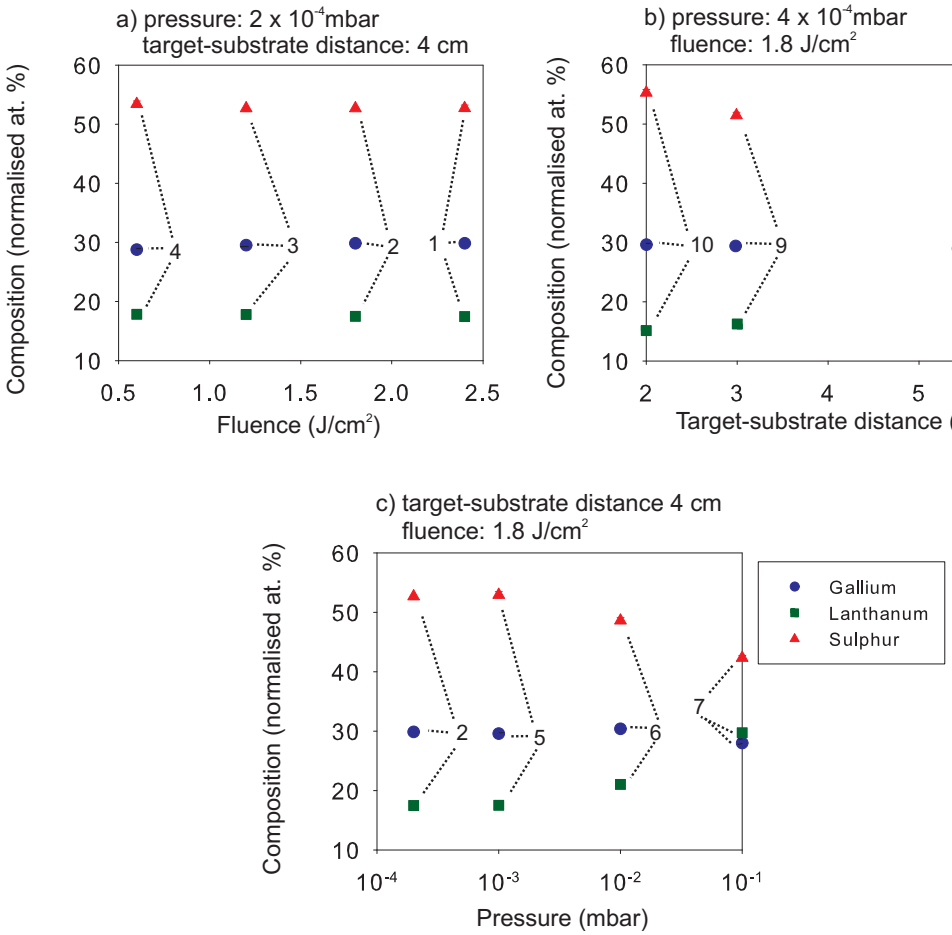

FIGURE 6.3: Effect of the deposition parameters on the normalised composition of gallium, lanthanum and sulphur for films deposited by nanosecond PLD: a) various fluences (films 1-4), b) various target-substrate distances (films 8-10) and c) various pressures (films 2, 5-7). The numbers on the graphs correspond to the sample number for the data-point (see table 6.3 for the deposition conditions).

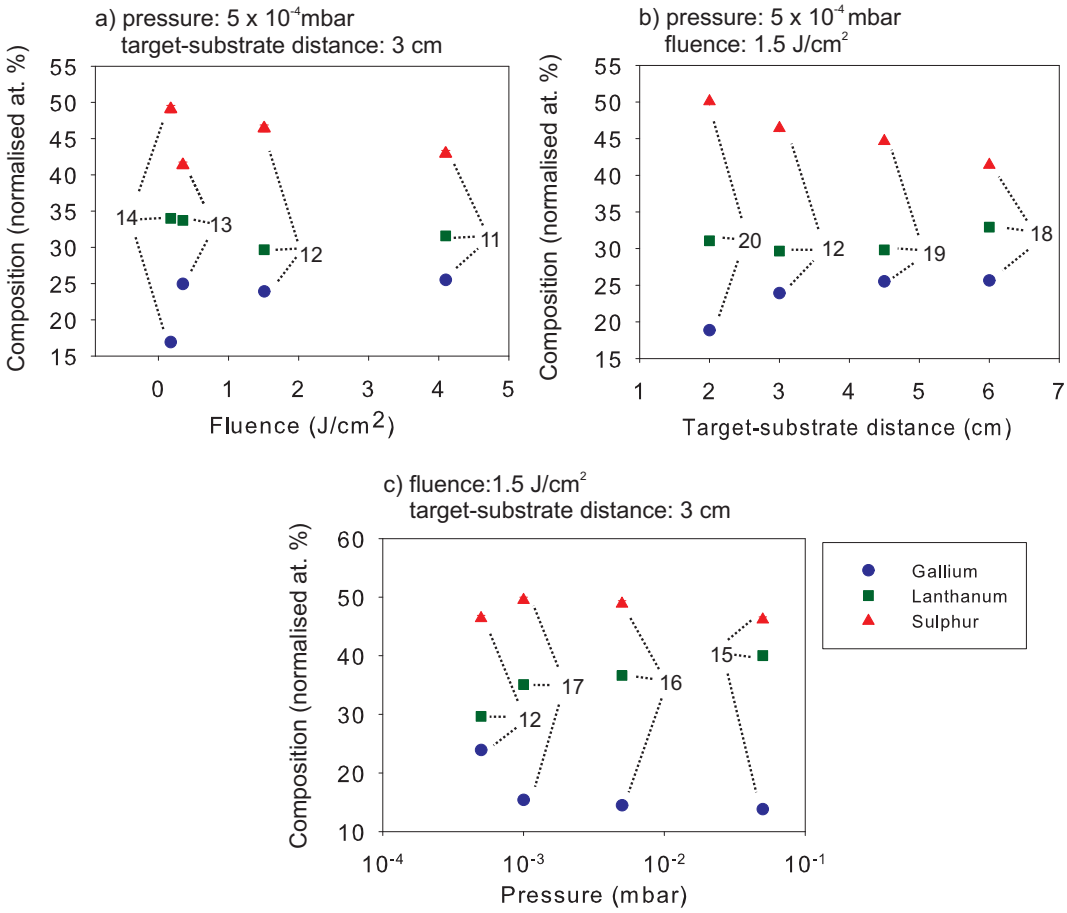

FIGURE 6.4: Effect of deposition parameters on the normalised composition of gallium lanthanum and sulphur of films deposited by femtosecond PLD: a) various fluences (films 11-14) b) various target-substrate distances (films 12, 18-20) c) various pressures (films 12, 15-17). The numbers on the graphs correspond to the sample number for the data-point (see table 6.3 for the deposition conditions).

6.3.2 Compositional spread

Figure 6.5 shows the compositional spread of films deposited by femtosecond (film 27) and nanosecond pulses (film 9) using a similar laser fluences (2.0 and 1.8 J/cm^2), pressures (2×10^{-4} and 4×10^{-4} mbar) and target-substrate distances (2.5 and 3 cm). Measurements were taken along a distance from the centre of the film, corresponding to the position of the centre of the plasma-plume incident on the substrate. A notable observation is the change in the atomic percentage of lanthanum for material deposited at higher off-axis geometries. For femtosecond PLD, the film's gallium content decreases and the film becomes considerably richer in lanthanum at distances farther away from the centre of the film. For nanosecond PLD, the sulphur percentage is reduced to a greater extent for higher off-axis geometries, and there is an increase in the gallium and lanthanum percentages. Figure 6.6 shows the compositional spread from a film deposited by femtosecond PLD (film 27) plotted on a ternary diagram. Compositional measurements were taken at distances up to 20.5 cm from the centre of the film. The results show a gradual increase in the lanthanum percentage for film material deposited farther from the centre of the plume.

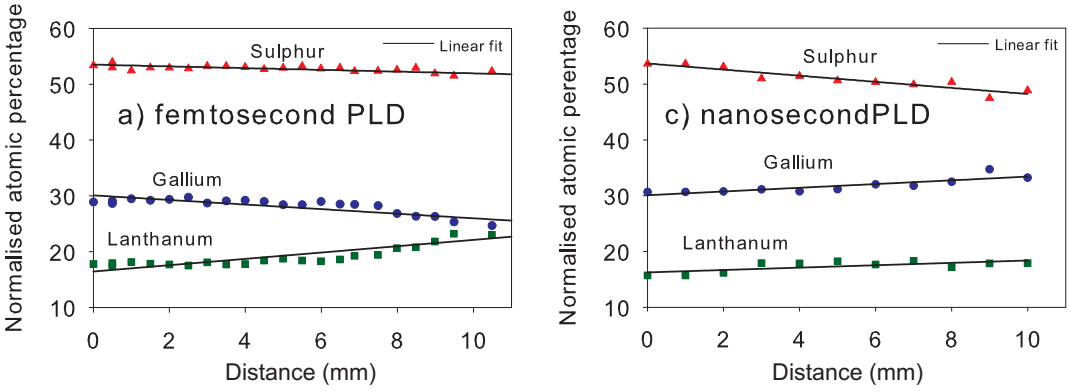

FIGURE 6.5: Compositional spread across a a film deposited by a) femtosecond PLD (film 27) b) nanosecond PLD (film 9) using target A.

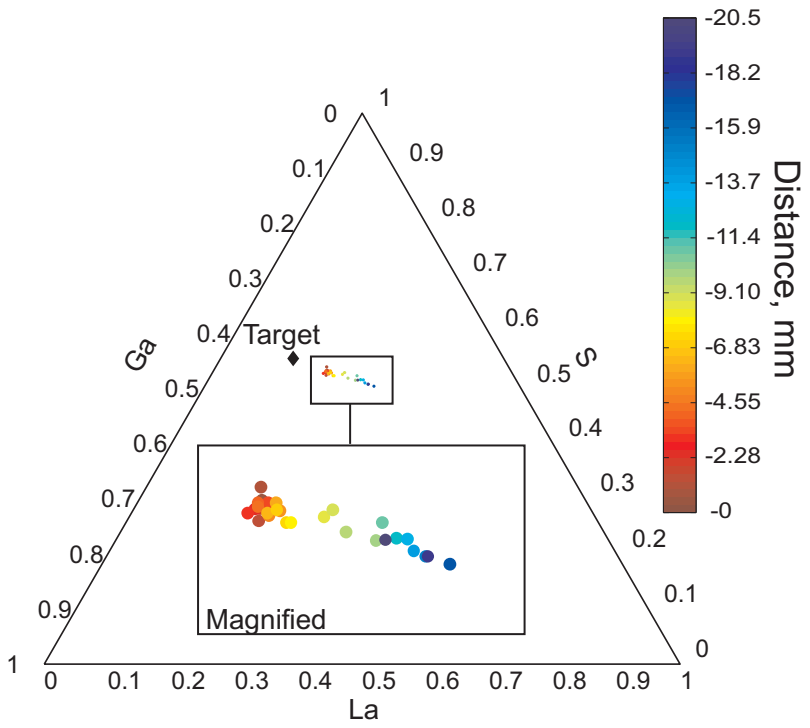

FIGURE 6.6: Ternary diagram of the compositional spread across a film deposited by femtosecond PLD (film 27).

6.3.3 Surface morphology

The surfaces of the films deposited by femtosecond PLD were all covered in particulates that were up to roughly 1 µm in diameter. The circular shape of the particulates suggests that they have formed from a molten phase during the ablation process or have formed from condensation of the vapour species. A lower fluence and larger ablation spot-size was found to result in more particulates that were smaller in diameter, evidenced by the comparatively high density of smaller particulates observed on a film deposited with the lowest laser fluence (figure 6.7). Figure 6.8 shows a higher magnification SEM micrograph of the surface of a film deposited by femtosecond PLD.

The films deposited by nanosecond PLD had very few particulates by comparision (figure 6.9). Even under high magnification (×10,000) of regions between the particulates, the film appeared very smooth with no discernible surface features.

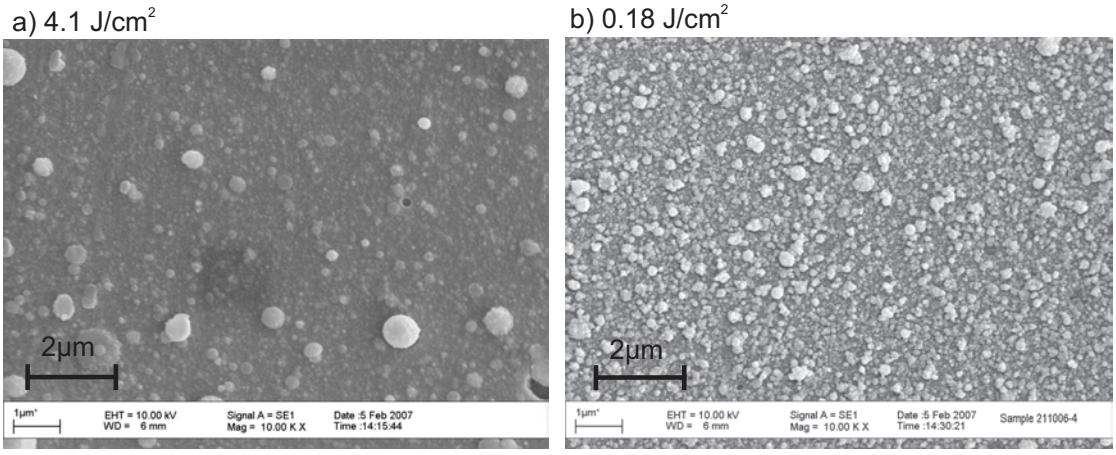

FIGURE 6.7: SEM micrographs of films deposited by femtosecond PLD with various fluences of a) 4.1 J/cm^2, b) 0.18 J/cm^2 (films 11 and 14).

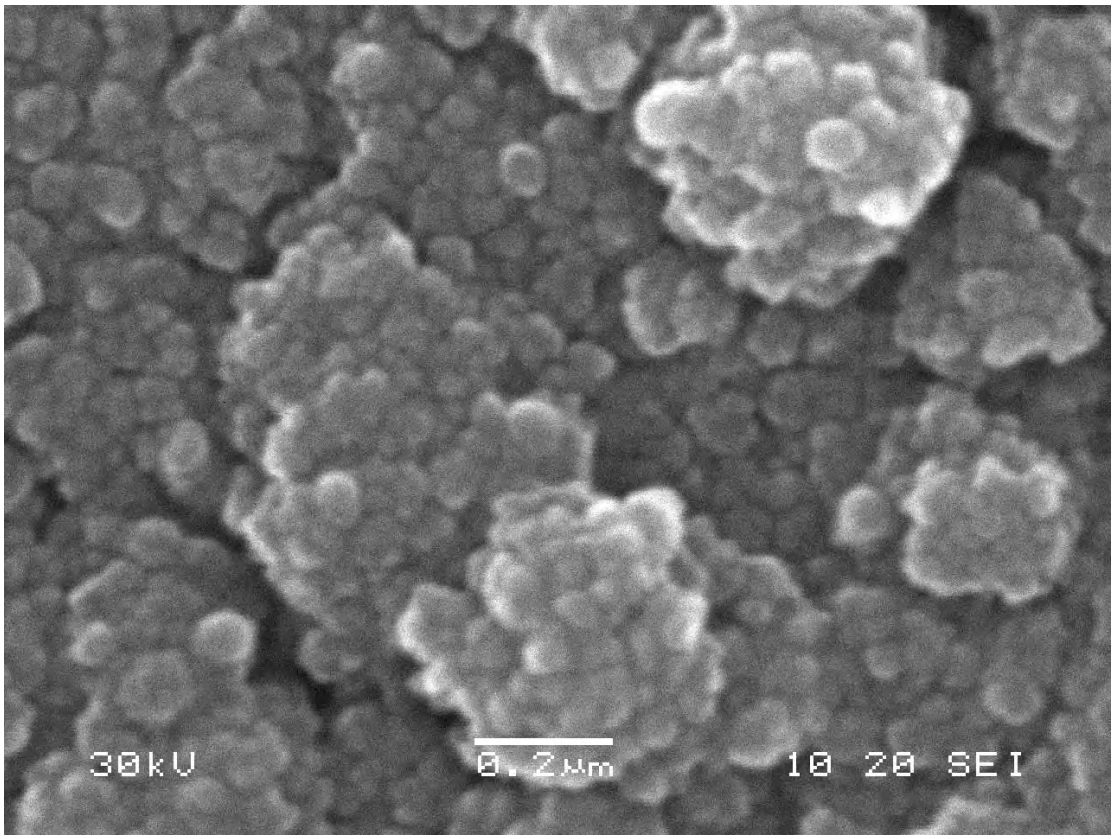

FIGURE 6.8: SEM micrograph of film deposited by femtosecond PLD (film 20).

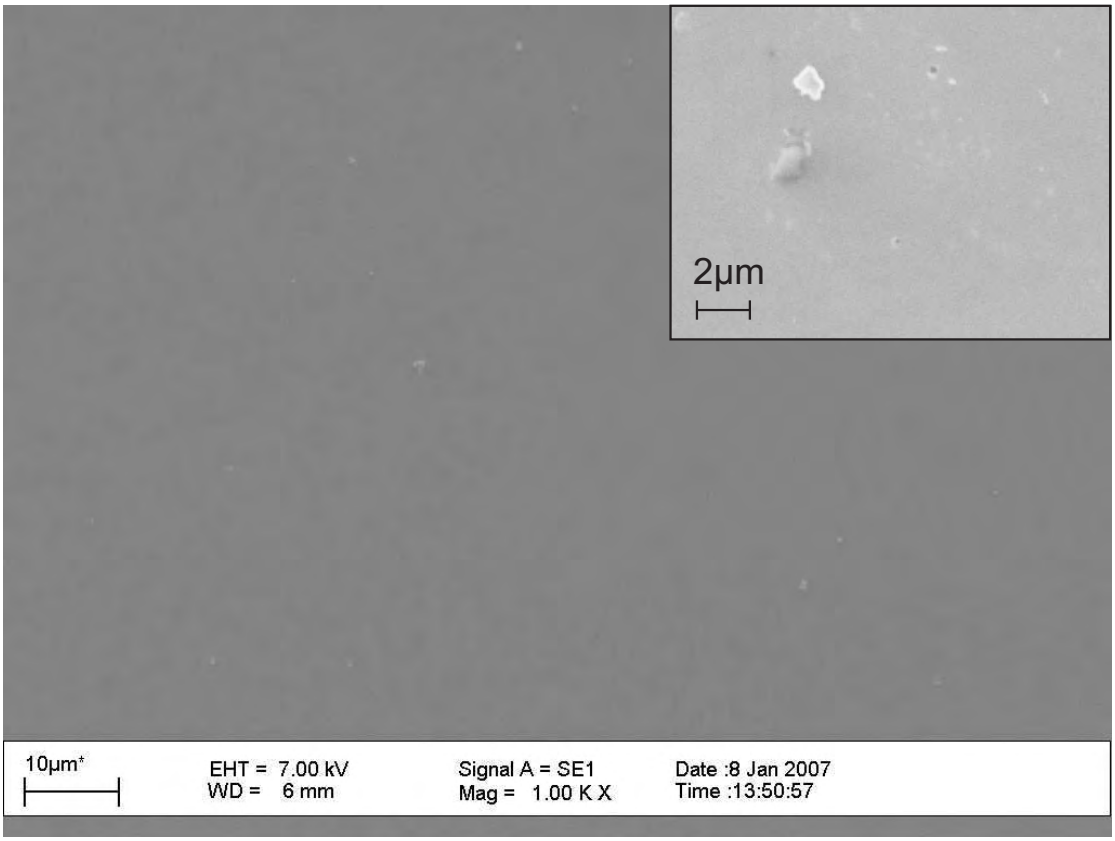

FIGURE 6.9: SEM micrographs of a film deposited by nanosecond PLD (film 1). The inset shows a higher magnification SEM micrograph of the same film.

6.3.4 Phase-change memory device

A phase-change memory device was fabricated using nanosecond PLD[2]. A GLS film was deposited onto a microscope slide onto which was sputter-deposited a series of ten parallel chromium strips (1 mm by 50 mm by 200 nm), each separated by 5 mm. After deposition, the GLS film was then coated with another series of strips perpendicular to the bottom electrodes using an Edwards coater. This enabled localised current flow and heating of specific areas (cells) of the film. A photograph of the device is shown in figure 6.10.

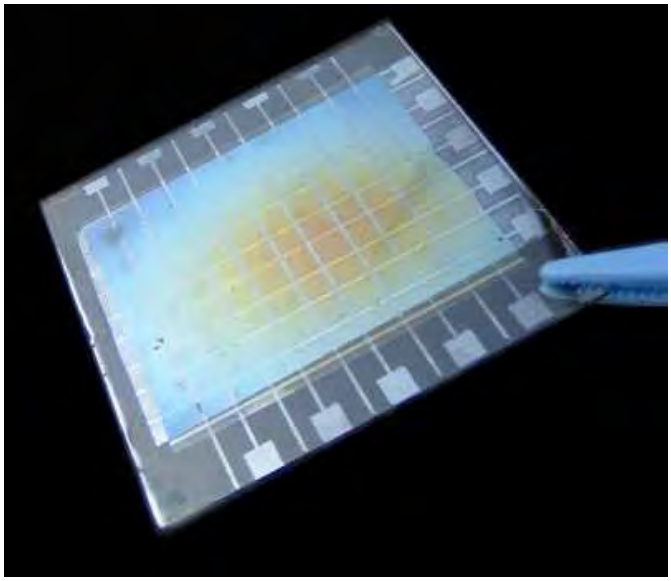

FIGURE 6.10: GLS film deposited on a 10 by 10 array of Cr electrodes using nanosecond PLD.

The variation in composition of the film, which was due to the large area of the GLS coating, could potentially yield valuable information on the switching characteristics of GLS film material for various compositions. The primary goal of this investigation was to find the optimum composition for phase-change memory, characterised by low threshold switching voltage and a large difference between the resistance of the respective phases. The I-V characteristic of each cell was measured using an electrometer (*Keithley 238*), which was programmed to increase the voltage in 1 V steps and measure the current flowing through the sample for a duration of 100 ms. The electrical resistivity of the material was calculated from these measurements. The spread in resistivity on the chip is plotted in figure 6.11. The black circles shows the position of the cells that switched to a lower resistivity and figure 6.12 shows the I-V characteristics of selected cells.

[2]This work was performed in collaboration with R. E. Simpson and D. Hewak (ORC)

The resistance of cell (4,8) is shown to decrease at a threshold voltage of roughly 60 V, which may indicate that the region has switched phase. Although X-ray diffraction analysis of the cell before and after the event would be required to confirm this, the resistance of GLS in its crystalline phase is known to be lower than in its amorphous phase. Many of the cells, for example cells (1,9) and (2,8), are shown to have performed the opposite, that is to have increased in resistance at a threshold voltage. Some of the cells did not show any threshold changes in the resistance, for example cell (3,10) is shown to fluctuate slightly and does not exhibit any threshold changes. The threshold at which many of the cells are shown to change in resistance, either increasing or decreasing is variable between 40 and 80 V and there does not appear to be any correlation of these characteristics with the position (and hence composition and thickness) of the cells on the film. Unfortunately, further investigation into the device could not be undertaken since it was destroyed by fire.

It is possible that the inhomogeneity of each of the cell's I-V characteristics was caused by the film separating from the surface of the substrate. Surface features were identified on some of the films by SEM analysis (the device sample was not analysed), which may have had an effect on the electrical characteristics if these were situated between the electrodes of the cells. The surface of one film deposited under similar

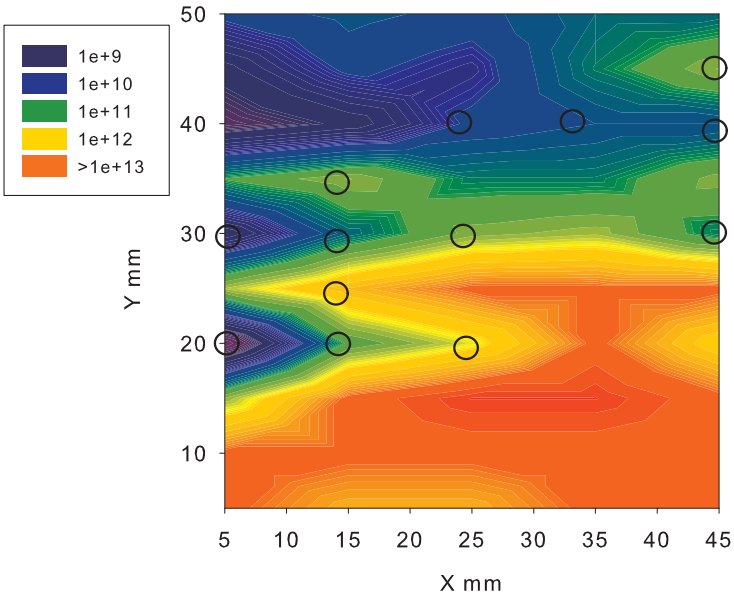

FIGURE 6.11: Electrical resistivity of a GLS film deposited by nanosecond PLD as a function of position on the substrate. The black circles show the position of cells that switched to a lower resistivity. The legend shows the measured values of electrical resistivity in Ωm (measured by R. E. Simpson (ORC)).

conditions shows cracking and delamination (figure 6.13), which would certainly have a detrimental effect on the electrical characteristics of any phase-change device. XRD analysis confirmed they were amorphous.

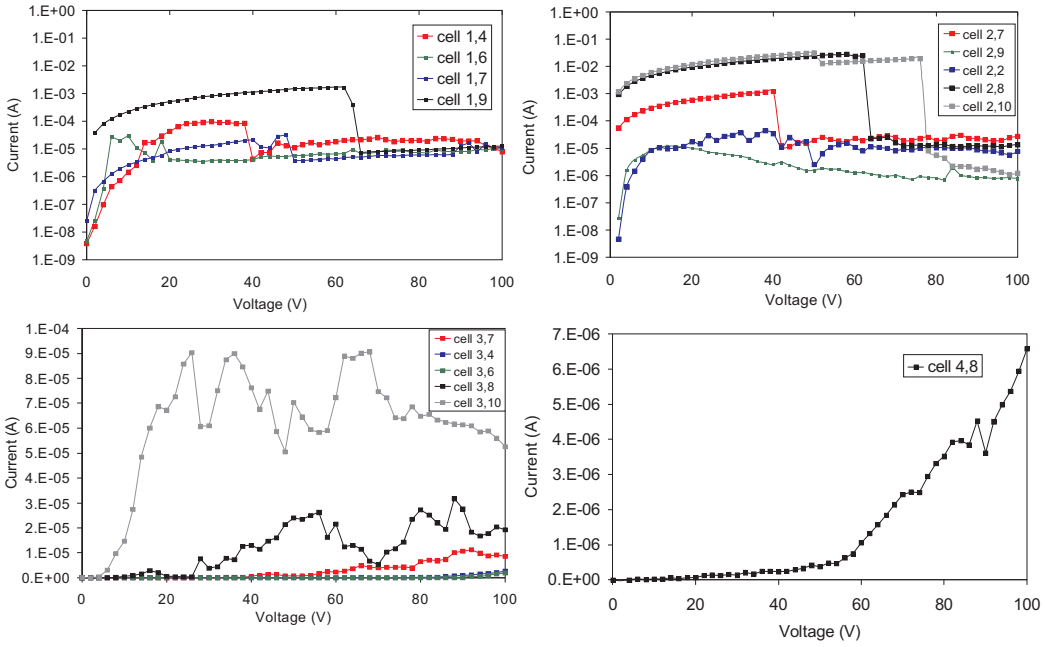

FIGURE 6.12: I-V characteristics of selected cells (measured by R. E. Simpson(ORC)).

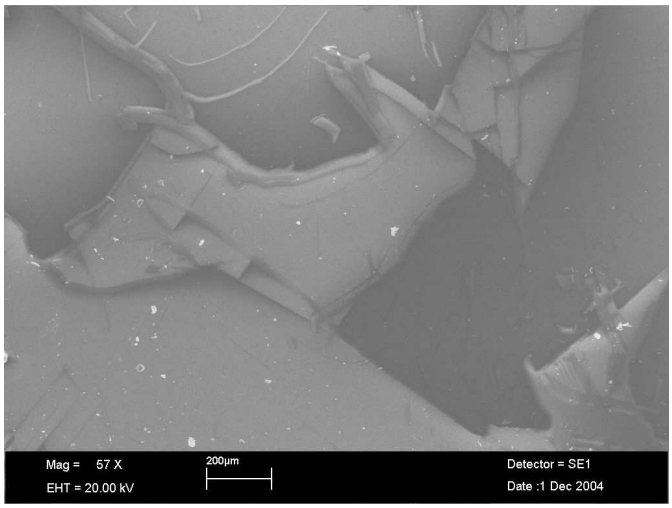

FIGURE 6.13: SEM micrograph of a film deposited by nanosecond PLD. Note that the film has undergone delamination.

6.4 Effect of high-intensity, short-pulse laser regime on film composition

The effect of the femtosecond regime on the film's compositions is not generally well-known due to the limited number of reports of short-pulse duration PLD experiments (see table 5.1). However, work conducted by Millon et al. (2003) has revealed some of the characteristic differences of the composition of films produced by femtosecond and nanosecond PLD. Using a 90 fs pulse duration laser with a 620 nm wavelength and 10 Hz repetition rate they deposited $BaTaO_3$ films, which consisted of crystalline $BaTiO_3$ with a surface morphology that revealed large ($\sim$ 1µm) particulate-like structures on the surface. Their analysis of the composition showed that the distribution of the Ba:Ti ratio in the film strongly depends on the angular position of the substrate (relative to the normal to the target at the laser impact point). Films at larger angular positions were richer in the heavier element Ba. Indeed, the Ba/Ti ratio more than doubled when the angular position was moved from 0 ° to 40 °. $BaTiO_3$ films grown by PLD with an ArF excimer laser (193 nm) in the nanosecond regime show that the Ba/Ti ratio remains almost constant at around unity for angular positions from 0 ° to 25 ° (albeit slightly decreasing by a faction of a percent). The finding in this chapter agrees with trend observed by Millon et al. (2003) that suggests that femtosecond PLD results in enrichment of the heavier element at larger off-axis angles.

6.5 Conclusions

This chapter has presented experimental results of the deposition of GLS material using femtosecond and nanosecond regime lasers. There are several outstanding differences between these two regimes. The surface of the femtosecond laser-deposited films is covered in particulates, which are present for the range of deposition conditions we have investigated. However, the size of the particulates is affected by the laser fluence, with smaller particulates observed on films deposited at lower laser fluences. The nanosecond films are comparatively smoother, with a relatively low density of particulates, many of which are presumed to have formed from target fragmentation. The compositional spread of the film shows different characteristics: at higher angular deviations the femtosecond-laser deposited films have a gradually increasing Ga:La ratio, whereas the nanosecond-laser deposited film show an opposite trend.

Generally, pulsed laser deposition has shown itself to be useful for fabricating amorphous films with a wide range of compositions. The influence of the deposition parameters on the composition of deposited films is a useful means for engineering film compositions. Femtosecond PLD has shown itself to be a highly non-stoichiometric deposition method, producing films with a Ga:La ratio that can be varied (by changing the deposition parameters) between 0.12 – 0.78 for a target with a Ga:La ratio of roughly unity.

In light of these discoveries, nanosecond PLD is a more favourable method for depositing GLS films that are to be used for optical applications. For femtosecond films to be useful in these areas there is a need to reduce the effect the particulates will inevitably have on the optical loss of the medium. One method to achieve this would be to re-melt and fast-quench the film, thus integrating the particulates into the film material and reducing the affect they have on the scattering losses.

Chapter 7

Gallium Enrichment of Nd:GGG by Combinatorial PLD

This chapter will present an experimental study into PLD using two nanosecond pulse duration lasers to simultaneously deposit material from two dissimilar targets onto a single substrate. The aim of this work is to compensate for the loss of gallium observed in GGG films grown by conventional PLD (May-Smith & Eason 2007) by enriching the plume with gallium from an additional gallia target.

Films were produced from synchronised ablation of two different targets of single-crystal Nd:GGG and hot-pressed Ga_2O_3. The gallium concentration in the resultant film was controlled by changing the fluences on the respective targets. This chapter will show how this technique can lead to deposition of film material with a Gd/Ga ratio both *above* and *below* that of stoichiometric GGG. The inclusion of additional gallium in the film is shown to progressively decrease the lattice parameter of the resultant film material. With higher proportions of gallium, the lattice parameter is found to be smaller than the database value for stoichiometric GGG.

This chapter begins by discussing the origins and background work on multi-target PLD. It will explore the main differences between two interacting plumes and single-plume PLD and present the prior work conducted on multi-target PLD. It will then discuss the possible mechanisms by which gallium-excess and gallium-deficient films can be produced. The effect garnet composition has on the lattice parameter is modelled using empirical formulas, and the method for substitution of excess Ga in the GGG structure is discussed.

7.1 Introduction

7.1.1 Prior art

The concept of multi-target PLD was initially proposed by Gaponov et al. (1982) to overcome the problems of particulate contamination in PLD films. The essential feature of this technique is the creation of an artificial collision region having a high pressure produced by colliding two laser-produced plasmas. The heavy particulates with a large momentum, traverse the interaction region with little perturbation, while the plasma expands towards the substrate. If the mean free path of the atoms in the intersection region is smaller than the intersection region, the atoms, ions and other plume components will be re-directed from their initial direction. This technique was applied ten years later with the introduction of a diaphragm that shadowed the substrate from the direct line-of-sight of the ablated areas and a reduction in the density of droplets on the film's surface was reported (Pechen et al. 1992).

This technique has grown in popularity recently and is now referred to as *cross-beam* PLD (Gorbunov et al. 1996). A typical set-up is shown in figure 7.1(a). The two laser beams strike two separate targets close to one another and the substrate is located on a symmetrical axis between the two intersecting laser plumes. Between the targets are two v-shaped diaphragms, positioned in such a way that the laser ablation spots cannot be seen directly from the substrate position. This technique has been used successfully to reduce the number of particulates in films deposited from a range of targets (Gorbunov et al. 1996, Lambert et al. 1999, Tselev et al. 2001).

In the cross-beam PLD set-up, the particle energies in the re-directed plasma plume can have a critical influence on the number of particulates deposited on the films. Early work by Strikovsky et al. (1993) on the deposition of high-temperature superconductor films ($YBa_2Cu_3O_7$) revealed that the surface morphology of the films depends on the distance between the substrate and the crossing point of the plasma fluxes. Droplet-free films were obtained only for a narrow range of distances (54 – 58 mm). At short distances, the substrate contained large crystals formed from the film overheating or melting from the energy of the dual-plasma flux, whereas at larger distances the plasma was sufficiently cool to form a high concentration of condensed droplets.

The energetic characteristics of two interacting plumes have been investigated by Tselev et al. (1999). In their work, time-of-flight measurements using the Langmuir probe technique were applied to obtain kinetic energy distributions of the ionised species from

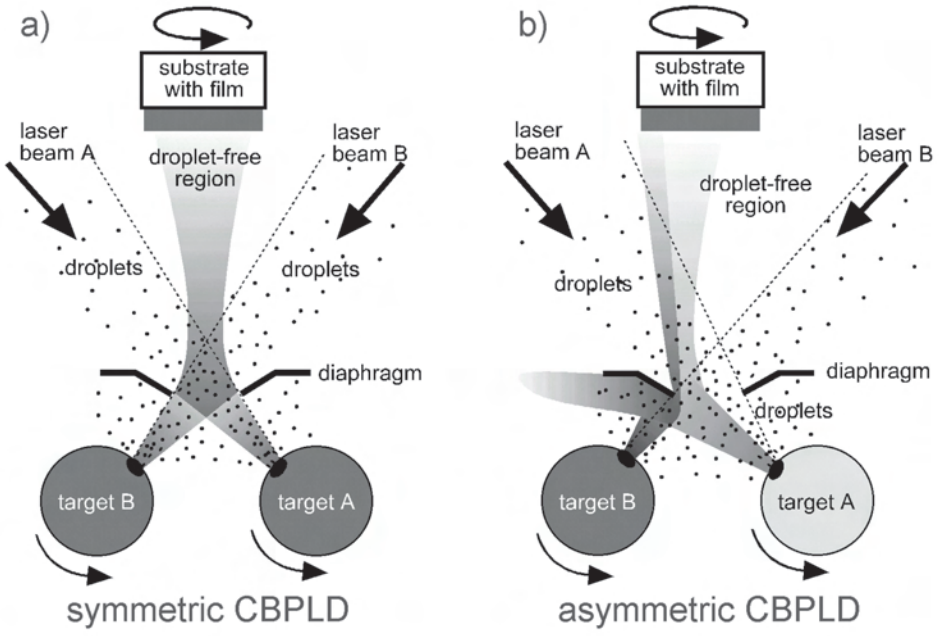

FIGURE 7.1: Schematic diagram of the a) cross-beam and b) asymmetric cross PLD techniques (after Gorbunoff (2007)).

several metal targets and a comparison was made with conventional PLD. The average kinetic energy of the ions in the cross-beam geometry was found to be roughly 2 - 3 times lower compared to conventional PLD, while the proportion of ionised species was found to be 1.5 - 2 times larger. They also found that the angular width of the plasma plume was comparable with conventional PLD. High energy species were found to travel through the intersection region without being affected, which was believed to be due to the lower density of the leading edge of the plasma resulting in a larger mean free path of the ions.

Measurements made by Sánchez Aké et al. (2007) using time resolved optical spectroscopy on two interacting plumes produced from graphite targets found that the intensity of emitting ions was higher while the number of emitting neutrals was less than in conventional PLD. It was also shown that the velocities of the ions produced from one of the targets can be controlled by varying the delay between the laser pulses. The collision process in the intersection region is responsible for the change in the kinetic energy and an increase in the ionised species in the collision region.

The primary aim therefore of cross-beam PLD until recently has been to reduce the particulate concentration in films. Alternatively, this technique can be used to control the film's stoichiometry. There have been a few reports on the deposition of intermetalic

compounds by cross-beam PLD using two disimilar targets. In particular, asymmetric cross-beam PLD arrangement (figure 7.1(b)) proposed by Gorbunov et al. (1999), in which two laser plumes are positioned in such a way as to result in a variable film composition, has been used to deposit a range of compositions of Fe-Al, Fe-Cr and Co-Cu films (Gorbunov et al. 1999, 2002). Multilayers of Fe-Al have been fabricated by alternating the number of pulses on different targets (Levin et al. 2001). Work by Irissou et al. (2006) on the cross-beam PLD of films from two dissimilar targets has shown that films with mixed Pt-Au and Pt-Ru compositions can be prepared over the whole compositional range with Pt at. % from 0 to 100 using this technique.

7.1.2 Structure of garnets

The cubic unit cell of a garnet crystal structure contains eight units of $A_3B'_2B''_3O_{12}$ and has a space group of $Ia3d$ (Galasso 1970, p. 244). The metal ions A, B′ and B″ occupy the 24c, 16a, and 24d sites, respectively, and the O^{2-} ions occupy the 96h sites. The structure can be viewed as interconnected dodecahedrons (A sites), octahedrons (B′ sites), and tetrahedrons (B″ sites) with shared O^{2-} ions at the corners of the polyhedra. Each oxygen is a member of two dodecahedra, one octahedron, and one tetrahedron. Part of the structure is depicted in figure 7.2 around a single oxygen atom, showing the three cation lattice sites.

For stoichiometric GGG crystal, the A site is occupied by a Gd^{3+} ion, and the B′ and B″ sites are occupied by Ga^{3+} ions. There is a degree of flexibility on the location of the Gd^{3+} ion however, which can occupy the dodecahedral or the octahedral sites. Calculation of the electronic structure of GGG has been performed recently by Xu et al. (2000b).

7.1.3 Imperfections and non-stoichiometry

All crystals are imperfect to some degree and dislocations and defects will always occur during crystal growth. There are broadly three types of imperfections: dislocations, point defects and vacancies.

A dislocation can be considered to be an insertion of an extra lattice plane of atoms into the crystal lattice and can occur from a build-up of strain in the crystal. The crystal planes are distorted and the lattice is dilated at the line where the plane is introduced

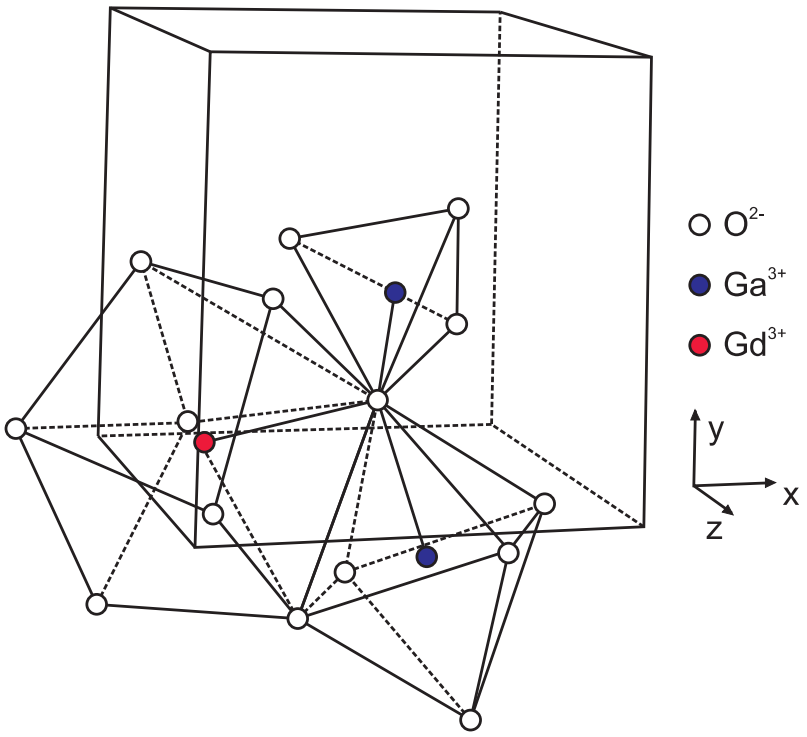

FIGURE 7.2: Structure of $Gd_3Ga_5O_{12}$, showing the dodecahedral, octahedral and tetrahedral lattice sites about one oxygen atom.

(figure 7.3(a)). These defects can become detrimental to the growth of good quality crystal when lattice mismatch is high.

A further class of imperfections are termed point defects (figure 7.3(b)), which is described as the presence of an atom at an interstitial position that distorts the host lattice. If they occur in sufficiently large numbers they can destabilise the crystal and eventually result in a phase transition.

Vacancies are caused by the removal of atoms to another position in the lattice, and are divided into two different types: Frenkel defects and Schottky defects. A Frenkel defect is the creation of a vacancy by the removal of an atom to an interstitial position (figure 7.3(c)). A Schottky defect is the formation of a cation and anion vacancy (figure 7.3(d)). If one of the cations has a multiple charge, then it will be counter-balanced by the removal of the appropriate number of anions to maintain overall neutrality. Schottky defects occur by ions leaving their lattice positions and taking a position of the surface of the growing crystal. Another type of defect arises from an atom occupying an incorrect lattice site, called an anti-site defect. The formation of an anti-site defect is one of the dominant mechanisms for non-stoichiometry in ionic crystals since it often requires less energy to form.

Imperfection and non-stoichiometry are of enormous importance to the properties of a crystal and if a material is grown with the incorrect stoichiometry, vacancies, point defects and anti-site defects may occur more frequently. This can result in the crystal becoming increasingly unstable, and if the non-stoichiometry of the crystal reaches a point where the incorporation of these defects becomes energetically less favorable than the formation of another phase, then the crystal will undergo of phase transition.

7.1.4 Effective ionic radii

In an ionic crystal the attractive Coulomb force is counter-balanced by the repulsive force of the outer electron shells of the ions, resulting in an equilibrium internuclear distance. Because of the short-range of the repulsive force and its rapid increase as ions are brought closer together, it is possible to consider them as classic spheres with defined radii.

The sizes of the cations is one major factor in determining site preferences in garnets (Geller 1967). Historically, a number of different sets of ionic radii have been compiled using different methods (Ahrens 1952, Pauling 1932), although the most widely used

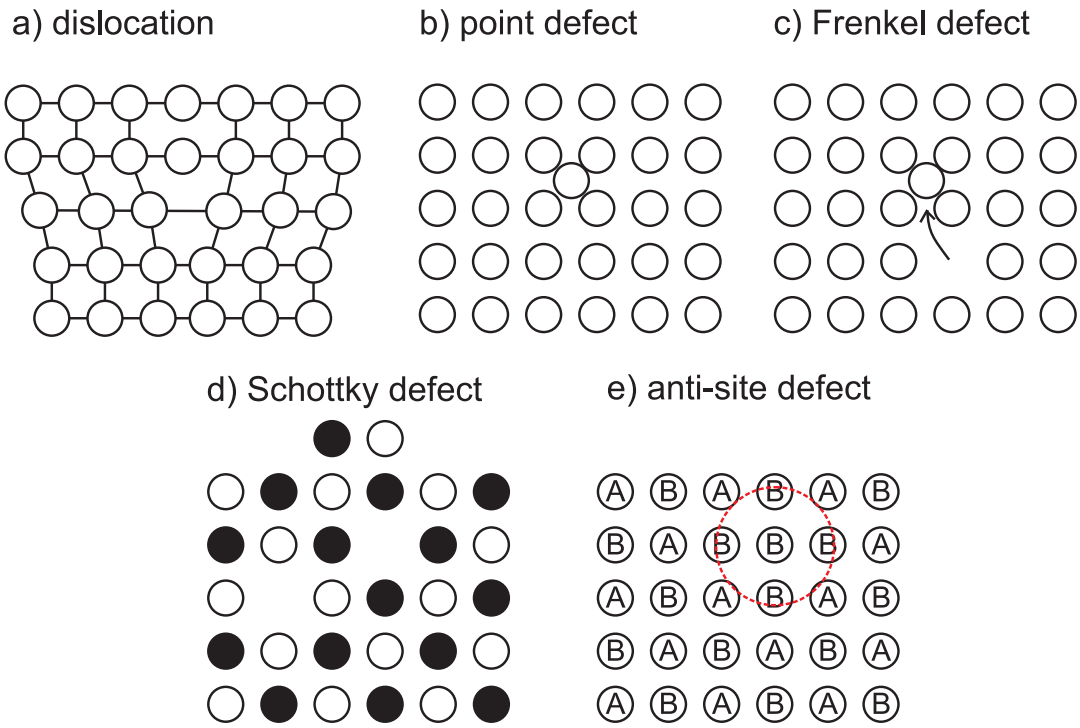

FIGURE 7.3: Imperfections in a crystal lattice: a) dislocations, b) point defects, c) Frenkel defect, d) Schottky defect (open and filled circles are oppositely charged atoms) and e) anti-site defect.

today are those of Shannon & Prewitt (1969). Table 7.1 shows a list of the effective ionic radii of Ga^{3+}, Gd^{3+} and Nd^{3+} ions with their corresponding co-ordination number.

Ion	c.n.	Ionic radius
Ga^{3+}	4	0.47
Ga^{3+}	6	0.62
Gd^{3+}	6	0.938
Gd^{3+}	8	1.053
Nd^{3+}	8	1.109

TABLE 7.1: Effective ionic radii of the Ga^{3+}, Gd^{3+} and Nd^{3+} ions with their respective co-ordination numbers (c.n.) (Shannon 1976).

7.1.5 Cation site preferences and non-stiochoimetry

There is a larger body of work on cation site preferences for garnet structures (Geller 1967, Maglia et al. 2006, Milanese et al. 2004, Nakatsuka et al. 1995). Early work by Geller (1967) reviewed many garnets and found the preferred lattice sites of the ions were primarily determined by their ionic radii.

More recently, static-lattice atomistic calculations (Maglia et al. 2006) have been preformed to study the preferred lattice sites for a range of ions in various garnets. This technique involves calculating the energy of the solid by considering the potential energy of a given ion in the structure. The word 'static' is used because entropy and energy contributions from lattice vibrations are not included. In this technique, the position of the ions in the lattice is adjusted until the minimum energy configuration is found. The individual energy of an ion in a particular lattice site is found by estimating the potential energy between a given pair of ions (pair-wise potential) (Catlow & Mackrodt 1982).

The energy corresponding to the incorporation of the cations in all three sites for a range of gallium and aluminum garnets has been predicted recently using this method (Maglia et al. 2006). The calculated solution energy, which is the heat energy required to dissolve 1 mol of the binary oxide M_2O_3 (M=chosen dopant cation) into the lattice, was calculated for the various site occupations (dodecahedral, octahedral, or tetrahedral). These simulations have shown that the preferred lattice site for the Ga^{3+} ion is the octahedral or tetrahedral sites, with very little difference (< 0.1 eV) in the calculated solution energy for either site occupation. The occupation of the Ga^{3+} ion in the dodecahedral lattice site is energetically unfavourable and requires a relatively higher

solution energy of roughly 2 eV. Even though the preferred lattice site for the Gd^{3+} ion is the dodecahedral, the calculated solution energies for the occupation of the octahedral site is less than 1 eV (Maglia et al. 2006), and therefore, inclusion of the Gd^{3+} in the octahedral site is expected, and has been experimentally observed (Brandle & Barns 1974).

Inclusion of the smaller Ga^{3+} ions in the octahedral lattice sites (as compared to gallium-deficient GGG deposited by PLD, where the larger Gd^{3+} ions occupy a small fraction of the tetrahedral lattice sites) is more energetically favorable than Gd incorporation in the same site, and requires a lower energy. Therefore, when the Gd/Ga ratio is reduced to 0.6 all available Ga^{3+} sites are full and the Ga atoms are forced to either occupy some of the dodecahedral lattice sites or become incorporated in the lattice in the form of defects.

There are a number of different defects that can result in higher concentrations of gallium (as compared to stoichiometric GGG), such as: i) a point defect, where a number of Ga atoms are inserted into the lattice at interstitial positions i) a Schottky defect, where a number of Gd^{3+} and an O^{2-} are removed from the lattice; ii) a Frenkel defect, where extra Ga atoms are inserted into the crystal at interstitial positions and a vacancy occurs in either the Ga or Gd lattice sites; iii) a Gd^{3+} vacancy and an increase in charge on some of the remaining ions, iv) an anti-site defect, where a number of Ga atoms occupy the dodecahedral lattice sites. If vacancies occur in large numbers the dimensions of the unit cell will be effected. The Coulomb repulsion of the anions will force them apart and they will no longer be repelled by the cation's outer election shells and the structure will also become increasingly unstable. The creation of a Schottky vacancy expands the volume of the lattice, whereas Frenkel vacancies are matched within the crystal volume by an equivalent number of interstitial ions (Greenwood 1968).

The energy corresponding to the formation of various defects has been predicted using atomistic calculations (Milanese et al. 2004). It was found that the most dominant form of defect occurs in the form of an anti-site defect. In the case for GGG, this occurs in the form of a Ga atom occupying the dodecahedral lattice site. Formation of Schottky and Frenkel defects was found to involve much higher energies (2.4 to 5 eV for a range of garnets). The incorporation of excess Ga by the simultaneous formation of anti-site defects, cation vacancies, and oxygen vacancies is less favorable than formation of anti-site defects alone, and as a consequence the number of oxygen vacancies in Ga-rich (Gd/Ga$<$ 0.6) GGG is predicted to be small.

An important consideration for mixed garnets is their solubility. When choosing to mix two or more garnets from separate targets it is important that the resultant hybrid garnet forms a stable structure. Garnets of mixed composition with the general formula $\{A_{3-x}B_x\}C_5O_{12}$ have been fabricated (see review by Geller (1967)) and the maximum value of x generally depends on the ionic size mismatch between the A and B ions. This is in agreement with the solution energies found for the incorporation of cations in a given garnet (Milanese et al. 2004). Lower solution energies are found when the ionic sizes of the dopant cations are closer to the host ions (in the preferred lattice site).

7.1.6 Lattice parameter variations in garnets

Strocka et al. (1978) have obtained a relation for the calculation of the dimensions of a garnet unit cell on the basis of investigated garnets. The formula was developed assuming that only cation sizes, distribution and composition affects the lattice parameter. It describes the relation for the lattice parameter a, as a function of the effective ionic radii of the ions in their respective lattice sites using the radii measured by Shannon & Prewitt (1969). The algebraic relation $a = f(r_{VIII}, r_{VI}, r_{IV})$, where r_{VIII}, r_{VI} and r_{IV} are the effective ionic radii in the dodecahedral, tetrahedral or octahedral lattice sites was obtained from the following garnets,

$$R_3M_5O_{12}$$

$$R = Y^{3+},\ La^{3+},\ Lu^{3+}$$

$$M = Fe^{3+},\ Al^{3+},\ Ga^{3+}$$

and from the following substituted garnets,

$$R_3M_uFe_{5-u}O_{12}$$

$$M = Al^{3+},\ Ga^{3+},\ In^{3+},\ Sc^{3+}$$

$$R_{3-u}Ca_uM_uFe_{5-u}O_{12}$$

$$M = Ge^{4+},\ Si^{4+},\ Zr^{4+},\ Sn^{4+},\ Ti^{4+}$$

The empirical formula, derived by the least-squares method, yielded the following relationship between the lattice parameter and the effective ionic radii of the ions in their

sites,

$$a = b_1 + b_2 r_{VIII} + b_3 r_{VI} + b_4 r_{IV} + b_5 r_{VIII} r_{VI} + b_6 r_{VIII} r_{IV}, \tag{7.1}$$

where b_1 to b_6 are given by,

$$b_1 = 7.02954 \qquad b_2 = 3.31277$$
$$b_3 = 2.49398 \qquad b_4 = 3.34124$$
$$b_5 = -0.87758 \qquad b_6 = -1.3877$$

It must be noted that this model considers lattice parameter variation only by the uniform deformation due to the cation sizes. Changes in the cubic symmetry (Dong & Lu 1991) and ionic state with the distribution of the cations has not been taken into account.

Prior to the work by Strocka et al., formulas for the lattice parameter of garnet compositions based on the ionic radii measured by Ahrens (1952) have been given (Suchow & Kokta 1972, Talanov et al. 1975). Calculations have been performed by Glass & Elliott (1974) for the expansion of YIG ($Y_3Fe_5O_{12}$) films caused by the incorporation of lead atoms in the lattice. Lattice constants published by Winkler et al. (1972) of a range of polycrystalline garnets have also yielded a dependence on the compositional parameter. More recently, a range of over 350 garnet compositions has been investigated and an empirical formula, similar to formula 7.1, has been given for the lattice parameter (Vorobiov & Carban 1997).

Earlier work by Allibert et al. (1974) obtained a formula for the lattice parameter variation[1] of $\{Gd_3\}[Gd_xGa_{2-x}](Ga_3)O_{12}$, which is given by,

$$a = 12.375 \left[1 + \left(\frac{r_{Gd}}{r_{Ga}} - 1\right) \times 0.0268x\right], \tag{7.2}$$

where r_{Gd} and r_{Ga} are effective ionic radii of the Gd^{3+} and Ga^{3+} in the octahedral lattice sites. Substituting 0.939 Å and 0.620 Å (Shannon 1976) for r_{Gd} and r_{Ga}, respectively, the formula can be written as,

$$a = 12.375 + 0.170x. \tag{7.3}$$

[1]The brackets denote the lattice sites: dodecahedral { }, octahedral [], and tetrahedral ( )

A range of compositions was fabricated by Allibert et al. (1974) using the Czochralski method with x in the range 0.5 to -0.5.

The above formulas can be used to predict the lattice parameter of various garnet compositions if the location and size of the ions in their respective sites are known. For non-stoichiometric garnets, where site exchange occurs between the ions, it is possible to assign the site location of an excess metal by predicting its preferred lattice sites.

If we consider a GGG crystal for which the Gd^{3+} cation is substituted into the octahedral lattice site such that the formula becomes $\{Gd_3\}[Gd_xGa_{2-x}](Ga_3)O_{12}$. This form of Gd substitution has been observed in Czochralski-grown GGG (Allibert et al. 1974, Brandle & Barns 1974, Makino et al. 1976). Assuming the average radius for the cation in the lattice is related to the mole fraction of the elements, and that the substitution of the cations is randomly distributed in the lattice sites, then the average radius of the ion in the octahedral lattice site can be calculated by,

$$r_{VI} = r_{Ga} + \frac{x}{2}\left(r_{Gd} - r_{Ga}\right), \tag{7.4}$$

where r_{Gd} and r_{Ga} are the effective ionic radii of Gd^{3+} and Ga^{3+} atoms in octahedral co-ordination (Shannon 1976). On the basis of this prediction, the lattice parameter can be estimated for a range of GGG garnet compositions. Figure 7.4 shows the measured lattice parameter of GGG films deposited using an excimer laser (λ =248 nm) (May-Smith & Eason 2007) and the estimated lattice parameter according to Stroka's formula.

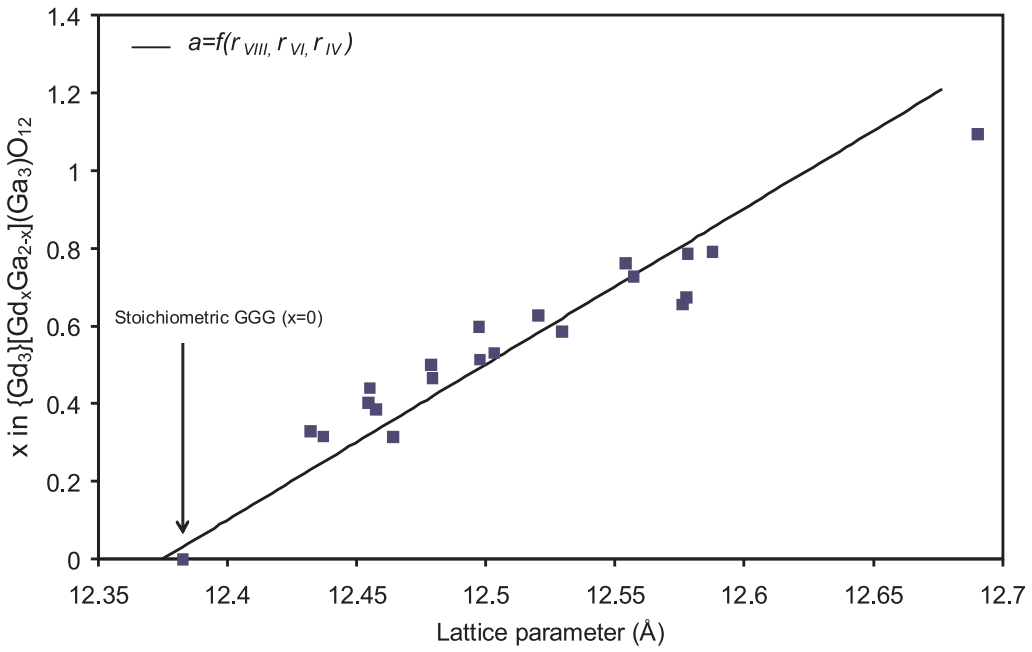

FIGURE 7.4: The measured lattice parameter for a range of film compositions deposited by PLD. (data from work by May-Smith & Eason (2007)). The solid line is the estimated lattice parameter according to equations 7.1.

7.2 Experimental

The experiments were conducted in a vacuum chamber using oxygen as a background gas. Two synchronised frequency-quadrupled Nd:YAG lasers ($\lambda = 266\,\text{nm}$), operating at a repetition rate of 10 Hz with pulse duration of 10 ns were focused onto two separate targets of Nd:GGG (1% at. Nd doped) and Ga_2O_3 (99.99% purity). The Nd:GGG target was cut from a piece of bulk-grown crystal (OSICO Technologies Inc, China), whereas the Ga_2O_3 target was hot-pressed from powder with a maximum particle size of about 7 µm (Cathay Advanced Materials Ltd, China). The incident laser beams were directed onto the targets so that the ablation plumes were coincident on a polished YAG substrate of dimensions $1.0 \times 1.0 \times 0.1$ cm. Both targets were rotated at 10 revolutions per minute and, since they were both positioned off axis, were set at a given angle of $\sim 29°$ relative to the substrate normal. A schematic of the arrangement is shown in figure 7.5. A raster-scanned CO_2 laser with a wavelength of 10.6 µm and a maximum output power of 32 W used for substrate heating. The laser beam was raster-scanned over the rear surface of the substrate using a pair of galvanometric mirrors. An absorbed CO_2 laser power of 6.3 W was required to obtain an optimal substrate temperature (previously

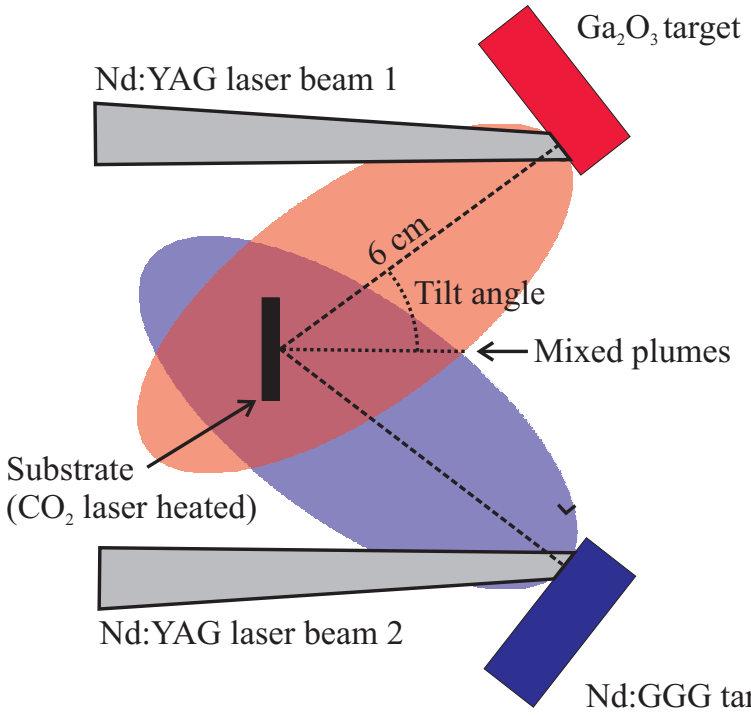

FIGURE 7.5: Experimental set-up for combinatorial PLD of Nd:GGG and Ga_2O_3.

estimated to be approximately 750℃). The substrate was held in place with specially made ceramic alumina posts to minimise heatsinking. The amount of gallium enrichment was defined by the deposition rates from the two targets, and this was changed by altering the fluence on each target by changing the energies of the two Nd:YAG lasers. Each compositional measurement was taken over an area of 20,µm by 20 µm, and a 4×4 array of equally spaced locations were analysed so that an average could be taken. The standard deviation of the measured atomic percentage over this area was 0.27% for gallium and 0.31% for gadolinium.

7.2.1 Effect of Ga_2O_3 enrichment

Table 7.2 shows the deposition conditions for films deposited with a mixture of laser ablated plumes from Nd:GGG and Ga_2O_3 targets alongside the lattice parameter, calculated from the 2θ position of the (400) GGG peak, and the measured Gd/Ga ratio. The spot-sizes (major and minor axis diameters of an ellipse) on the GGG and Ga_2O_3 targets were 1.5 by 2.5 mm and 1.5 by 2.2 mm, respectively, and the fluence was changed by altering the energy of the ablating laser. The target-substrate distance was kept at 6.0 cm. The tilt angle of the target holders was kept at 28.5° and depositions were conducted for a duration of 30 minutes.

	Fluence on targets (J/cm^2)				
Sample	GGG	Ga_2O_3	Pressure (mbar)	Lattice parmeter (Å)	Gd/Ga ratio
1	1.5	2.5	0.04	No peak	0.11
2	1.5	1.7	0.04	12.34	0.56
3	2.3	1.7	0.04	12.36	0.57
4	2.3	1.1	0.04	12.36	0.65
5	2.3	-	0.04	12.40	0.67
6	1.5	-	0.04	12.49	0.83
7	2.3	1.6	0.0044	12.44	0.77
8	2.3	1.6	0.00024	No peak	2.44

TABLE 7.2: Deposition conditions for films deposited using a combination of Nd:GGG and Ga_2O_3 targets.

Figure 7.6 shows expanded-view XRD spectra of the (400) GGG peak for films deposited with various combinations of fluences on the Nd:GGG and Ga_2O_3 targets (samples 1-6). Other than the corresponding (800) GGG film and (800) YAG substrate peaks, no other peaks were detected outside the 2θ range shown in figure 7.6.

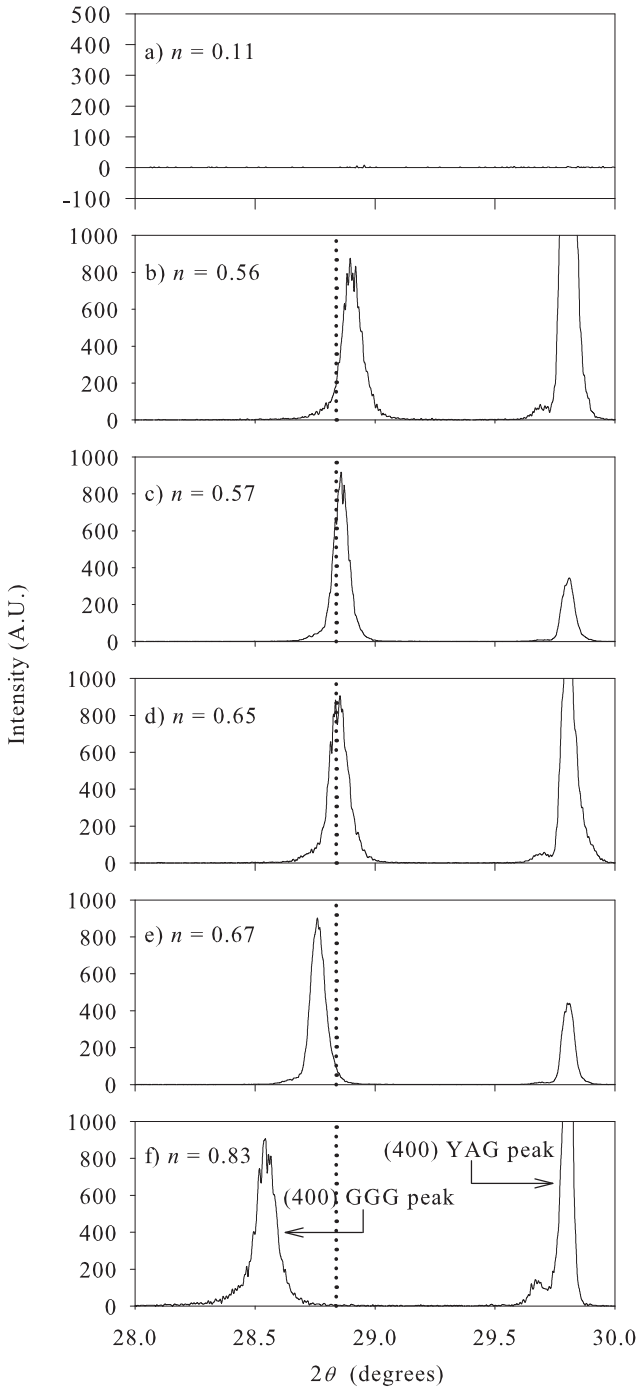

FIGURE 7.6: XRD spectra of films deposited with various fluences on the Ga_2O_3 and Nd:GGG targets of (a) 2.5 and 1.5 J/cm^2, (b) 1.7 and 1.5 J/cm^2, (c) 1.7 and 2.3 J/cm^2, (d) 1.1 and 2.3 J/cm^2 (samples 1-4), respectively, and on the Nd:GGG target only of (e) 2.3 J/cm^2, (f) 1.5 J/cm^2 (samples 5 and 6). The dotted line corresponds to the position of the (400) GGG peak for stoichiometric composition ($2\theta = 28.839°$ (Sawada 1997)). The intensity of the GGG (400) peaks have been normalised. The peak intensities of the YAG (400) substrates peaks are different because the films may have different thicknesses. The cationic ratio, n =Gd/Ga, was measured for each sample using EDX analysis.

Figure 7.7 shows the calculated film lattice parameter plotted against the measured cationic ratio (n =Gd/Ga) for samples 2-6.

There is a distinctive increase in the observed (400) GGG film peak position for increasing values of Gd/Ga ratio. Film material deposited only from the Nd:GGG target has a lattice parameter that is larger than the database value for stoichiometric GGG (12.383Å (Sawada 1997)) and is deficient in Ga (samples 5 and 6). Increasing the fluence is shown to improve the stoichiometric transfer and decrease the lattice parameter. Simultaneous deposition from Nd:GGG and Ga_2O_3 targets produces film material that is richer in Ga compared to films deposited only from the Nd:GGG target. Film material deposited with higher fluences on the Ga_2O_3 target (and a corresponding lower fluence on the Nd:GGG target) is shown to have a lattice parameter that is smaller than the database value for stoichiometric GGG (samples 2 and 3). For fluences on the Nd:GGG and Ga_2O_3 targets of 1.5 and 2.5 J/cm^2, respectively, no diffraction peaks were observed from the film over the 2θ range from 10° to 80°, indicating the absence of any crystalline film growth.

Experiments were also conducted at lower oxygen pressures (samples 7 and 8) using Nd:GGG and Ga_2O_3 targets to investigate if a better film crystal quality would result. The gallium concentration in the films was considerably reduced by lowering the

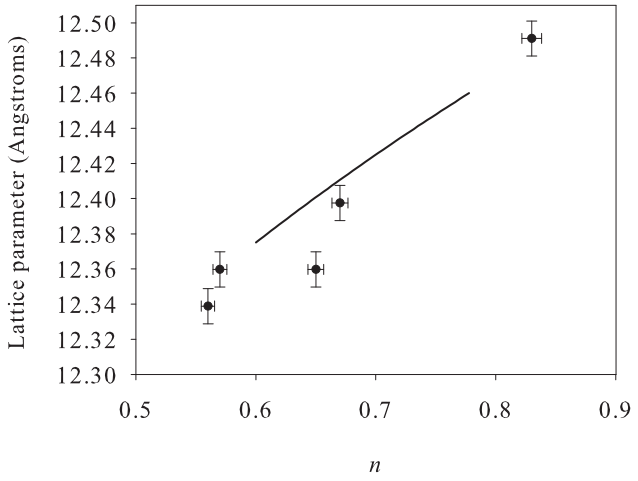

FIGURE 7.7: Calculated lattice parameter plotted against the measured film cationic ratio (n =Gd/Ga) (data from samples 2-6). The solid line corresponds to a fit to equation 7.3, where the cationic ratio (n =Gd/Ga) was determined from $n = (x + 3)/(5 - x)$. The error in the lattice parameter was determined from the error in the measured (400) GGG peak position. The error in the cationic ratio was determined from the accuracy of EDX measurements.

background pressure of oxygen. Films deposited under oxygen pressures of 4.0×10^{-2}, 4.4×10^{-3} and 2.4×10^{-4} mbar and similar fluences (samples 3, 7 and 8) on the Nd:GGG and Ga_2O_3 targets show a gradual reduction in the gallium concentration for lower pressures (see table 7.2). For the film grown with a pressure of 2.4×10^{-4} mbar (sample 8), no diffraction peaks were observed, and the film was amorphous. Reducing the background gas pressure from 4.0×10^{-2} mbar to 4.4×10^{-3} mbar, and depositing with a mixture of plumes from the Nd:GGG and Ga_2O_3 targets, resulted in a reduction of the (400) GGG peak position by roughly 1.0°. XRD analysis of films deposited under an oxygen pressure of 4.0×10^{-2} mbar to 4.4×10^{-3} mbar (samples 3 and 7) is shown in figure 7.8. This shift of peak position indicates a relatively large change in lattice parameter of around 0.4Å, a significant difference of ∼3% for GGG. Additionally, the peak full-width-half-maximum of films deposited at a pressure of 4.4×10^{-3} mbar was noticeably higher than that for a film deposited at a pressure of 4.0×10^{-2} mbar (0.17° compared to 0.07°), indicating a decrease in crystalline quality (i.e. an increase in disorder) and/or a significantly strained film. A notable point about these results is that, GGG has been fabricated with a deficiency of gadolinium atoms rather than gallium atoms (Gd/Ga = 0.56).

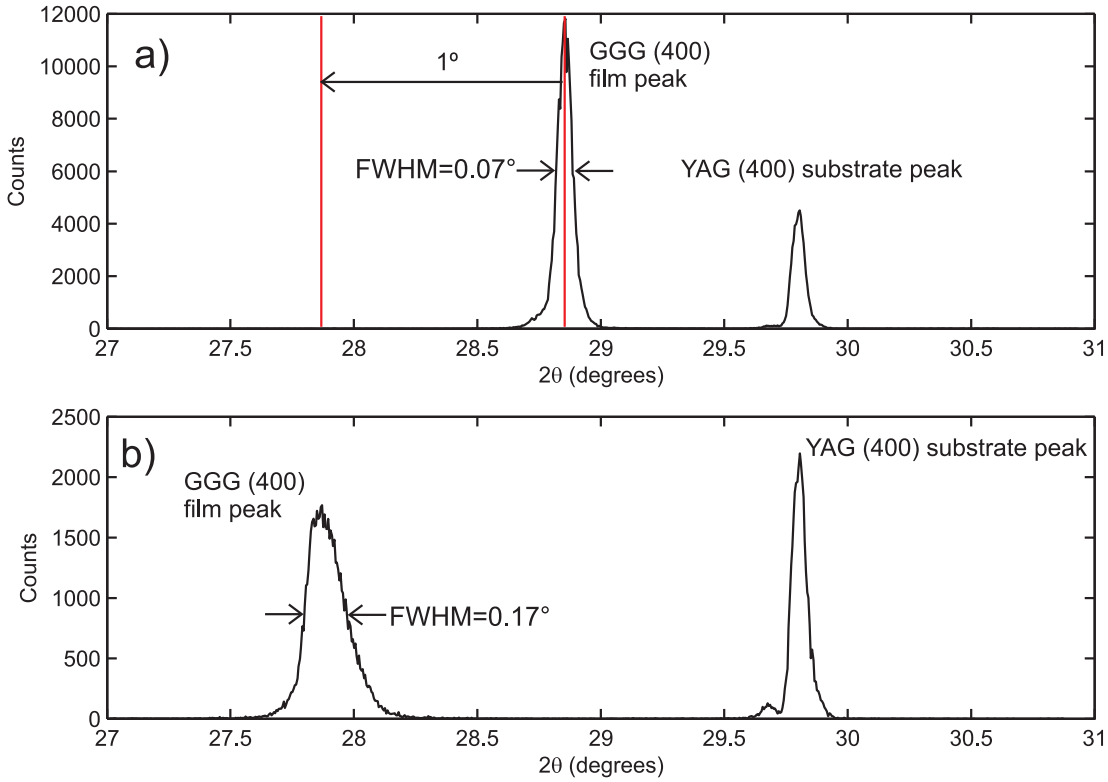

FIGURE 7.8: XRD spectra of films deposited with a mixture of Ga_2O_3 and GGG targets under oxygen pressure of a) 4.0×10^{-2} mbar (sample 3) and b) 4.4×10^{-3} mbar (sample 7).

All the films deposited with a mixture of Nd:GGG and Ga_2O_3 targets were shown to have a high density of particulates compared to those deposited with one Nd:GGG target only. Figure 7.9 shows a typical SEM micrograph of a film deposited with Nd:GGG and Ga_2O_3 targets (sample 3).

Smooth, solid-density targets are preferred for the production of films by PLD, since they generally result in fewer particulates on the surface of the films. Using a pure metal target to enrich the films is one option, but gallium metal has a low melting temperature (29.8℃) and would therefore need to be continuously cooled if it is to be used as a target. Many other garnets grown by PLD suffer from light-element deficiencies, such as GSGG and YAG (May-Smith & Eason 2007) and these may also be deposited by combinatorial PLD using the appropriate metal targets such as aluminum or scandium. However, one method to overcome the drawback associated with hot-pressed targets is to prevent the particulates from reaching the substrate by using the cross-beam PLD approach (Gorbunov et al. 1996).

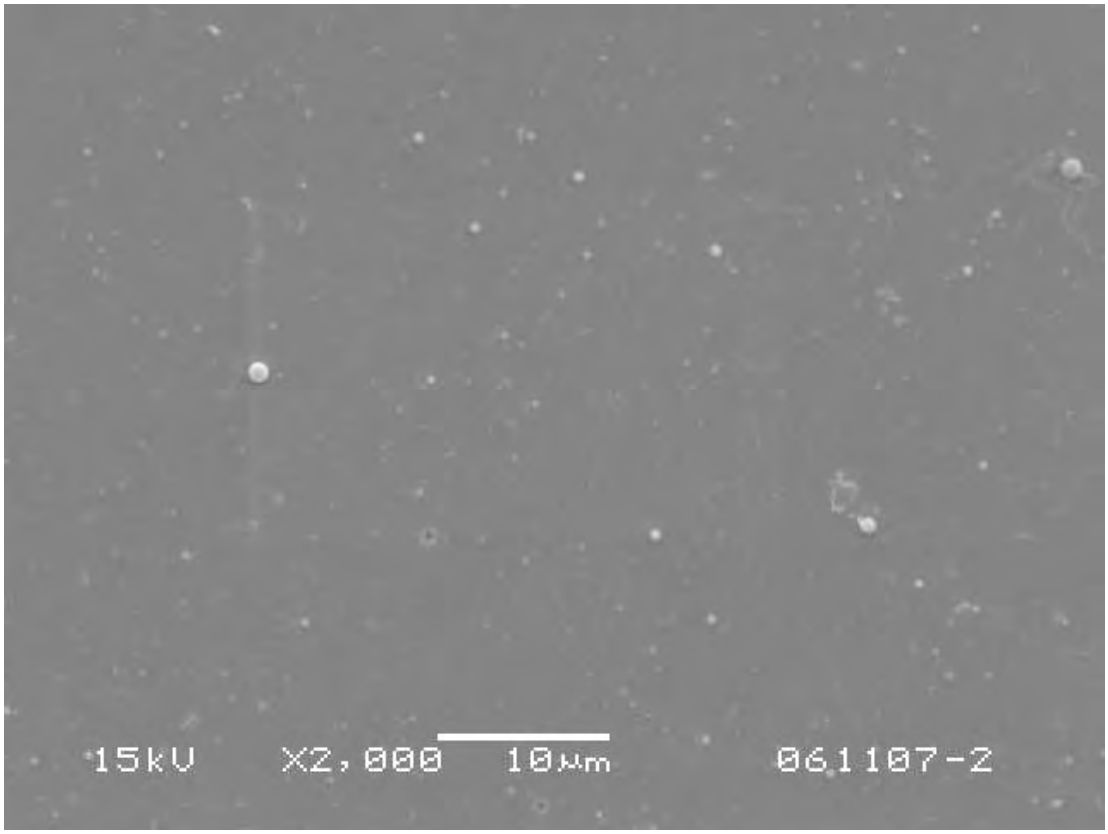

FIGURE 7.9: SEM micrograph of a film deposited with a mixture of Nd:GGG and Ga_2O_3 targets (film 3).

7.2.2 Deposition from Nd:GGG and YAG targets

Synchronised deposition from Nd:GGG and YAG targets onto a YAG substrate produced a film with an XRD spectrum with a typical (100) garnet orientation. Figure 7.10 shows an XRD spectrum from a film deposited with a fluence of $1.6\,\mathrm{J/cm^2}$ on both Nd:GGG and YAG targets under an oxygen pressure of 3.0×10^{-2} mbar, a target-substrate distance of 4 cm, a tilt angle of 36° and a CO_2 laser heating power of 6.3 W. The EDX compositional measurements of this film are shown in table 7.3 and an SEM micrograph of the film is shown in figure 7.11. The intensity of the film peaks was less intense compared to a film deposited with one Nd:GGG target with the same deposition conditions (see figure 7.12).

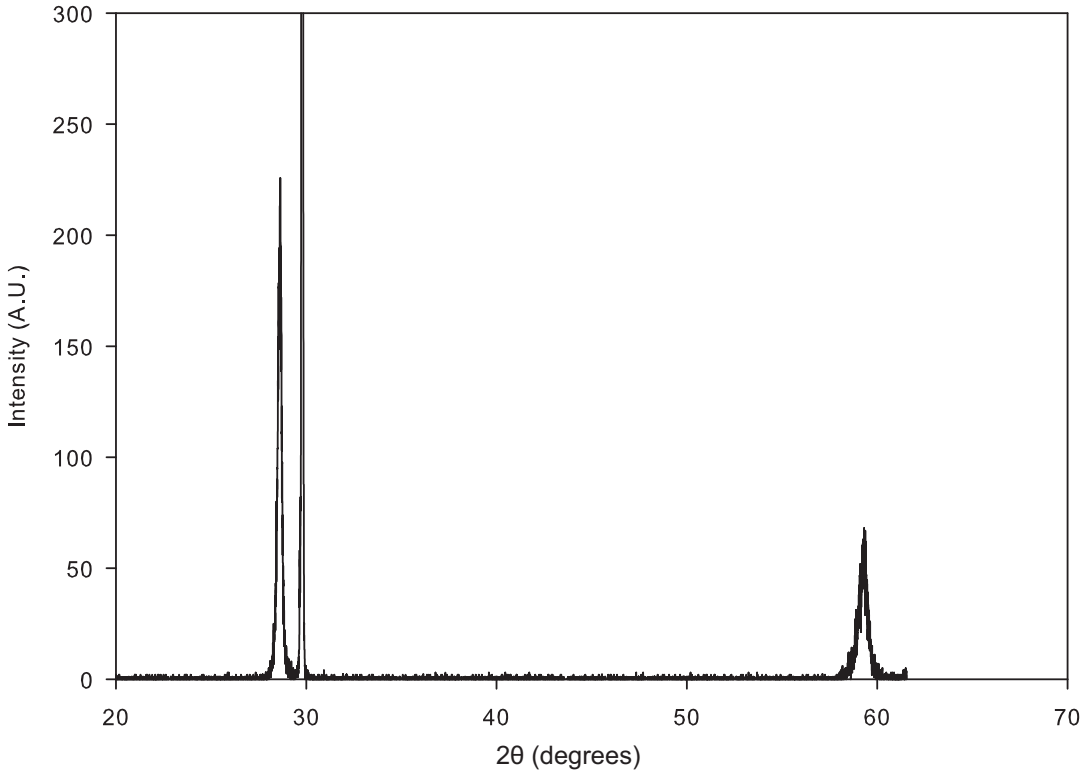

FIGURE 7.10: XRD spectrum from a film deposited onto a YAG substrate with a mixture of Nd:GGG and YAG targets. The inset shows the film peak in the 2θ range from 28 to 29°.

Element	Weight %	atomic %
O	19.42	58.40
Al	4.74	8.45
Ga	16.58	11.44
Y	15.20	8.22
Gd	44.06	13.48

TABLE 7.3: Measured composition of a sample deposited with a mixture of Nd:GGG and YAG targets.

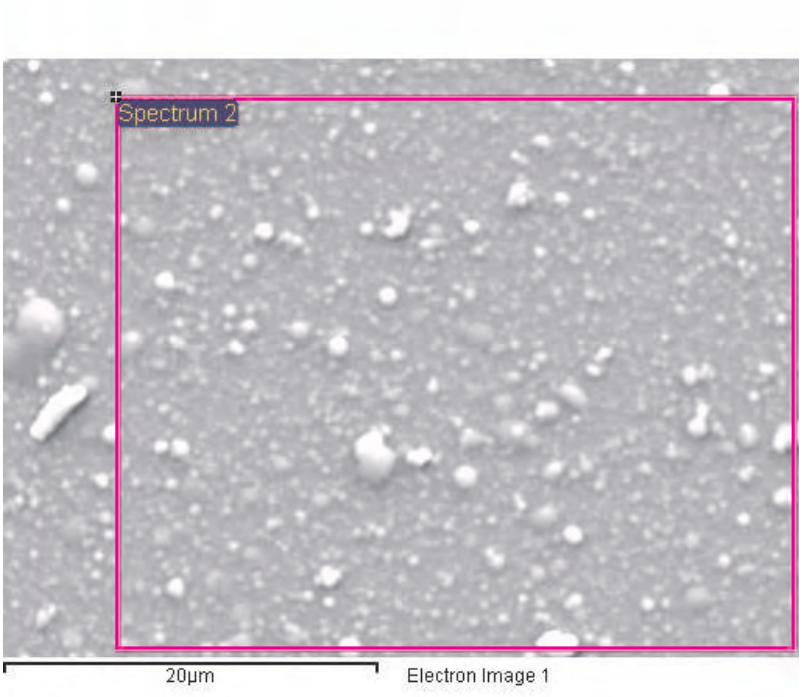

FIGURE 7.11: SEM micrograph of a film deposited onto YAG with a mixture of Nd:GGG and YAG targets. The composition of this sample was measured over the area encompassing the box labeled 'spectrum 2'.

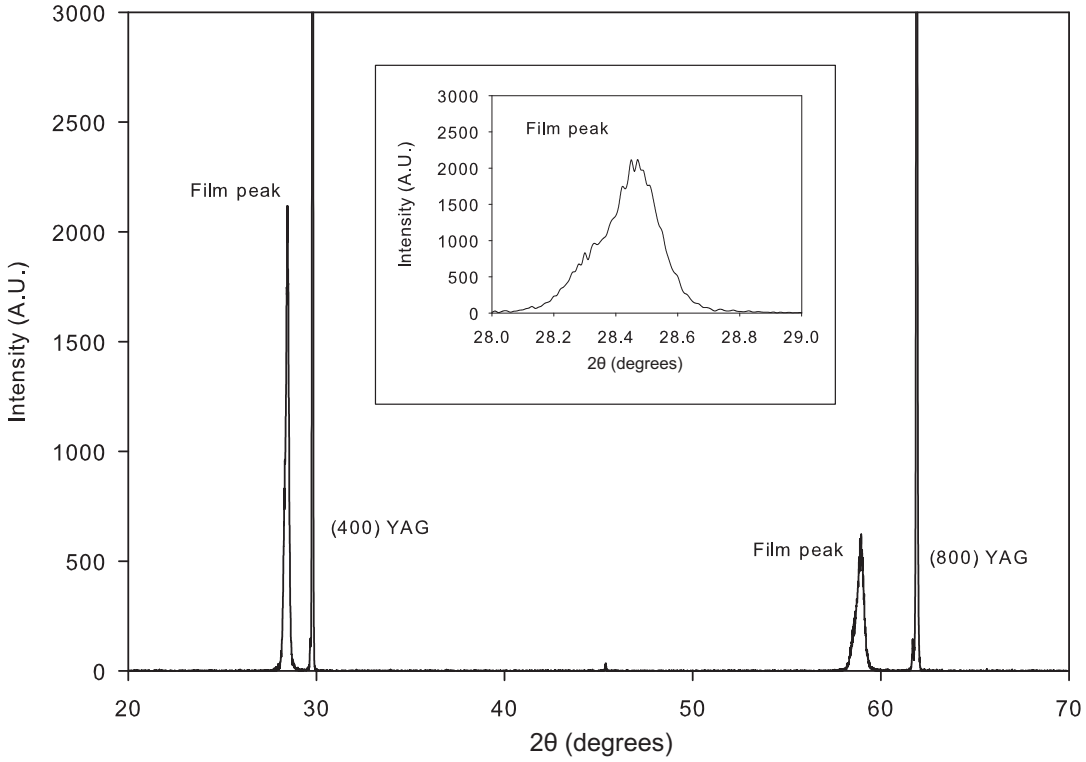

FIGURE 7.12: X-ray diffraction spectrum from a film deposited onto YAG with one Nd:GGG target. The inset shows the film peak in the 2θ range from 28 to 29°.

7.3 Conclusions

This chapter has presented experimental results on the growth of Nd:GGG using simultaneous deposition from two targets of Nd:GGG and Ga_2O_3. It has been shown that the gallium deficiencies previously observed in GGG films grown using conventional PLD can be compensated for by appropriately mixing the plasma plumes from the Nd:GGG and Ga_2O_3 targets. Compositions have been fabricated with a cationic ratio both above and below that of stoichiometric GGG (Gd/Ga ratio in the range 0.56 – 0.83, stoichiometric GGG Gd/Ga=0.60). The introduction of an increasing amount of gallium from a Ga_2O_3 target is shown to decrease the lattice parameter of the GGG film crystal and, for an optimum fluence used on the Ga_2O_3 target, make it equal to stoichiometric GGG. The lattice shifting from the database stoichiometric value is believed to occur due to a varying amount of Gd^{3+} occupying lattice sites that would usually be occupied by Ga^{3+}. For Ga concentrations above that of stoichiometric GGG, the lattice parameter continued to reduce. This is thought to be due to the occupation of some lattice sites normally occupied by Gd^{3+} by the excess Ga^{3+} and/or to the incorporation of the excess Ga in the lattice in the form of defects.

Chapter 8

PLD of $LiNbO_3$ onto silicon

This chapter[1] will present experimental results on the deposition of lithium niobate ($LiNbO_3$) onto silicon using a nanosecond eximer laser. A review of the recent efforts to create thin films of this material onto silicon is presented, and discussion is included on the potential methods that can be employed to overcome the inherent drawbacks that occur for the deposition of this material. The work presented in this chapter will demonstrate how non-stoichiometric transfer of the target material in the conventional PLD arrangement can be detrimental to the growth of high quality films for the specific case of lithium niobate.

8.1 Introduction

Lithium niobate is a ferroelectric oxide with large non-linear optical and electro-optic coefficients. It is used for optoelectronic and acousto-optic applications, which include waveguides, optical switches, modulators, second harmonic generators, and surface acoustic wave devices. To date, these devices are commonly implemented on single crystals, but thin films of this material can offer several potential advantages since they can be integrated into other device architectures. An innovative approach towards the development of lithium niobate-based thin film devices is the fabrication of such structures on silicon substrates in order to realise integration compatible with existing semiconductor technologies. The production of optoelectronic and micromechanical components on the same substrate will enable manipulation of optical signals using microelectronic control. Lithium niobate thin films can be used to control position using the piezoelectric effect,

[1]The work presented in this chapter was terminated due to loss of facilities and samples (located in the Mountbatten building).

and can be fabricated into pressure sensors, accelerometers and micro-pumps. For all the aforementioned commercial applications, it is necessary to grow this material with an epitaxial or well-oriented crystal phase in order to successfully utilise spontaneous polarisation, large electro-optic and piezoelectric coefficients of this material. One of the primary challenges of this research is to optimise the growth conditions in order to achieve device-quality films.

The deposition of lithium niobate onto silicon has posed a challenge for researchers mainly due to the fact that the lighter element, lithium, does not transfer well to the substrate. This problem may be overcome by implementing 'unconventional' PLD techniques, such as using of lithium-rich targets to compensate for the lithium deficiency, depositing in a high pressure environment in order to suppress the expansion of the lithium plume, or use combinatorial PLD in order to enrich the plume with deficient element.

8.2 Prior art

While lithium niobate has been epitaxially grown on sapphire, all previous attempts to grow lithium niobate films on silicon substrates have produced only poor crystalline quality films. There are many reports on the PLD of polycrystalline lithium niobate onto silicon (Chaos et al. 2001, Ghica et al. 1999, Wang et al. 2004), and highly textured growth has been achieved by using lithium-rich targets (Afonso et al. 1993) or mixed gas of O_2 and Ar (Ogale et al. 1992). Also, in-situ poling the growing film, highly-textured c-axis lithium niobate films have been made (Guo et al. 1998). The role of an applied electric field, in this case, is to align the spontaneous polarization of lithium niobate with the growing grains. One of the most comprehensive studies of the growth conditions of lithium niobate onto silicon, which investigated the composition and crystallinity as a function of gas environment, the laser energy density and the target-to-substrate distance, found that a gas pressure close to 1 mbar is required to produce stoichiometric films and lower pressures increased the presence of the Li-deficient phase, $LiNb_3O_8$. It was also found that the degree of c-axis orientation can be improved by increasing the laser energy density.

One of the main problems that occurs during the ablation process is the delayed release of lithium from the target. Experimental studies on the TOF of the lithium atoms in the plume found that lithium atoms are released $2 - 20\,\mu s$ after the laser pulse strikes

the surface (Chaos et al. 2000). Consequently, this delayed release means that there is almost no mixing with the other elements in the vapour phase, and higher pressures are required to compensate for the this effect. Also, theoretical models describing the expansion in a vacuum of the plasma produced from binary targets (Urbassek & Sibold 1993) predicts that the angular distribution of the lighter element species is broader. The ratio of lithium to niobium and oxygen, therefore, would not be representative of $LiNbO_3$ in the forward direction, and therefore lithium-deficient phases may occur for this reason. Clearly, methods need to be employed to overcome these drawbacks. The growth of lithium niobate onto silicon by PLD has had limited success, but various methods have been employed that resulted in preferentially polycrystalline films, such as:

- applying an electric field during deposition (Guo et al. 1998);
- using lithium-rich targets (Afonso et al. 1995);
- a mixture of Ar/O_2 background gases (Chaos et al. 2001).

A variety of other techniques have been used to deposit lithium niobate onto silicon, such as chemical beam epitaxy (Joshkin et al. 2000), polymeric precursor method (Bouquet et al. 1999) and sol-gel (Hur et al. 1994). These techniques still suffer from lithium-deficient phases and the films are poorly crystallised. However, a more promising technique based on crystal slicing and bonding, has recently been developed to produce sub-micron thin films of single-crystalline quality lithium niobate (Guarino et al. 2007). In this method, slicing of a layer of lithium niobate is performed by exposing the bulk sample to high-energy (195 keV) helium ions, which penetrate the sample and stop, rapidly losing most of their energy in lattice collisions. The high concentration of interstitial helium causes stress in the lattice and a thin slab is cleaved from the sample. The slice is then bonded to a substrate using an adhesive polymer, and structures can be fabricated using photolithographic techniques. This approach has been used to fabricate electro-optically tunable micro-ring resonators (Guarino et al. 2007).

8.3 Experimental set-up

A KrF excimer laser emitting at 248 nm with a pulse duration of ≈ 20 ns was used to ablate a single-crystal lithium niobate target. The laser beam was focused to a spot size

of $\sim 2 \times 4$ mm on the target at an angle of incidence of 45 degrees. A CO_2 laser with remote control scanning (galvanometric mirrors) was used to heat the silicon substrate. The computer-controlled mirrors were used to deflect the CO_2 laser across a 2D array of points (6×4) on the substrate as previously reported by Barrington & Eason (2000). The substrates were mounted on ceramic holders and a CCD camera was used to observe the distribution of a laser diode pointer coincident with the CO_2 beam path on the substrate. Before each experiment, the chamber was pumped down to a pressure of $\sim 10^{-5}$ mbar and the background gas was slowly introduced into the chamber until the desired pressure was reached.

The temperature was calibrated by recording the melting points of small ($\approx 1 \times 1$ mm) pieces of various metals foil attached to the top edge of the substrate. Samples of indium, tin, lead and aluminium were used in this experiment, and the melting of samples was observed using a CCD camera. Figure 8.1 shows a plot of the incident CO_2 laser power as a function of the observed melting points of various metals.

In order to control the heating rate of the substrate more accurately, an automatic power ramp for the CO_2 laser was introduced. The device consists of a stepper motor

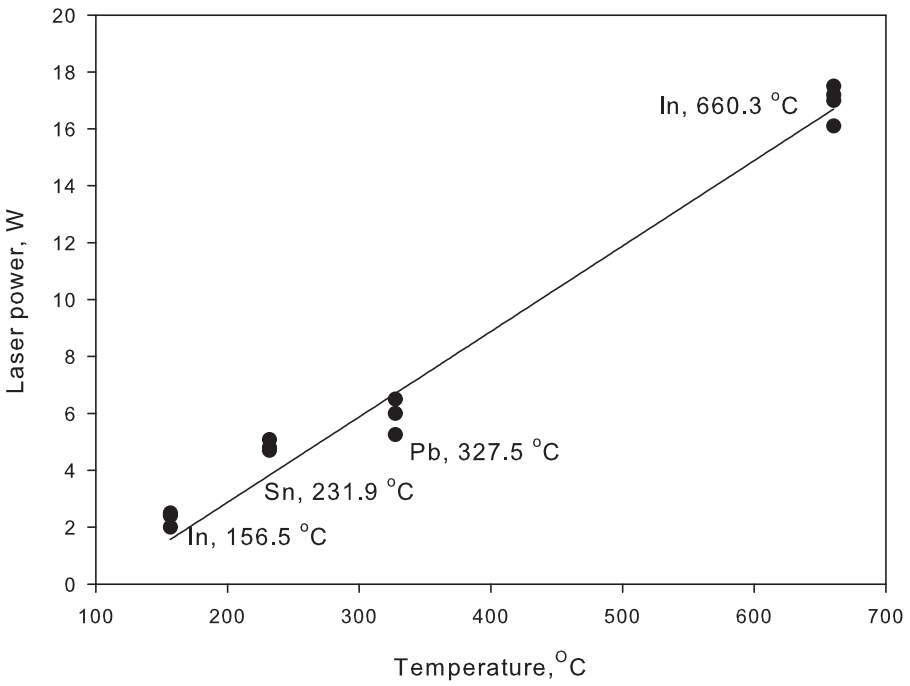

FIGURE 8.1: Temperature calibration curve of CO_2 laser-heated silicon substrates using the raster-scanning method of Barrington & Eason (2000).

attached to a potentiometer that would vary the voltage received by the laser. This device is capable of increasing CO_2 laser power 2.6-1000 mW per minute.

A remote controlled substrate blocker was used to allow pre-conditioning of the target before deposition. The films where grown on chemically cleaned silicon [100] (0.5 mm thick) and the native oxide layer (SiO_2) was removed by exposing the substrate to hydrofluoric acid and ammonium fluoride (silicon dioxide etchent 7:1) a few minutes before each experiment. After deposition the substrate was cooled at a rate of $\sim$ 10°C per minutes. The target was a single-crystal 2 mm think $LiNbO_3$ wafer grown by the Czocchralski method. The experimental set-up used for PLD growth of lithium niobate films is shown in figure 8.2

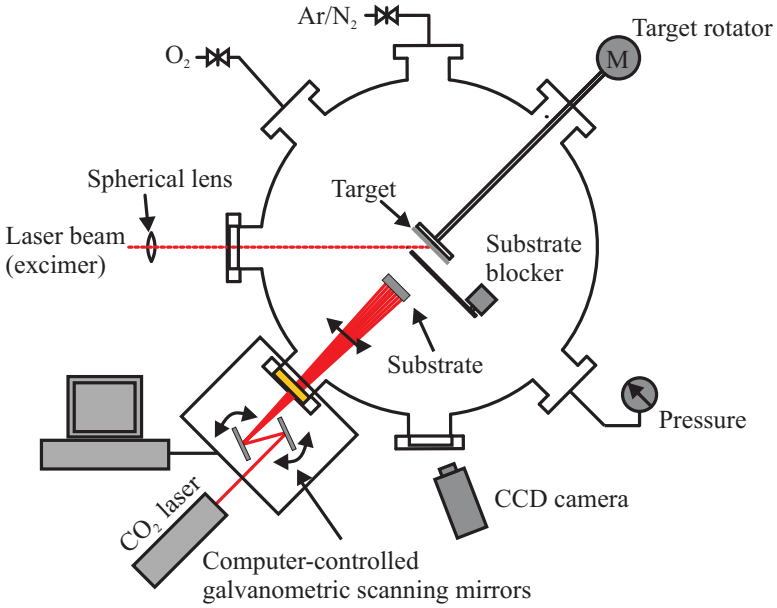

FIGURE 8.2: Experimental set-up used for nanosecond (excimer $\lambda = 244$ nm) PLD of lithium niobate onto silicon.

8.4 Results

Lithium niobate was deposited onto silicon under various conditions and the films were analysed by X-ray diffraction. Table 8.4 shows a list of deposition conditions for films deposited at a temperature of roughly 600°C (incident CO_2 laser power of 15 W).

Films were deposited at room temperature, 400°C (9 W) and 600°C (15 W), and at a temperature of 400°C or less films were found to be amorphous. All of the films deposited at 600 °C (films $1-8$) were polycrystalline. Figure 8.3 shows an XRD spectrum of a

Film	Pressure (mbar)	Distance (cm)	Fluence (J/cm^2)	Angle* (deg.)
1	1	3	1.5	0
2	1	4	1.5	0
3	1	5	1.5	0
4	0.1	3	1.5	0
5	0.1	5	1.5	0
6	0.1	2	1.6	10
7	0.1	2	1.6	22
8	0.1	2	1.6	54
9	0.1	2	1.6	70

TABLE 8.1: Deposition conditions for PLD of lithium niobate onto silicon. The substrate temperature was 600℃ and the duration was 30 minutes (films 1-5) and 1 hour (films 6-9). *This angle corresponds to the angle between the normal of the target and line from the ablation spot to the centre of the substrate.

lithium niobate film ($2.5 - 3.0\,\mu$m thick) grown at 1 mbar (film 1), plotted on the same graph is a spectrum corresponding to bulk lithium niobate (Nakanishi et al. 2006).

The XRD spectra of films deposited at an oxygen pressure of 0.1 mbar (films $4 - 7$) revealed the possible presence of the lithium-deficient phases ($LiNb_3O_8$). Figure 8.4 shows an XRD spectrum of a lithium niobate film deposited at a pressure of 0.1 mbar (film 4). A peak was identified at 30 degrees, which may correspond to the (202) $LiNb_3O_8$ plane. The XRD spectrum in this case was noticeably weaker, compared to the XRD scan of a film deposited at a higher pressure of 1 mbar. Figure 8.5 shows XRD spectra of films deposited at various target-substrate distances of 3, 4, and 5 cm. These results reveal the need for closer target substrate distances at these high pressures.

Lithium niobate was grown at large off-axis angles to investigate whether improved growth could be achieved (films 6-9). The temperature was kept at 600℃ for all depositions. The appearance of the films was very non-uniform, with interference fringes visible on the outer edges (film 7 and 8) and an opaque region on the opposite edge. The XRD analysis revealed that most of the films grown where polycrystalline, with the existence of preferential c-axis growth in one of the films (Film 8). Figure 8.6 shows an X-ray diffraction spectrum of a film (700 nm thick at the edge) grown at an angular deviation of 54 degrees and a distance of 2 cm (film 8). The peak at 33° could not be identified as a known phase. The peak corresponding to the (006) plane is more intense than the (012) and (110) planes, which suggests that this film is preferentially orientated along the (001) plane.

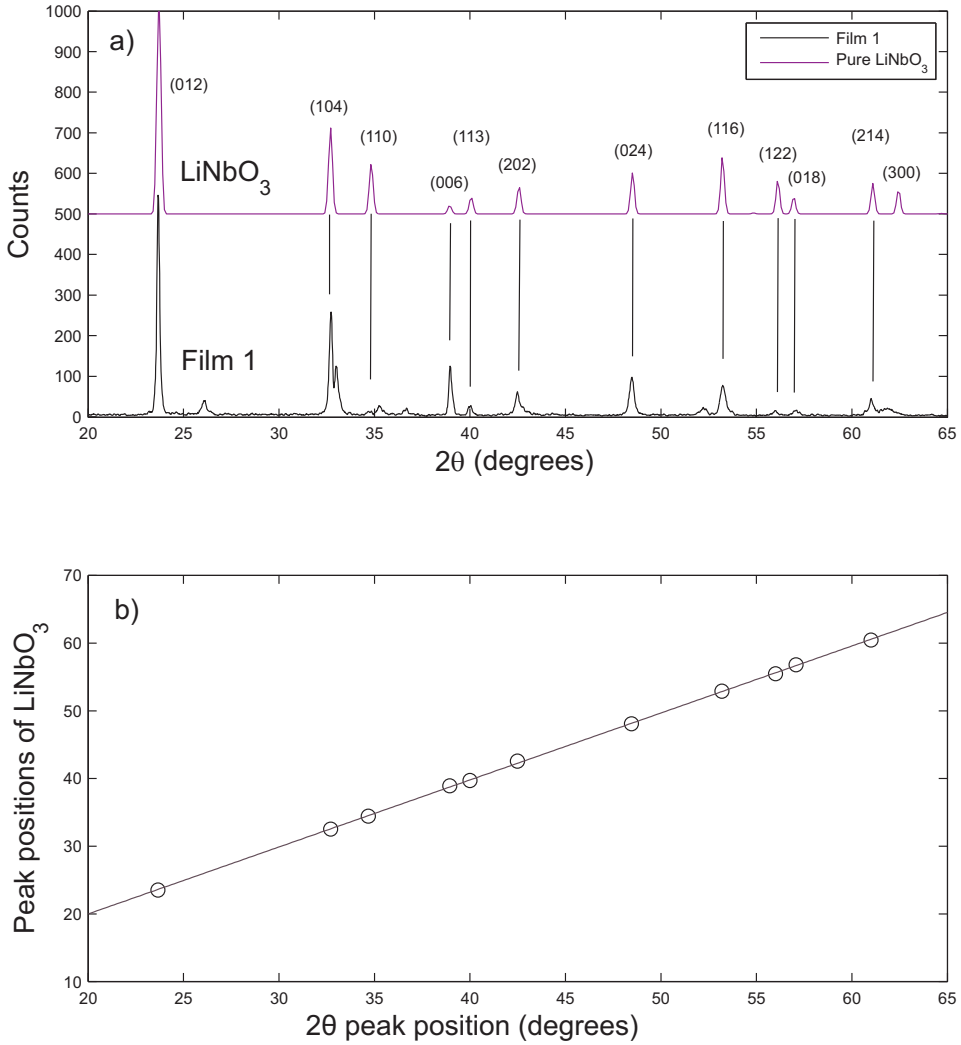

FIGURE 8.3: a) XRD spectrum of a lithium niobate film deposited onto silicon at an oxygen pressure of 1 mbar (film 1). Plotted on the same graph is an XRD spectrum of polycrystalline $LiNbO_3$ (the spectrum is off-set on the intensity axis for clarity) (Nakanishi et al. 2006). b) 2θ peak positions detected from film 1 plotted against peak positions for polycrystalline $LiNbO_3$.

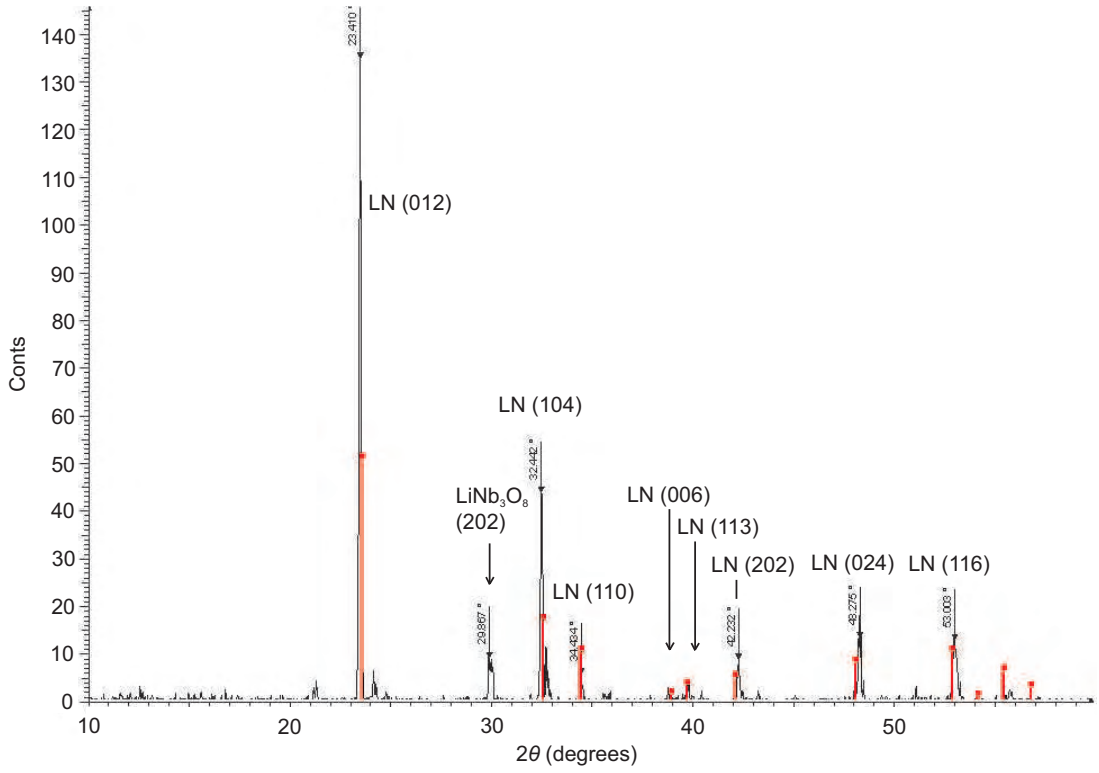

FIGURE 8.4: XRD scan of a polycrystalline lithium niobate film deposited onto silicon under an oxygen pressure of 0.1 mbar (film 4). The $LiNbO_3$ peaks (LN in figure) have been identified. Note the possible presence of the lithium deficient phase $LiNb_3O_8$.

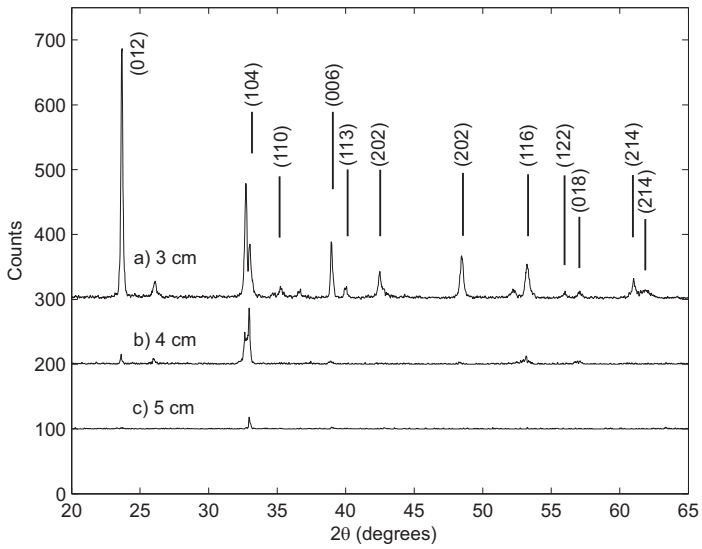

FIGURE 8.5: XRD spectra of lithium niobate deposited onto silicon at various target substrate distances of a) 3 cm, b) 4 cm and c) 5 cm (films 1-3). The $LiNbO_3$ peaks have been identified.

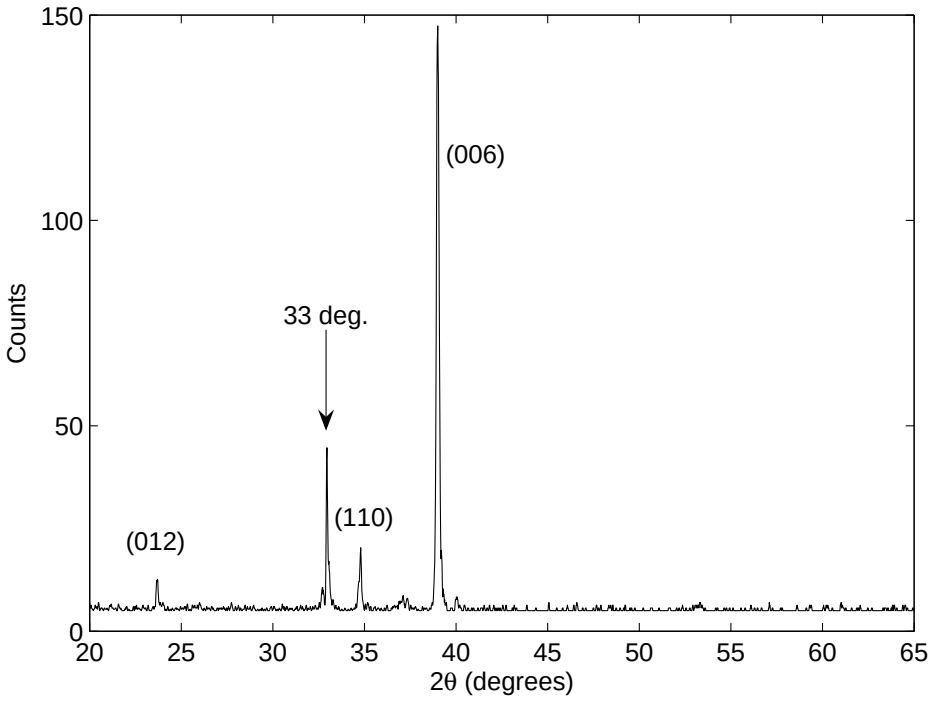

FIGURE 8.6: XRD spectrum of a film grown at an off-axis angle of 54 degrees (relative to the normal of the target) (film 8).

8.5 Conclusion

This chapter has presented experimental results on the deposition of lithium niobate onto silicon. XRD evidence shows that the films consist of polycrystalline lithium niobate and other phases that could not be identified. Films have been deposited under various growth conditions of pressure, distance and off-axis angles. It has been found that an oxygen pressure of 1 mbar is preferred for the growth of the lithium niobate phase, and at pressures of 0.1 mbar the peaks corresponding to the lithium niobate phase are noticeably less intense. The XRD spectrum from a film deposited at off-axis geometries shows that the (006) peak is more intense than the other orientations, suggesting that this film is preferentially orientated in the (001) plane.

For realisation of device-quality lithium niobate film onto silicon there is a need to overcome the shortcoming of PLD for this material, namely the non-stoichiometric transfer of the target material. The main problem is that the lighter element lithium is not transferred effectively to the substrate, either because of its delayed release from the target (Chaos et al. 2000), or its broader angular distribution in the plasma-plume. This leads to the formation of light-element deficient films. Research shows that stoichiometric films can be deposited by either using a mixture of Ar and O_2 (Chaos et al. 2001) gases or by using lithium-rich targets (Afonso et al. 1995), however the films remain polycrystalline and to utilise the electro-optic properties epitaxial or textured films are required. Combinatorial PLD could also be used to overcome this drawback. Deposition for two targets of Lithium niobate and lithium oxide may lead to films with a stoichiometry closer to bulk lithium niobate.

Chapter 9

Conclusions

This thesis has reported on two novel PLD techniques with the intension of increasing the capability of this technology. The following sections will review some on the important results and discuss future directions of femtosecond and combinatorial PLD.

9.1 Femtosecond PLD

This thesis has shown that femtosecond PLD is a variable method of fabricating thin films of highly textured Nd:GGG films. Experiments have been conducted using a Ti:sapphire femtosecond laser operating at a wavelength of 800 nm and a pulse duration of 130 fs. Film properties have been studied systematically for a range of deposition parameters of laser fluence, laser spot-size, target-substrate distance, background pressure. It was found that relatively high oxygen pressure (0.1 mbar) were required for films to grow in the desired phase ($Gd_3Ga_5O_{12}$). The films under a range of depostion parameters were shown to have a relatively poor surface morphology, and AFM and SEM analysis confirms the films are covered with particulates upto roughly 1 µm in diameter. A comparison between the ion velocities produced by nanosecond and femtosecond laser ablation of the Nd:GGG target material indicate a large difference in the plasma characteristics. Evidence shows that the peak TOF of the femtosecond laser-ablated ions can be up to eight times faster than the nanosecond case for similar fluences. It is possible that higher background pressure is necessary to reduce the adverse effect fast ions can have on the growing film (such as sputtering). Evidence also shows that the TOF of the femtosecond laser ablated ions has a distinctively non-maxwellian velocity

distribution, and in some conditions a dual-peak characteristic was observed, possibly indicating non-thermal ablation mechanisms.

The presence of particulates can have a detrimental effect on the quality of thin films grown by PLD, especially those used for optical applications where scattering losses should ideally be minimal. However, the generation of nanoparticles, fragments or clusters seems to be an inherent feature of ultrashort PLD and ablation. Many of the reports detailing PLD in the ultrashort regime show that the surfaces of the films often have a very poor quality, and the phenonemon of nanoparticle production from ultrashort laser ablation has recently been reported for a range of materials (Albert et al. 2003, Liu et al. 2007, Noël et al. 2007). These experimental studies show that femtosecond ablation of metals in vacuum leads to a plume that is composed of an atomic and ion component, and a nanoparticle component. For the case of the ablation of titanium (Albert et al. 2003), Coulomb explosion leads to highly energetic ions, which are followed by atomic neutrals, then a slower plume component consisting of nanoparticles of the target material. The sizes of these particles have been found to range up to roughly 100 nm diameter, and some evidence shows that they can be crystalline (Liu et al. 2007, Tull et al. 2006). The particulates observed on the surface of Nd:GGG films deposited by femtosecond PLD, reported in this thesis, have been found to range up to roughly 1 µm in size. It is possible that nanoparticles from the ablation process have coalesced into larger particulates due to the presence of a background gas. The quasi-spherical shapes of the particulates observed on the surface of the films suggests that they may have formed from a molten or vapour phase. The highly textured nature of the GGG films also indicates that they are not likely to be crystalline before arriving at the substrate.

9.2 Combinatorial PLD

Combinatorial PLD has shown to be a promising technique for controlling the composition of the deposited films. This thesis has shown that by simultaneously depositing from two targets of Nd:GGG and Ga_2O_3, the composition of the resultant films can be controlled by changing the relative fluences on two targets. Nd:GGG films have been deposited with a Gd/Ga ratio that is both above and below that of stoichiometric GGG. The introduction of an increasing amount of gallium from a Ga_2O_3 target is shown to decrease the lattice parameter of the GGG film, which is in agreement with empirical formulas based on the ionic radii and the concentrations of the constituent atoms.

In other areas, the combinatorial PLD approach may provide unique capability for the fabrication of sophisticated thin film architectures and unique film compositions. For example, by using three target that are the same composition, it is possible to deposit more uniform films over a larger area. The cross-beam PLD arrangement could be used with three targets to illuminate particulate contamination. This arrangement has only used two targets to date.

By using three plumes that are of a different composition, a range of potential novel devices are possible. New mixed material, engineered from three different starting materials. For example, new garnets that have not been made via conventional Czochralski method could be fabricated from three different metal oxides:

$$X_3Y_2Z_3O_{12} = 1.5(X_2O_3) + (Y_2O_3) + 1.5(Z_2O_3)$$
$$X, Y, Z = \text{chosen cation}$$

Layered structures are also possible by sequential deposition of different materials. This could be used to fabricate cladding-pumped planar waveguides. Graded transitions between two garnets is possible by gradually varying the mixing ratio for two or more targets.

One of the applications for garnets is the minimisation of the lattice mismatch by choosing a film stoichiometry that has the appropriate lattice parameter for a given substrate. As has been shown in this thesis, the sizes of the constituent ions in the crystal can have a pronounced influence the lattice parameter. This leads to the opportunity of using combinatorial PLD to substitute ions of different sizes into the crystal structure that has an effect of more closely matching the chosen material to the substrate's lattice parameter. This can either take the form of an intermediate buffer layer between the film and substrate or direct modification of the film lattice parameter by changing its composition.

Appendix A

Three dimensional heat diffusion modelling

This appendix will describe the thermal modelling of the CO_2 laser heating of substrates using a ZnSe tetra-prism. This theoretical model is supplementary to the work presented in chapter 4 and was undertaken by A. Muir (ORC).

Finite element modelling was used to construct a three-dimensional (3D) computer model describing the heat flow in a YAG substrate (10 mm × 10 mm × 0.5 mm) that results from CO_2 laser heating with various different source intensity distributions. The heat flow within the substrate is governed by the heat diffusion equation in the steady state,

$$-\nabla\left(k\nabla T\right) = Q, \tag{A.1}$$

where k is the thermal conductivity of YAG, which is $k = 3.4\,\mathrm{Wm^{-1}K^{-1}}$ at 1073 K (Padture & Klemens 1997), T the temperature and Q is the heat source function. When the thermal conductivity is not temperature dependent this can be written as,

$$-k\nabla^2 T = Q. \tag{A.2}$$

Since the substrates are heated in vacuum, it can be assumed that heat loss at the substrate surfaces is due only to radiative emission. This gives the nonlinear boundary equations for the model:

$$\mathbf{n}\cdot\left(k\nabla T\right) = \epsilon\sigma\left(T_{amb}^4 - T^4\right) \tag{A.3}$$

where $\mathbf{n}$ is a unit vector directed with the inward normal to the surface, ϵ is the emissivity of the substrate, σ is the Stefan-Boltzmann constant, and T_{amb} is the ambient temperature around the substrate (293 K). Emissivity is not well documented for YAG at high temperatures so the value above was estimated from a separate calibration of

temperature involving the melting of thin, high purity metal foils on a YAG substrate, which resulted in an estimate of emissivity of 0.45.

Untransformed Gaussian

To illustrate the need for using any form of beam homogenization device, the temperature distributions produced by an untransformed Gaussian beam have been calculated for a range of beam waists. In this case, the heat source function is given by

$$Q = \delta(z)\frac{2P}{\pi w^2}\exp\left[-2\frac{x^2+y^2}{w^2}\right], \tag{A.4}$$

where P is the power of the incident laser beam, w is the beam waist, x, y and z are Cartesian axes. It has been assumed that the optical absorption is a delta function, since the absorption depth is much less than the substrate thicknesses (the skin depth of the YAG substrate illuminated with 10.6 µm light is roughly 50 µm, assuming an absorption coefficient of 200 cm^{-1} (Slack et al. 1969)). The investigation has been limited to beam waists up to half the width of the substrate (5 mm) because beam waists larger than this are not practical, since they would result in significant wastage of radiation and heating of the chamber and other chamber parts. As an example, the amount of beam wastage with a waist of 5.0 mm is 4.4%.

A minimum standard deviation of 43 K was found to occur for a beam waist of 5.0 mm and a power of 5.6 W with a corresponding mean temperature of 978 K and a temperature range of 173 K. A profile of the untransformed Gaussian source function is shown in figure A.1(a) and the corresponding temperature profile on the deposition face of a YAG substrate is shown in figure A.1(b). It can be seen in figure A.1(b) that most of the substrate surface is at a temperature more than 50 K below that of the substrate center. Such an inhomogeneous temperature distribution would result in severely reduced quality crystal growth in the cooler areas and would not be acceptable for use in PLD experiments. This clearly indicates the requirement for a beam homogenisation technique if a CO_2 laser is to be successfully used as a heat source.

Raster-scanned Gaussian

To compare the operation of the tetra-prism to a raster-scanned Gaussian beam, a grid of 6×6 scanning points spaced evenly across the substrate surface was used. Rather

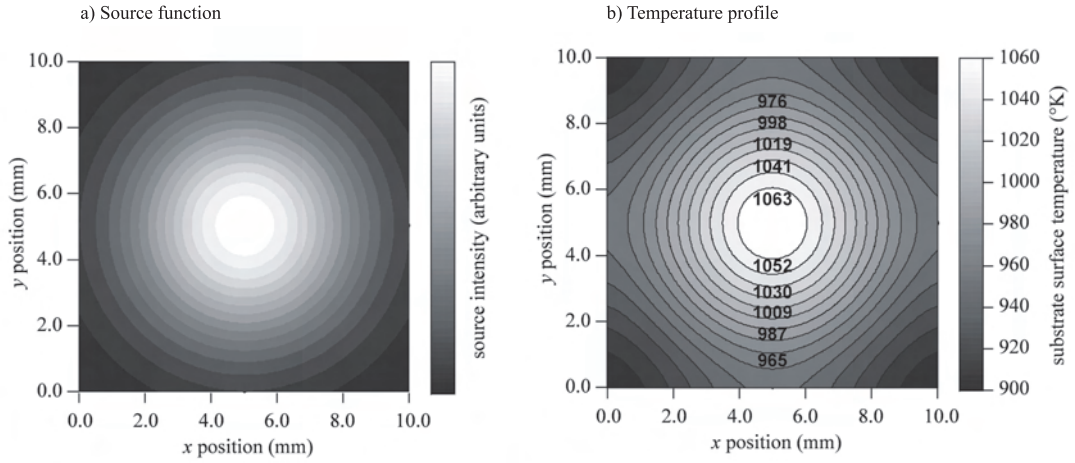

FIGURE A.1: a) Untransformed Gaussian source function with a beam waist of 5 mm and power of 5.6 W and b) the corresponding temperature profile on the deposition face of a YAG substrate.

than model the high speed movement of one beam across the substrate, it is possible to approximate the process by dividing the laser power into the grid points and making them constant in time. This approximation is valid when the scan speed is fast (< 100 ms to scan one complete cycle, which is faster than the thermal diffusion time in YAG) and the grid point dwell time is significantly longer than the transit time of the beam between grid points. In this case, the source function can be built without coherence effects because there is only one laser beam and one spot at any one time. The source can be described by

$$\begin{aligned} Q = \frac{2P}{36\pi w^2} \sum_{i,j=1}^{3} \Bigg[& \exp\left(-\frac{2}{w^2}\left([x+(i-0.5)d]^2 + [y+(j-0.5)d]^2\right)\right) \\ & + \exp\left(-\frac{2}{w^2}\left([x+(i-0.5)d]^2 + [y-(j-0.5)d]^2\right)\right) \\ & + \exp\left(-\frac{2}{w^2}\left([x-(i-0.5)d]^2 + [y+(j-0.5)d]^2\right)\right) \\ & + \exp\left(-\frac{2}{w^2}\left([x-(i-0.5)d]^2 + [y+(j-0.5)d]^2\right)\right)\Bigg] \end{aligned} \tag{A.5}$$

where d is the separation between neighboring scanning points along the x and y axes and i and j are indices to be summed over.

The range of beam waists used for this analysis was 1.0 mm $<$ w $<$ 3.5 mm and the scanning point separation was varied from 1.0 mm$< d < d_{max}$, where d_{max} was chosen such that the outermost scanning point was a distance w from the substrate. The minimum standard deviation of the temperature profile of the deposition face of the substrate was found to be 14 K for $w = 1.0$ mm and $d = 1.6$ mm with an incident

power of 6.9 W. The heat source profile used is shown in figure A.2(a) and the resultant substrate deposition face temperature distribution is shown in figure A.2(b).

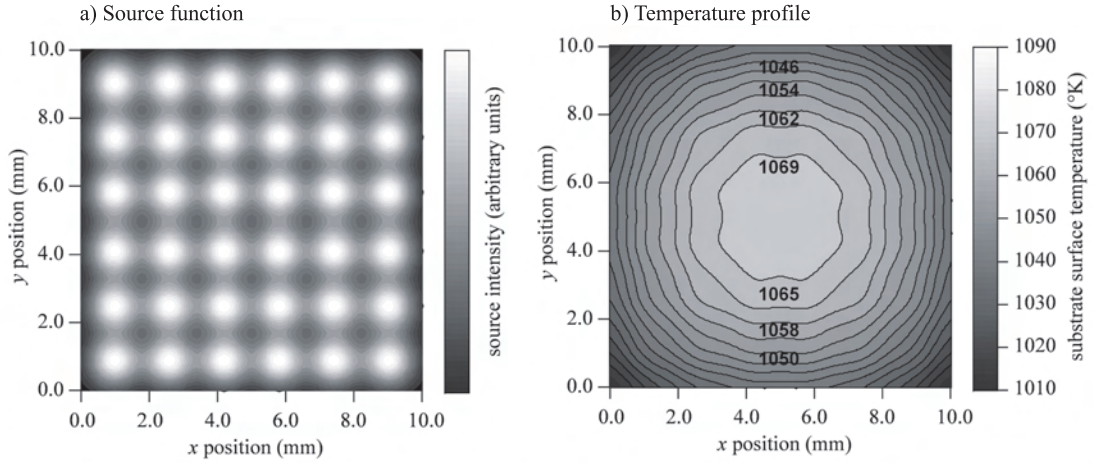

FIGURE A.2: a) Raster-scanned beam source function with $w = 1.0\,\text{mm}$, $d = 1.6\,\text{mm}$ and $P = 6.9\,\text{W}$, and b) corresponding temperature profile on the deposition face of a YAG substrate.

As can be seen from figure A.2, the homogeneity of the temperature profile is a clear improvement on the untransformed Gaussian case. However, there are still regions at the corners of the substrate where the temperature is noticeable lower (up to 80 K) than the centre of the substrate. For the raster scanning method to be improved further, the scanning points at the edges would have to be set closer to and perhaps even overlap the edges of the substrate to enable the intensity there to be increased. Another method of tuning the temperature distribution with the raster scanned approach, would be to increase the dwell time for scanning points around the outside of the heated square. This would allow the average intensity at the edges to be increased without leading to a decrease in power efficiency.

Recombined Gaussian

The heat source function obtained from the addition of four incoherent beam quadrants is now considered as an initial assessment of the heating profile produced by the tetra-prism. The heat source function was obtained from the superposition of four appropriately truncated Gaussians. To investigate the effect of changing working distance, D, for a fixed tetra-prism angle (θ=1°), a quadrant separation parameter a was introduced. The source function is then given by

$$Q = \frac{2P}{\pi w^2}\left(A_1 + A_2 + A_3 + A_4\right) \tag{A.6}$$

where,

$$A_1 = \exp\left(-\frac{2}{w^2}\left[(x+a)^2 + (y+a)^2\right]\right), \quad \text{for } x > -a,\, y > -a \tag{A.7}$$

$$A_2 = \exp\left(-\frac{2}{w^2}\left[(x+a)^2 + (y-a)^2\right]\right), \quad \text{for } x > -a,\, y < a \tag{A.8}$$

$$A_3 = \exp\left(-\frac{2}{w^2}\left[(x-a)^2 + (y+a)^2\right]\right), \quad \text{for } x < a,\, y > -a \tag{A.9}$$

$$A_4 = \exp\left(-\frac{2}{w^2}\left[(x-a)^2 + (y-a)^2\right]\right), \quad \text{for } x < a,\, y < a \tag{A.10}$$

The parameter range 3.0 mm< a <5.0 mm and 1.0mm < w < 10.0mm was modeled over to achieve a combination that results in the most homogeneous temperature distribution. A minimum standard deviation of 2.7 K was found to occur for $a = 5.0$ mm and $w = 7.7$ mm using a power of 7.7 W. The mean temperature obtained with these parameters was 1076 K and the temperature range was 16 K. A profile of the source function generated by the above parameters is shown in figure A.3(a) and the temperature distribution on the deposition face of a YAG substrate is shown in figure A.3(b). It is

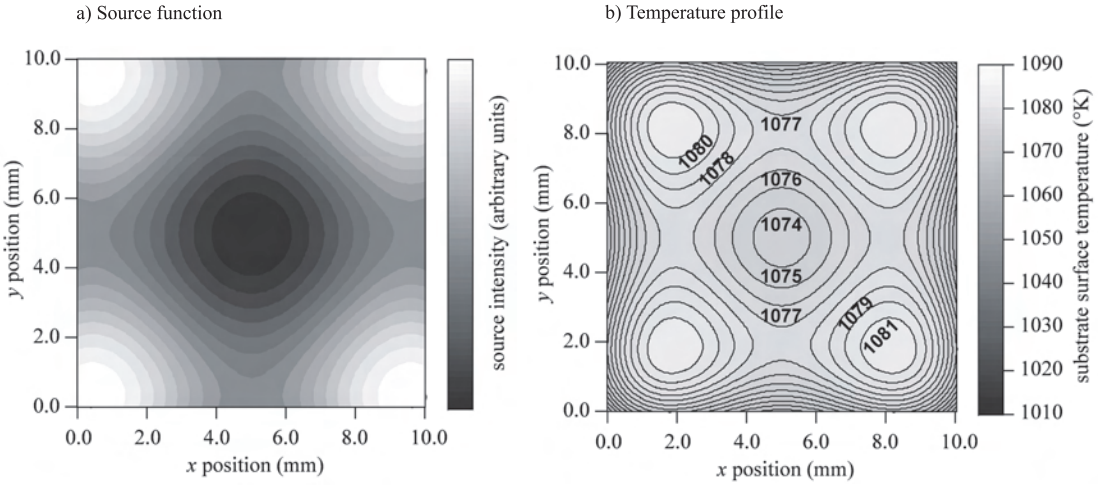

FIGURE A.3: a) Recombined incoherent Gaussian beam source function with w = 7.7 mm, $d = 5.0$ mm, and $P = 11.0$ W, and b) corresponding temperature profile on the deposition face of a YAG substrate.

interesting to note from figure A.3(a) that in contrast to the source functions produced by the previous methods, the parameters above do not produce the flattest average intensity source function possible, which would occur for slightly different parameters ($a = 5.0$ mm and $w = 9.6$ mm). However, this slightly inhomogeneous heating profile

does result in the most homogeneous temperature distribution. This is because above average heat supplied at and near the substrate edges compensates for the higher rate of radiative emission from these areas because of the larger surface area to volume ratio. This highlights the fact that the goal of a square heating beam homogeniser is not to produce a perfectly flat intensity square beam, but rather an overall flat intensity beam with an increased level of heat at the corners and around the edges. This is the key to the success of the tetra-prism design, which enables the level of increased intensity at the substrate edges to be controlled without the consequence of reduced efficiency. The temperature distribution shown in figure A.3(b) clearly illustrates the improvement in homogeneity over the untransformed Gaussian case. Such a homogeneous temperature distribution is ideal for PLD experiments and the remaining challenge is for the tetra-prism to reproduce a similar degree of homogeneity despite the diffraction and interference effects that apply in the real-world case.

Recombined Gaussian with Fresnel diffraction

Fresnel diffraction will produce a larger periodic modulation of intensity than interference for the tetra-prism setup under consideration (1.7 mm compared to 0.430 mm) and will therefore be the dominant factor in determining the substrate temperature inhomogeneity, allowing the source intensity modulation due to interference to be neglected here for simplicity.

To calculate the source function from a recombined Gaussian with Fresnel diffraction, a single quadrant of a Gaussian E-field was considered and then propagated in free space using Fourier optics methods. The independence of the diffraction of each quadrant from the others then allowed the result for the initial single quadrant to be rotated to give the pattern produced by the other three quadrants. The four resultant E-field distributions could then be summed to build the complete source function.

The Fresnel diffraction was seen to have a few noticeable effects on the heat source compared to the incoherent function analyzed in the previous section. An intensity modulation in both the x and y directions was introduced with a period variable at the millimeter scale length and the effective edge of the source was softened and moved toward the center of the substrate.

The recombined beam quadrant parameters were varied to find the parameters that produce the most homogeneous substrate temperature distribution. The minimum standard deviation of 2.2 K in this case was found to occur with $a = 5.6\,\text{mm}$ and $w = 9.5\,\text{mm}$ with a power of 9.5 W. The mean temperature was found to be 1076 K and the temperature range was 14 K. Figure A.4(a) shows the source function for these parameters and figure A.4(b) shows the resultant temperature distribution on the deposition face of a YAG substrate.

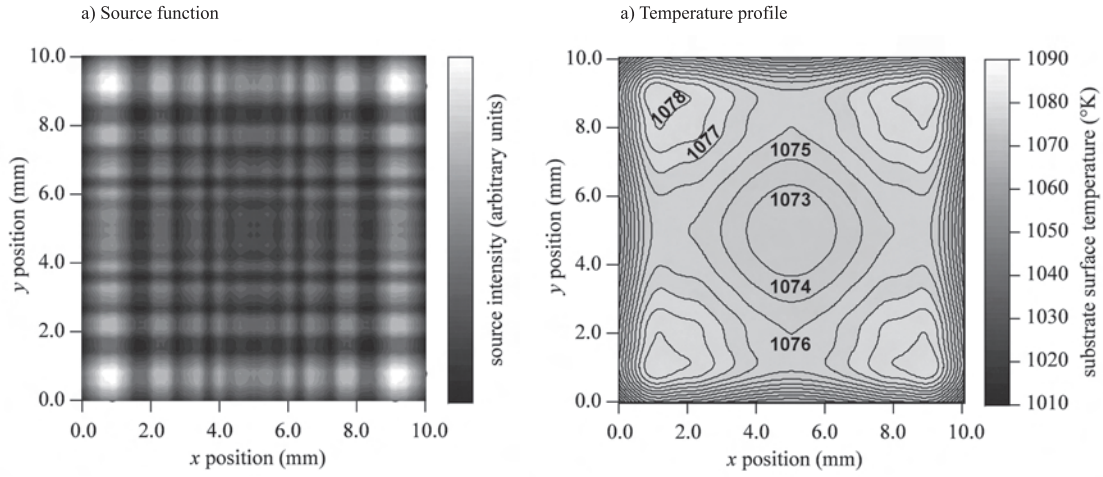

FIGURE A.4: a) Source function of a recombined Gaussian with Fresnel diffraction with $w = 9.5\,\text{mm}$, $d = 5.6\,\text{mm}$, and $P = 9.5\,\text{W}$, and (b) corresponding temperature profile on the deposition face of a YAG substrate.

Compared to the incoherent recombined Gaussian case, the beam waist and quadrant separation have increased to compensate for the shift of the effective edge that results because of Fresnel diffraction. Despite the additional modulation, however, a temperature distribution with comparable homogeneity to the incoherent case is still achieved. It is clear therefore that the tetra-prism design and experimental parameters can be optimised simply by using incoherent modeling in the case that has been studied here, but it would be useful to know how much the heating beam intensity can be modulated due to diffraction or interference before the temperature distribution is significantly affected. A simple two-dimensional (2D) model has been used in the next section to investigate this and give an indication of the role of substrate thickness as a thermal diffuser in the achievement of homogeneous temperature distributions.

Effect of substrate thickness on the temperature homogeneity

In order to generate simple rules for describing the influence of source intensity modulation on the homogeneity of substrate temperature, we can simplify by using a 2D thermal model. A cosine-squared modulation can serve as an approximation of the actual source intensity modulation for this simple modeling. In this case, the heat source function is given by

$$Q = \frac{Ak_f}{k_f h + \cos(k_f h)\sin(k_f h)} \cos^2(k_f y)\delta(z), \tag{A.11}$$

where A is a parameter similar to the beam power and can be varied to adjust the temperature, y is the direction parallel to the heating face, z is the direction perpendicular to the heating face, and $k_f = \pi/\Lambda$, where Λ is the heat intensity modulation periodicity that results from using the cosine squared function.

Simulations were carried out over a range of substrate thicknesses and heat intensity modulation periodicities. For simplicity, the heat intensity periodicities were chosen such that the modulation was symmetric about the substrate center. The parameter A was varied to give a temperature of 1073 ± 0.5K at the center of the substrate deposition face. To isolate the effect of changing the heat intensity modulation on the temperature inhomogeneity that results from the substrate edges, the parameter Δ was introduced,

$$\Delta = [T_{\text{mod}}(y) - T_{\text{flat}}(y)]_{\text{max values}} - [T_{\text{mod}}(y) - T_{\text{flat}}(y)]_{\text{min values}} \tag{A.12}$$

where T_{mod} is the temperature for the modulated heat intensity case and T_{flat} is the temperature for the unmodulated heat intensity case.

Figure A.5 shows Δ plotted for a range of heat intensity modulation periodicities from 0.2 mm up to 5.0 mm and for substrate thicknesses of 0.1, 0.25, 0.5, and 1.0 mm. The temperature inhomogeneity due to source modulation increases rapidly with increasing heat intensity modulation periodicity and decreasing substrate thicknesses. Thicker substrates allow more homogeneous temperature distributions to be produced because more thermal diffusion can take place between the heated face and the opposite deposition face.

Figure A.5 can be used as a guideline for how inhomogeneous a heat source can be

before it has a significant impact on the temperature homogeneity of substrates with different thicknesses.

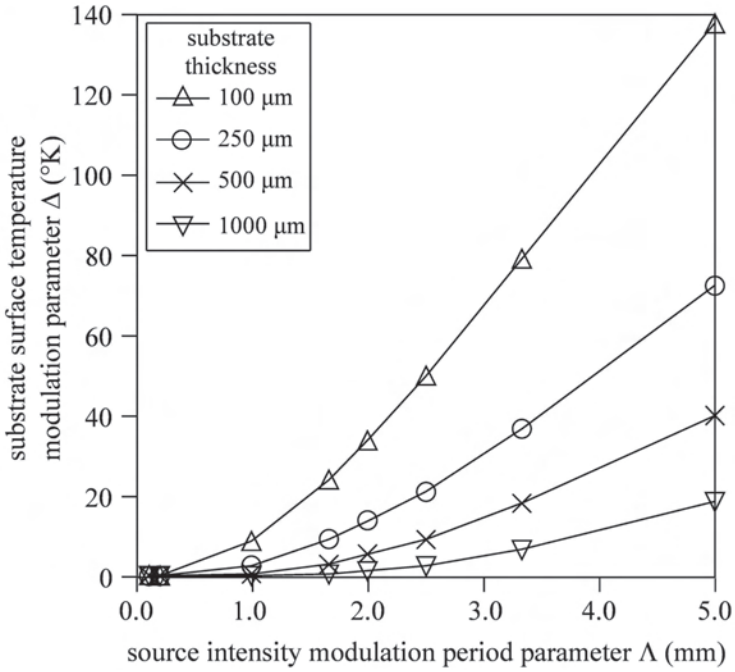

FIGURE A.5: Variation of the temperature inhomogeneity due to source modulation for substrate thicknesses of 0.1, 0.25, 0.5, and 1.0 mm.

Appendix B

List of publications

Listed below are the publications arising from the work in this thesis.

Journal articles

M. S. B. Darby, T. C. May-Smith, R. W. Eason Deposition and stoichiometry control of Nd-doped gadolinium gallium garnet thin films by combinatorial pulsed laser deposition using two targets of Nd:$Gd_3Ga_5O_{12}$ and Ga_2O_3, Applied Physics A: Materials Science & Processing 93 (2), 477 (2008)

M. S. B. Darby, R. E. Simpson, T. C. May-Smith, D. W. Hewak, R. W. Eason, Influence of deposition parameters on composition and refractive index of femtosecond and nanosecond pulsed laser deposited gallium lanthanum oxysulphide, Journal of Non-Crystalline Solids 354 (40-41), 4582 (2008)

M. S. B. Darby, T. C. May-Smith, R. W. Eason, T. Donnelly, J. G. Lunney, K. D. Rogers, A comparative study of gadolinium gallium garnet growth by femtosecond and nanosecond pulsed laser deposition, Applied Surface Science, 254:1361-1369 (2008)

T. C. May-Smith, A. C. Muir, **M. S. B. Darby**, and R. W. Eason, Design and performance of a ZnSe tetra-prism for homogeneous substrate heating using a CO_2 laser for pulsed laser deposition experiments, Applied Optics, 47:1768-1780 (2008).

Conference presentations

M. S. B. Darby, T. C. May-Smith, R. W. Eason, T. Donnelly, J. G. Lunney, K. D. Rogers, Garnet crystal growth by femtosecond pulsed laser deposition (oral presentation), Conference on Laser Ablation, Tenerife, 22-28 September 2007.

M. S. B. Darby, R. E. Simpson, D. W. Hewak, R. W. Eason, Femtosecond pulsed laser deposition of amorphous gallium lanthanum oxysulphide films (poster presentation), Conference on Laser Ablation, Tenerife, 22-28 September 2007.

Other presentations by group members

R. W. Eason, T. C. May-Smith, C. Grivas, D. P. Shepherd, **M. S. B. Darby**, R. Gazia, Pulsed laser deposition (PLD) growth of high quality low-loss optical waveguide films of ternary and quarternary doped garnets. Paul Scherrer Institute Vilingen Switzerland July 2008 (Invited).

R. W. Eason, T. C. May-Smith, C. Grivas, **M. S. B. Darby**, D. P. Shepherd, R. Gazia, Current state of the art of pulsed laser deposition: existing capabilities and future trends, E-MRS 2008 Spring Meeting Strasbourg 26-30 May 2008 (Invited).

R. W. Eason, T. May-Smith, C. Grivas, D. P. Shepherd, **M. S. B. Darby**, R. Gazia, Pulsed laser deposition for growth of high quality epitaxial garnet films for low threshold waveguide lasers, Seminar: National Technical University of Athens Athens 20 June 2007 (Invited).

R. W. Eason, T. C. May-Smith, C. Grivas, D. P. Shepherd, **M. S. B. Darby**, R. Gazia, Pulsed laser deposition for growth of high quality epitaxial garnet films for low threshold waveguide lasers, Invited Talk at Tyndall National Institute Cork, Ireland 3 Apr 2007 (Invited)

C. Grivas, T. C. May-Smith, J. Wang, **M. S. B. Darby**, D. P. Shepherd, R. W. Eason, A low-loss PLD fabricated garnet planar waveguide laser, EPS-QEOD Europhoton Conference Lausanne 29 August – 3 September 2004.

C. Grivas, D. P. Shepherd, T. C. May-Smith, **M. S. B. Darby**, R. W. Eason, M. Pollnau, Ar^+ beam etched Ti:sapphire rib waveguides: a route for the development of broadband fluorescence and channel laser sources, CLEO/IQEC 2004 San Francisco 16-21 May 2004.

T. C. May-Smith, C. Grivas, D. P. Shepherd, **M. S. B. Darby**, R. W. Eason, Pulsed laser deposition of thick multilayer garnet films for cladding-pumped planar waveguide laser devices, CLEO/IQEC 2004 San Francisco, 16-21 May 2004.

References

Acquaviva, S., Perrone, A., Zocco, A., Klini, A. & Fotakis, C. (2000), 'Deposition of carbon nitride films by reactive sub-picosecond pulsed laser ablation', *Thin Solid Films* **373**, 266–272.

Afonso, C. N., Gonzalo, J., Vega, F., Dieguez, E., Wong, J. C. C., Ortega, C., Siejka, J. & Amsel, G. (1995), 'Correlation between optical-properties, composition, and deposition parameters in pulsed-laser deposited $LiNbO_3$ films', *Applied Physics Letters* **66**, 1452–1454.

Afonso, C. N., Vega, F., Gonzalo, J. & Zaldo, C. (1993), 'Lithium-niobate films grown by excimer-laser deposition', *Applied Surface Science* **69**, 149–155.

Ahrens, L. H. (1952), 'The use of ionization potentials part 1. ionic radii of the elements', *Geochimica et Cosmochimica Acta* **2**, 155–169.

Albert, O., Roger, S., Glinec, Y., Loulergue, J. C., Etchepare, J., Boulmer-Leborgne, C., Perriere, J. & Millon, E. (2003), 'Time-resolved spectroscopy measurements of a titanium plasma induced by nanosecond and femtosecond lasers', *Applied Physics A: Materials Science & Processing* **76**, 319–323.

Allibert, M., Chatillo.C, Marescha.J & Lissalde, F. (1974), 'Study of phase-diagram in system Gd_2O_3 – Ga_2O_3', *Journal of Crystal Growth* **23**, 289–294.

Amoruso, S., Altucci, C., Bruzzese, R., de Lisio, C., Spinelli, N., Velotta, R., Vitiello, M. & Wang, X. (2004a), 'Study of the plasma plume generated during near IR femtosecond laser irradiation of silicon targets', *Applied Physics A: Materials Science & Processing* **79**, 1377–1380.

Amoruso, S., Bruzzese, R., Spinelli, N., Velotta, R., Vitiello, M., Wang, X., Ausanio, G., Iannotti, V. & Lanotte, L. (2004b), 'Generation of silicon nanoparticles via femtosecond laser ablation in vacuum', *Applied Physics Letters* **84**, 4502–4504.

Anderson, A. A., Eason, R. W., Jelinek, M., Grivas, C., Lane, D., Rogers, K., Hickey, J. M. B. & Fotakis, C. (1997), 'Growth of Ti:sapphire single crystal thin films by pulsed laser deposition', *Thin Solid Films* **300**, 68–71.

Anisimov, S. I., Kapeliovich, L. B. & Perelman, T. (1974), *Soviet Physics JETP* **39**, 375.

Ashkenasi, D., Lorenz, M., Stoian, R. & Rosenfeld, A. (1999), 'Surface damage threshold and structuring of dielectrics using femtosecond laser pulses: the role of incubation', *Applied Surface Science* **150**, 101–106.

Barrington, S. J. & Eason, R. W. (2000), 'Homogeneous substrate heating using a CO_2 laser with feedback, rastering, and temperature monitoring', *Review Of Scientific Instruments* **71**, 4223–4225.

Blank, D. H. A., Koster, G., Rijnders, G. A. J. H. M., van Setten, E., Slycke, P. & Rogalla, H. (2000), 'Epitaxial growth of oxides with pulsed laser interval deposition', *Journal of Crystal Growth* **211**, 98–105.

Bouquet, V., Longo, E., Leite, E. R. & Varela, J. A. (1999), 'Influence of heat treatment on $LiNbO_3$ thin films prepared on Si (111) by the polymeric precursor method', *Journal of Materials Research* **14**, 3115–3121.

Brandle, C. D. & Barns, R. L. (1974), 'Crystal stoichiometry of Czochralski grown rare-earth gallium garnets', *Journal of Crystal Growth* **26**, 169–170.

Brodoceanu, D., Manousaki, A., Zergioti, I., Klini, A., Dinescu, M. & Fotakis, C. (2004), 'Growth of polycrystalline $La_{0.5}Sr_{0.5}CoO_3$ films by femtosecond pulsed laser deposition', *Applied Physics A: Materials Science & Processing* **79**, 911–914.

Brorson, S. D., Fujimoto, J. G. & Ippen, E. P. (1987), 'Femtosecond electronic heat-transport dynamics in thin gold-films', *Physical Review Letters* **59**, 1962–1965.

Catlow, C. R. A. & Mackrodt, W. C., eds (1982), *Computer Simultation of Solids*, Springer-Verlag Berlin Heidelberg New York.

Cha, Y. H., Lee, Y. W., Nam, S. M., Han, J. M., Rhee, Y. J., Yoo, B. D., Lee, B. C. & Jeong, Y. U. (2007), 'Simple method for the temporal characterization of amplified spontaneous emission in femtosecond terawatt Ti:sapphire lasers', *Applied Optics* **46**, 6854–6858.

Chaos, J. A., Dreyfus, R. W., Perea, A., Serna, R., Gonzalo, J. & Afonso, C. N. (2000), 'Delayed release of Li atoms from laser ablated lithium niobate', *Applied Physics Letters* **76**, 649–651.

Chaos, J. A., Gonzalo, J., Afonso, C. N., Perriere, J. & Garcia-Gonzalez, M. T. (2001), 'Growth of stoichiometric and textured $LiNbO_3$ films on Si by pulsed laser deposition', *Applied Physics A: Materials Science & Processing* **72**, 705–710.

Chen, L. (1994), *Pulsed laser deposition of thin films*, John Wiley & Sons, Inc, chapter 6, pp. 167–198.

Chern, G. C. & Lauks, I. (1982), 'Spin-coated amorphous-chalcogenide films', *Journal of Applied Physics* **53**, 6979–6982.

Chichkov, B. N., Momma, C., Nolte, S., von Alvensleben, F. & Tünnermann, A. (1996), 'Femtosecond, picosecond and nanosecond laser ablation of solids', *Applied Physics A: Material Sciences & Processes* **63**, 109–115.

Choopun, S., Vispute, R. D., Noch, W., Balsamo, A., Sharma, R. P., Venkatesan, T., Iliadis, A. & Look, D. C. (1999), 'Oxygen pressure-tuned epitaxy and optoelectronic properties of laser-deposited ZnO films on sapphire', *Applied Physics Letters* **75**, 3947–3949.

Daguzan, P., Guizard, S., Krastev, K., Martin, P., Petite, G., Dossantos, A. & Antonetti, A. (1994), 'Direct observation of multiple-photon absorption by free-electrons in a wide band-gap insulator under strong laser irradiation', *Physical Review Letters* **73**, 2352–2355.

Dijkamp, D., Venkatesan, T., Wu, X. D., Shaheen, S. A., Jisrawi, N., Min-Lee, Y. H., McLean, W. L. & Croft, M. (1987), 'Preparation of Y-Ba-Cu oxide superconductor thin-films using pulsed laser evaporation from high-T_c bulk material', *Appled Physics Letters* **51**, 619–621.

Dominguez, J. E., Pan, X. Q., Fu, L., Van Rompay, P. A., Zhang, Z., Nees, J. A. & Pronko, P. P. (2002), 'Epitaxial SnO_2 thin films grown on $(\bar{1}012)$ sapphire by femtosecond pulsed laser deposition', *Journal Of Applied Physics* **91**, 1060–1065.

Dong, J. & Lu, K. (1991), 'Noncubic symmetry in garnet structures studied using extended x-ray absorption fine-structure spectra', *Physical Review B* **43**, 8808–8821.

Dong, Y. Y. & Molian, P. (2004), 'Coulomb explosion-induced formation of highly oriented nanoparticles on thin films of 3C-SiC by the femtosecond pulsed laser', *Applied Physics Letters* **84**, 10–12.

Du, D., Liu, X., Korn, G., Squier, J. & Mourou, G. (1994), 'Laser-induced breakdown by impact ionization in SiO_2 with pulse widths from 7 ns to 150 fs', *Applied Physics Letters* **64**, 3071–3073.

Flahaut, J., Guittard, M. & Loireaulozach, A. M. (1983), 'Rare-earth sulfide and oxysulfide glasses', *Glass Technology* **24**, 149–156.

Frantz, J. A., Shaw, L. B., Sanghera, J. S. & Aggarwal, I. D. (2006), 'Waveguide amplifiers in sputtered films of Er^{3+}-doped gallium lanthanum sulfide glass', *Optics Express* **14**, 1797–1803.

Fujimoto, J. G., Liu, J. M., Ippen, E. P. & Bloembergen, N. (1984), 'Femtosecond laser interaction with metallic tungsten and nonequilibrium electron and lattice temperatures', *Physical Review Letters* **53**, 1837–1840.

Galasso, F. S. (1970), *Stucture and properties of inorganic solids*, Pergamon press.

Gamaly, E. G., Rode, A. V., Uteza, O., Kolev, V., Luther-Davies, B., Bauer, T., Koch, J., Korte, F. & Chichkov, B. N. (2004), 'Control over a phase state of the laser plume ablated by femtosecond laser: spatial pulse shaping', *Journal of Applied Physics* **95**, 2250–2257.

Gaponov, S. V., Gudkov, A. A. & Fraerman, A. A. (1982), 'Processes occurring in an erosion plasma during laser vacuum deposition of films. iii. condensation in gas flows during laser vaporization of materials.', *Soviet Physics. Technical Physics* **27**, 1130–1133.

Garrelie, F., Loir, A. S., Donnet, L. C., Rogemond, F., Le Harzic, R., Belin, M., Audouard, E. & Laporte, P. (2003), 'Femtosecond pulsed laser deposition of diamond-like carbon thin films for tribological applications', *Surface & Coatings Technology* **163**, 306–312.

Geller, S. (1967), 'Crystal chemistry of garnets', *Zeitschrift Für Kristallographie, Kristallgeometrie, Kristallphysik, Kristallchemie* **125**, 1–47.

Ghica, D., Ghica, C., Gartner, M., Nelea, V., Martin, C., Cavaleru, A. & Mihailescu, I. N. (1999), 'Pulsed laser deposition of lithium niobate: a parametric study', *Applied Surface Science* **139**, 617–621.

Gill, D. S., Eason, R. W., Zaldo, C., Rutt, H. N. & Vainos, N. A. (1995), 'Characterization of Ga-La-S chalcogenide glass thin-film optical wave-guides, fabricated by pulsed-laser deposition', *Journal of Non-Crystalline Solids* **191**, 321–326.

Glass, H. L. & Elliott, M. T. (1974), 'Accommodation of Pb in yttrium iron-garnet films grown by liquid-phase epitaxy', *Journal of Crystal Growth* **27**, 253–260.

Glover, T. E., Ackerman, G. D., Belkacem, A., Heimann, P. A., Hussain, Z., Lee, R. W., Padmore, H. A., Ray, C., Schoenlein, R. W., Steele, W. F. & Young, D. A. (2003), 'Metal-insulator transitions in an expanding metallic fluid: Particle formation kinetics', *Physical Review Letters* **90**, 236102.

Gorbunoff, A. (2007), *Cross-beam PLD: metastable film structures from intersection plumes*, John Wiley & Sons, Inc., Hoboken, New Jersey, chapter 6, pp. 131–160.

Gorbunov, A. A., Pompe, W., Sewing, A., Gaponov, S. V., Akhsakhalyan, A. D., Zabrodin, I. G., Kaskov, I. A., Klyenkov, E. B., Morozov, A. P., Salaschenko, N. N., Dietsch, R., Mai, H. & Vollmar, S. (1996), 'Ultrathin film deposition by pulsed laser ablation using crossed beams', *Applied Surface Science* **96–98**, 649–655.

Gorbunov, A. A., Tselev, A. E., Elefant, D., Geisler, H., Henninger, G., Mensch, A., Meyer, D. C., Wolf, B., Paufler, P., Pompe, W., Schneider, C. M. & Worch, H. (1999), 'Thin film mixtures synthesized by cross-beam PLD', *Applied Physics A-Materials Science & Processing* **69**, S463–S466.

Gorbunov, A., Levin, A. A., Mensch, A., Meyer, D. C., Tselev, A., Paufler, P., Pompe, W. & Eckert, D. (2002), 'Formation of unusual intermetallic phases by vacuum PLD', *Applied Surface Science* **197**, 475–480.

Greenwood, N. N. (1968), *Ionic Crystals, lattice defects and non-stoichiometry*, Butterworths.

Guarino, A., Poberaj, G., Rezzonico, D., Degl'Innocenti, R. & Gunter, P. (2007), 'Electro-optically tunable microring resonators in lithium niobate', *Nature Photonics* **1**, 407–410.

Guo, X. L., Hu, W. S., Liu, Z. G., Zhu, S. N., Yu, T., Xiong, S. B. & Lin, C. Y. (1998), 'In-situ poling of lithium niobate films on silicon wafer by applying a low electric field during pulsed laser deposition', *Materials Science and Engineering B: Solid State Materials for Advanced Technology* **53**, 278–283.

Hafez, M. A. & Elsayed-Ali, H. E. (2007), 'Formation of In-(2×1) and In islands on Si(100)-(2×1) by femtosecond pulsed laser deposition', *Journal of Applied Physics* **101**, 113515.

Harwood, D. W., Taylor, E. R., Moore, R. & Payne, D. (2003), 'Fabrication of fluoride glass planar waveguides by hot dip spin coating', *Journal of Non-Crystalline Solids* **332**, 190–198.

Hecht, E. (2002), *Optics*, Addison Wesley Longman, Inc.

Hirai, T., Fuse, K., Shiozaki, M., Ebata, K., Okada, T. & Namba, H. (2003), 'Characteristic of ZnSe aspheric beam homogenizer for CO_2 laser', *First International Symposium on High-Power Laser Macroprocessing* **4831**, 142–147.

Hohlfeld, J., Grosenick, D., Conrad, U. & Matthias, E. (1995), 'Femtosecond time-resolved reflection 2nd-harmonic generation on polycrystalline copper', *Applied Physics A: Materials Science & Processing* **60**, 137–142.

Hopkins, J. A., Schwartz, F. A., McCay, M. H., McCay, D. T., Dahotre, N. B. & Bible, J. B. (2000), 'Apparatus and method for producing an improved laser beam', *U.S. patent 6,016,227* .

Hopp, B., Smausz, T., Kecskemeti, G., Klini, A. & Bor, Z. (2007), 'Femtosecond pulsed laser deposition of biological and biocompatible thin layers', *Applied Surface Science* **253**, 7806–7809.

Huang, C. C. & Hewak, D. W. (2004), 'High-purity germanium-sulphide glass for opto-electronic applications synthesised by chemical vapour deposition', *Electronics Letters* **40**, 863–865.

Hur, N. H., Park, Y. K., Won, D. H. & No, K. S. (1994), 'Effect of substrates on the growth and properties of $LiNbO_3$ films by the sol-gel method', *Journal of Materials Research* **9**, 980–985.

Irissou, E., Vidal, F., Johnston, T., Chaker, M., Guay, D. & Ryabinin, A. N. (2006), 'Influence of an inert background gas on bimetallic cross-beam pulsed laser deposition', *Journal of Applied Physics* **99**, 034904.

Ivanov, V. V., Maksimchuk, A. & Mourou, G. (2003), 'Amplified spontaneous emission in a Ti:sapphire regenerative amplifier', *Applied Optics* **42**, 7231–7234.

Jelinek, M., Klini, A., Grivas, C., Lancok, J., Studnicka, V., Chval, J., Mackova, A. & Fotakis, C. (2002), 'Deposition of Er:YAG (YAP) layers by subpicosecond and nanosecond KrF excimer laser ablation', *Applied Surface Science* **197**, 416–420.

Joshkin, V. A., Moran, P., Saulys, D., Kuech, T. F., McCaughan, L. & Oktyabrsky, S. R. (2000), 'Growth of oriented lithium niobate on silicon by alternating gas flow chemical beam epitaxy with metalorganic precursors', *Applied Physics Letters* **76**, 2125–2127.

Kools, J. C. S., Baller, T. S., Dezwart, S. T. & Dieleman, J. (1992), 'Gas-flow dynamics in laser ablation deposition', *Journal of Applied Physics* **71**, 4547–4556.

Lambert, L., Grangeon, F. & Autric, M. (1999), 'Crossed beam pulsed laser deposition of cryolite thin films', *Applied Surface Science* **139**, 574–580.

Levin, A. A., Meyer, D. C., Gorbunov, A., Tselev, A., Gawlitza, P., Mai, H., Pompe, W. & Paufler, P. (2001), 'Comparative study of interfaces of Fe-Al multilayers prepared by direct and crossed-beam pulsed laser deposition', *Thin Solid Films* **391**, 47–56.

Li, R., Furniss, D., Bagshaw, H. & Seddon, A. B. (1999), 'Decisive role of oxide content in the formation and crystallization of gallium-lanthanum-sulfide glasses', *Journal of Materials Research* **14**, 2621–2627.

Liu, B., Hu, Z. D., Che, Y., Chen, Y. B. & Pan, X. Q. (2007), 'Nanoparticle generation in ultrafast pulsed laser ablation of nickel', *Applied Physics Letters* **90**, 044103.

Loir, A. S., Garrelie, F., Donnet, C., Belin, M., Forest, B., Rogemond, F. & Laporte, P. (2004), 'Deposition of tetrahedral diamond-like carbon thin films by femtosecond laser ablation for applications of hip joints', *Thin Solid Films* **453-54**, 531–536.

Loireau-Lozac'h, A. M., Guittard, M. & Flahaut, J. (1976), 'Glass formed by rare-earth sulfides (La_2S_3) with gallium sulfide (Ga_2S_3)', *Materials Research Bulletin* **11**, 1489–1496.

Lowndes, D. H., Rouleau, C. M., Thundat, T. G., Duscher, G., Kenik, E. A. & Pennycook, S. J. (1999), 'Silicon and zinc telluride nanoparticles synthesized by low energy density pulsed laser ablation into ambient gases', *Journal of Materials Research* **14**, 359–370.

Maglia, F., Buscaglia, V., Gennari, S., Ghigna, P., Dapiaggi, M., Speghini, A. & Bettinelli, M. (2006), 'Incorporation of trivalent cations in synthetic garnets $A_3B_5O_{12}$ (A=Y, Lu-La, B=Al, Fe, Ga)', *Journal of Physical Chemistry B* **110**, 6561–6568.

Mairaj, A. K., Curry, R. J. & Hewak, D. W. (2004), 'Chalcogenide glass thin films through inverted deposition and high velocity spinning', *Electronics Letters* **40**, 421–422.

Mairaj, A. K., Curry, R. J. & Hewak, D. W. (2005), 'Inverted deposition and high-velocity spinning to develop buried planar chalcogenide glass waveguides for highly nonlinear integrated optics', *Applied Physics Letters* **86**, 094102.

Makino, H., Nakamura, S. & Matsumi, K. (1976), 'Lattice-parameter variations in Czochralski grown gadolinium gallium garnet single-crystals', *Japanese Journal of Applied Physics* **15**, 415–419.

Marple, D. T. F. (1964), 'Refractive index of ZnSe, ZnTe and CdTe', *Journal of Applied Physics* **35**, 539–542.

May-Smith, T. C. & Eason, R. W. (2007), 'Comparative growth study of garnet crystal films fabricated by pulsed laser deposition', *Journal of Crystal Growth* **308**, 382–391.

May-Smith, T. C., Muir, A. C., Darby, M. S. B. & Eason, R. W. (2008), 'Design and performance of a ZnSe tetra-prism for homogeneous substrate heating using a CO_2 laser for pulsed laser deposition experiments', *Applied Optics* **47**, 1767–1780.

Milanese, C., Buscaglia, V., Maglia, F. & Anselmi-Tamburini, U. (2004), 'Disorder and nonstoichiometry in synthetic garnets $A_3B_5O_{12}$ (A = Y, Lu-La, B=Al, Fe, Ga). A simulation study', *Chemistry of Materials* **16**, 1232–1239.

Millon, E., Albert, O., Loulergue, J. C., Etchepare, J., Hulin, D., Seiler, W. & Perriere, J. (2000), 'Growth of heteroepitaxial ZnO thin films by femtosecond pulsed-laser deposition', *Journal of Applied Physics* **88**, 6937–6939.

Millon, E., Perriere, J., Defourneau, R. M., Defourneau, D., Albert, O. & Etchepare, J. (2003), 'Femtosecond pulsed-laser deposition of $BaTiO_3$', *Applied Physics A: Materials Science & Processing* **77**, 73–80.

Nakanishi, Y., Mizota, H., Ito, Y., Takano, M., Fukao, S., Yoshikado, S., Ohyama, K., Yamada, K. & Fukushima, S. (2006), 'Relation between x-ray emission mechanism and crystal structure in $LiNbO_3$', *Physica Scripta* **73**, 471–477.

Nakatsuka, A., Yoshiasa, A. & Takeno, S. (1995), 'Site preference of cations and structural variation in $Y3Fe_{5-x}Ga_xO_{12}$ ($0 \leq x \leq 5$) solid-solutions with garnet structure', *Acta Crystallographica Section B* **51**, 737–745.

Noël, S., Hermann, J. & Itina, T. (2007), 'Investigation of nanoparticle generation during femtosecond laser ablation of metals', *Applied Surface Science* **253**, 6310–6315.

Ogale, S. B., Nawatheydikshit, R., Dikshit, S. J. & Kanetkar, S. M. (1992), 'Pulsed laser deposition of stoichiometric $LiNbO_3$ thin-films by using O_2 and Ar gas-mixtures as ambients', *Journal of Applied Physics* **71**, 5718–5720.

Ovshinsky, S. R. (1968), 'Reversible electrical switching phenomena in disordered structures', *Physical Review Letters* **21**(20), 1450.

Padture, N. P. & Klemens, P. G. (1997), 'Low thermal conductivity in garnets', *Journal of the American Ceramic Society* **80**, 1018–1020.

Pauling, L. (1932), 'The nature of the chemical bond. iv. the energy of single bonds and the relative electronegativity of atoms', *Journal of the American Chemical Society* **54**, 3570–3585.

Pechen, E. V., Krasnosvobodtsev, S. I., Kessler, G., Richter, A., Panzner, M., Grossmann, O. & Teresiak, A. (1992), '2-beam laser deposition process for $Y_1Ba_2Cu_3O_{7-x}$ films on silicon', *Physica Status Solidi A – Applied Research* **131**, 179–189.

Perez, D. & Lewis, L. J. (2002), 'Ablation of solids under femtosecond laser pulses', *Physical Review Letters* **89**, 255504.

Perrière, J., Boulmer-Leborgne, C., Benzerga, R. & Tricot, S. (2007), 'Nanoparticle formation by femtosecond laser ablation', *Journal of Physics D: Applied Physics* **40**, 7069–7076.

Pronko, P. P., VanRompay, P. A., Horvath, C., Loesel, F., Juhasz, T., Liu, X. & Mourou, G. (1998), 'Avalanche ionization and dielectric breakdown in silicon with ultrafast laser pulses', *Physical Review B* **58**, 2387–2390.

Rijnders, G., Koster, G., Leca, V., Blank, D. H. A. & Rogalla, H. (2000), 'Imposed layer-by-layer growth with pulsed laser interval deposition', *Applied Surface Science* **168**, 223–226.

Rizvi, N. H. (2002), 'Femtosecond laser micromachining: current status and applications', *Riken Review* **50**, 107–112.

Rode, A. V., Luther-Davies, B. & Gamaly, E. G. (1999), 'Ultrafast ablation with high-pulse-rate lasers. Part II: Experiments on laser deposition of amorphous carbon films', *Journal of Applied Physics* **85**, 4222–4230.

Rode, A. V., Zakery, A., Samoc, M., Charters, R. B., Gamaly, E. G. & Luther-Davies, B. (2002), 'Laser-deposited As_2S_3 chalcogenide films for waveguide applications', *Applied Surface Science* **197**, 481–485.

Sánchez Aké, C. S., Sobral, H., Ramos-Alvarez, P., Lemen, C. & Villagrán-Muniz, M. (2007), 'Ion kinetic energy control in cross-beam pulsed laser ablation on graphite targets', *Cola 2005: 8 th International Conference On Laser Ablation* **59**, 728–731.

Sawada, H. (1997), 'Electron density study of garnets: $Z_3Ga_5O_{12}$; Z = Nd, Sm, Gd, Tb', *Journal Of Solid State Chemistry* **132**(2), 300–307.

Schoenlein, R. W., Lin, W. Z. & Fujimoto, J. G. (1987), 'Femtosecond studies of nonequilibrium electron processess in metals', *Physical Review Letters* **18**, 1680–1683.

Shannon, R. D. (1976), 'Revised effective ionic radii and systematic studies of interatomic distances in halides and chalcogenides', *Acta Crystallographica A* **32**, 751–767.

Shannon, R. D. & Prewitt, C. T. (1969), 'Effective ionic radii in oxides and fluorides', *Acta Crystallographica B* **B25**, 925–946.

Simpson, R. E., Mairaj, A., Curry, R. J., Huang, C. C., Knight, K., Hassan, M. & Hewak, D. (2007), 'Electrical phase change of Ga:La:S:Cu films', *Electronics Letters* **43**, 830–832.

Slack, G. A., Oliver, D. W., Chrenko, R. M. & Roberts, S. (1969), 'Optical absorption of $Y_3Al_5O_{12}$ from 10 to 55 000 cm^{-1} wave numbers', *Physical Review* **177**, 1308–1314.

Stoian, R., Ashkenasi, D., Rosenfeld, A. & Campbell, E. E. B. (2000), 'Coulomb explosion in ultrashort pulsed laser ablation of Al_2O_3', *Physical Review B* **62**, 13167–13173.

Stoian, R., Rosenfeld, A., Ashkenasi, D., Hertel, I. V., Bulgakova, N. M. & Campbell, E. E. B. (2002), 'Surface charging and impulsive ion ejection during ultrashort pulsed laser ablation', *Physical Review Letters* **88**, 097603.

Strikovsky, M. D., Klyuenkov, E. B., Gaponov, S. V., Schubert, J. & Copetti, C. A. (1993), 'Crossed fluxes technique for pulsed-laser deposition of smooth $YBa_2Cu_3O_{7-x}$ films and multilayers', *Applied Physics Letters* **63**, 1146–1148.

Strocka, B., Holst, P. & Tolksdorf, W. (1978), 'An empirical formula for the calculation of lattice constants of oxide garnets based on substituted yttrium- and gadolinium-ion garnets', *Philips Journal of Research* **33**, 186–202.

Suchow, L. & Kokta, M. (1972), 'Magnetic properties of neodymium- small rare-earth gallium garnets with rare-earth ions on two crystallographic sites', *Journal of Solid State Chemistry* **5**, 85–92.

Talanov, V. M., Vorobov, J. P. & Men, A. N. (1975), 'Interpretation of concentration dependent properties of garnets and spinels by cluster components method', *Journal of Physics and Chemistry of Solids* **36**, 641–653.

Tam, A. C., Brand, J. L., Cheng, D. C. & Zapka, W. (1989), 'Picosecond laser sputtering of sapphire at 266 nm', *Applied Physics Letters* **55**, 2045–2047.

Teghil, R., D'Alessio, L., De Bonis, A., Galasso, A., Villani, P. & Santagata, A. (2006), 'Femtosecond pulsed laser ablation and deposition of titanium carbide', *Thin Solid Films* **515**, 1411–1418.

Teghil, R., D'Alessio, L., Santagata, A., Zaccagnino, M., Ferro, D. & Sordelet, D. J. (2003), 'Picosecond and femtosecond pulsed laser ablation and deposition of quasicrystals', *Applied Surface Science* **210**, 307–317.

Teghil, R., Ferro, D., Galasso, A., Giardini, A., Marotta, V., Parisi, G. P., Santagata, A. & Villani, P. (2007), 'Femtosecond pulsed laser deposition of nanostructured ITO thin

films', *Materials Science & Engineering C – Biomimetic and Supramolecular Systems* **27**, 1034–1037.

Tong, X. L., Jiang, D. S., Li, Y., Liu, Z. M. & Luo, M. Z. (2006), 'Femtosecond pulsed laser deposition of CdS thin films onto quartz substrates', *Physica Status Solidi A: Applications And Materials Science* **203**, 1992–1998.

Trelenberg, T. W., Dinh, L. N., Saw, C. K., Stuart, B. C. & Balooch, M. (2004), 'Femtosecond pulsed laser ablation of GaAs', *Applied Surface Science* **221**, 364–369.

Tselev, A., Gorbunov, A. & Pompe, W. (1999), 'Features of the film-growth conditions by cross-beampulsed-laser deposition', *Applied Physics A: Materials Science & Processing* **69**, 353–358.

Tselev, A., Gorbunov, A. & Pompe, W. (2001), 'Cross-beam pulsed laser deposition: General characteristic', *Review of Scientific Instruments* **72**, 2665–2672.

Tull, B. R., Carey, J. E., Sheehy, M. A., Friend, C. & Mazur, E. (2006), 'Formation of silicon nanoparticles and web-like aggregates by femtosecond laser ablation in a background gas', *Applied Physics A: Materials Science & Processing* **83**, 341–346.

Urbassek, H. M. & Sibold, D. (1993), 'Gas-phase segregation effects in pulsed laser desorption from binary targets', *Physical Review Letters* **70**, 1886–1889.

Vorobiov, Y. P. & Carban, O. V. (1997), 'A new empirical formula for the calculation of an elementary cell parameter of synthetic oxides-garnets', *Journal of Solid State Chemistry* **134**, 338–343.

Wang, K., Wamwangi, D., Ziegler, S., Steimer, C. & Wuttig, M. (2004), 'Influence of Bi doping upon the phase change characteristics of $Ge_2Sb_2Te_5$', *Journal of Applied Physics* **96**, 5557–5562.

Winkler, G., Hansen, P. & Holst, P. (1972), 'Variation of magnetic material parameters and lattice-constants of polycrystalline yttrium-iron garnet by incorporation of nonmagnetic ions', *Philips Research Reports* **27**, 151–156.

Womack, M., Vendan, M. & Molian, P. (2004), 'Femtosecond pulsed laser ablation and deposition of thin films of polytetrafluoroethylene', *Applied Surface Science* **221**, 99–109.

Wu, K. H., Lee, C. L., Juang, J. Y., Uen, T. M. & Gou, Y. S. (1991), 'Insitu growth of $Y_1Ba_2Cu_3O_{7-x}$ superconducting thin-films using a pulsed neodymium yttrium-aluminum-garnet laser with CO_2-laser heated substrates', *Applied Physics Letters* **58**, 1089–1091.

Xu, J. & Almeida, R. M. (2000a), 'Sol-gel derived germanium sulfide planar waveguides', *Materials Science in Semiconductor Processing* **3**, 339–344.

Xu, Y. N. & Ching, W. Y. (1999), 'Electronic structure of yttrium aluminum garnet $Y_3Al_5O_{12}$', *Physical Review B* **59**, 10530–10535.

Xu, Y. N., Ching, W. Y. & Brickeen, B. K. (2000b), 'Electronic structure and bonding in garnet crystals $Gd_3Sc_2Ga_3O_{12}$, $Gd_3Sc_2Al_3O_{12}$, and $Gd_3Ga_5O_{12}$ compared to $Y_3Al_3O_{12}$', *Physical Review B* **61**, 1817–1824.

Yoo, K. M., Zhao, X. M., Siddique, M., Alfano, R. R., Osterman, D. P., Radparvar, M. & Cunniff, J. (1990), 'Femtosecond thermal modulation measurements of electron-phonon relaxation in niobium', *Applied Physics Letters* **56**, 1908–1910.

Youden, K. E., Grevatt, T., Eason, R. W., Rutt, H. N., Deol, R. S. & Wylangowski, G. (1993), 'Pulsed-laser deposition of Ga-La-S chalcogenide glass thin-film optical wave-guides', *Applied Physics Letters* **63**, 1601–1603.

Zakery, A. & Elliott, S. R. (2003), 'Optical properties and applications of chalcogenide glasses: a review', *Journal of Non-Crystalline Solids* **330**, 1–12.

Zhang, Y. F., Russo, R. E. & Mao, S. S. (2005), 'Femtosecond laser assisted growth of ZnO nanowires', *Applied Physics Letters* **87**, 133115.

Zhang, Z., VanRompay, P. A., Nees, J. A., Clarke, R., Pan, X. & Pronko, P. P. (2000), 'Nitride film deposition by femtosecond and nanosecond laser ablation in low-pressure nitrogen discharge gas', *Applied Surface Science* **154**, 165–171.

Zhigilei, L. V. (2003), 'Dynamics of the plume formation and parameters of the ejected clusters in short-pulse laser ablation', *Applied Physics A: Materials Science & Processing* **76**, 339–350.